Theory and Simulations of Incomplete Reconnection During Sawteeth Due to Diamagnetic Effects

Matthew Thomas Beidler

Dissertation submitted
to the Eberly College of Arts and Sciences
at West Virginia University

in partial fulfillment of the requirements for the degree of

Doctor of Philosophy in
Physics

Paul A. Cassak, Ph. D., Chair
Zachariah B. Etienne, Ph. D.
Leonardo Golubovic, Ph. D.
Mark E. Koepke, Ph. D.
Earl E. Scime, Ph. D.

Department of Physics and Astronomy

Morgantown, West Virginia
2015

Keywords: fusion, magnetic reconnetion, sawteeth

ABSTRACT

Theory and Simulations of Incomplete Reconnection During Sawteeth Due to Diamagnetic Effects

Matthew Thomas Beidler

Tokamaks use magnetic fields to confine plasmas to achieve fusion; they are the leading approach proposed for the widespread production of fusion energy. The sawtooth crash in tokamaks limits the core temperature, adversely impacts confinement, and seeds disruptions. Adequate knowledge of the physics governing the sawtooth crash and a predictive capability of its ramifications has been elusive, including an understanding of incomplete reconnection, i.e., why sawteeth often cease prematurely before processing all available magnetic flux. In this dissertation, we introduce a model for incomplete reconnection in sawtooth crashes resulting from increasing diamagnetic effects in the nonlinear phase of magnetic reconnection. Physically, the reconnection inflow self-consistently convects the high pressure core of a tokamak toward the $q = 1$ rational surface, thereby increasing the pressure gradient at the reconnection site. If the pressure gradient at the rational surface becomes large enough due to the self-consistent evolution, incomplete reconnection will occur due to diamagnetic effects becoming large enough to suppress reconnection. Predictions of this model are borne out in large-scale proof-of-principle two-fluid simulations of reconnection in a 2D slab geometry and are also consistent with data from the Mega Ampere Spherical Tokamak (MAST). Additionally, we present simulations from the 3D extended-MHD code M3D-C^1 used to study the sawtooth crash in a 3D toroidal geometry for resistive-MHD and two-fluid models. This is the first study in a 3D tokamak geometry to show that the inclusion of two-fluid physics in the model equations is essential for recovering timescales more closely in line with experimental results compared to resistive-MHD and contrast the dynamics in the two models. We use a novel approach to sample the data in the plane of reconnection perpendicular to the $(m, n) = (1, 1)$ mode to carefully assess the reconnection physics. Using local measures of reconnection, we find that it is much faster in the two-fluid simulations, consistent with expectations based on global measures. By sampling data in the reconnection plane, we present the first observation of the quadrupole out-of-plane magnetic field appearing during sawtooth reconnection with the Hall term. We also explore how reconnection as viewed in the reconnection plane varies toroidally, which affects the symmetry of the reconnection geometry and the local diamagnetic effects. We expect our results to be useful for transport modeling in tokamaks, predicting energetic alpha-particle confinement, and assessing how sawteeth trigger disruptions. Since the model only depends on local diamagnetic and reconnection physics, it is machine independent, and should apply both to existing tokamaks and future ones such as ITER.

This work is dedicated to:

My Family To my Mom for always being there to motivate me to keep pushing, and to talk through complex things, no matter how one-sided the conversation could become. To my Dad for always being confident in my abilities and giving me the sense that I would succeed no matter the arena. To my sister for showing me what true work-ethic is, with her immense personal drive to accomplish her goals. And to my Nana, for setting the stage on which my sister and I have achieved our academic pursuits.

Acknowledgements

This manuscript could not have been finished without the tireless work of my advisor and colleague, Paul Cassak. He was always there to help me organize my thoughts and make the most of my ideas. I am truly grateful for the time we have had to work together, and look forward to collaborating with him throughout my career.

I am also thankful for the efforts of my Ph.D. committee, Zach Etienne, Leonardo Golubovic, Mark Koepke, and Earl Scime. Zach and I have had lively conversations on plasma physics and computational science. Leo was an extremely memorable professor, and his ability to express physics from first-principles allowed me to connect esoteric concepts. Mark has provided me a wealth of information while navigating the fusion community as I prepare to make a future impact. And Earl has always had an open door and welcomed all my questions regarding how to connect experiment, theory, and simulations.

The members of my research group have given me invaluable help through the years, whether through valuable discussions, lines of code, or breaks from work. Many thanks to Colin Komar, Luke Shepherd, Ray Fermo, Chris Doss, and Milton Arencibia.

I have had friendships with many people throughout Morgantown, in the physics department and the greater community. In the physics department I owe a great deal of thanks to Matt Galante, Dusty McCarren, Justin Elfritz, Rich Magee, John McKee, Drew Elliott, Umair Siddiqui, and Evan Delfino. From the Morgantown community I want to acknowledge Pete Martone, Debbie Louis, Beth Howell, Jason Collett, and Sasha Stolin.

I would like to thank everyone with whom I have collaborated to make the following work possible. This list includes Jim Drake, Mike Shay, Barrett Rogers, Marc Swisdak, Kittipat Malakit, Steve Jardin, Nate Ferraro, and Isabel Krebs.

Table of Contents

List of Figures

List of Tables

Chapter 1

Review of Sawteeth in Tokamaks

1.1 Fusion

1.1.1 Motivation

In the past century the human population has increased nonlinearly mainly due to medical advances and improvements in agricultural productivity, which have caused mortality rates to decrease and birth rates to increase. At the same time, our technological capabilities have increased exponentially consistent with "Moore's law". A continuously growing population consuming an exponentially increasing amount will eventually exhaust the limited resources our planet provides. In order to continue developing new technology and processing raw materials to support our growing population's needs, a vast amount of energy is required. The current use of fossil fuels to power our technology relies on rearranging the chemical bonds of hydrocarbon molecules utilizing the combustion reaction. However the energy contained in these chemical bonds pales in comparison to the energy contained in the nuclear bonds holding together the core of individual atoms, ~ 1 eV versus ~ 10 MeV (*Chen*, 2011)!

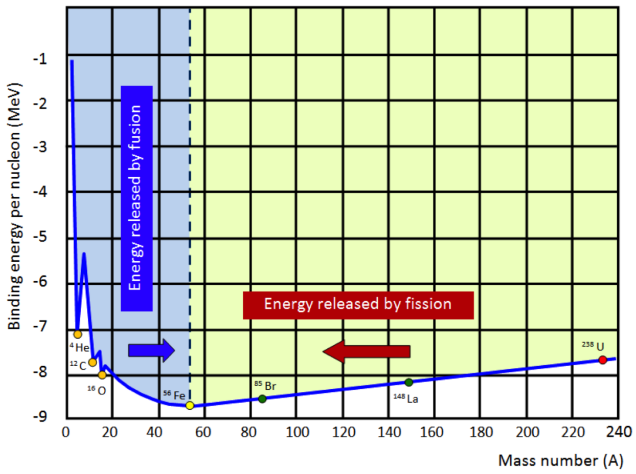

Figure 1.1: A curve showing the nuclear binding energy per nuclear particle as a function of mass of the element. Note the global minimum at iron ($A = 56$). Generally, processes that increase the atomic number of light elements or decrease the atomic number of heavy elements result in a decrease of nuclear energy. From *Gibbs* (2012).

To motivate how nuclear energy is stored and how it can be extracted, Fig. 1.1 shows the binding energy per individual nuclear particle (protons and neutrons) across different elements due to the strong nuclear force. This curve takes an interesting shape, having a minimum[1] binding energy for iron atoms with 56 nucleons. Nuclear reactions in which nuclei with large binding energy are transformed to nuclei with lower binding energy results in a decrease in the total binding energy, which must be transformed to another form of energy if the total energy is to be conserved. Nuclear binding energy can also be interpreted as the mass per nucleon, and the change in binding energy is consistent with a change in mass by Einstein's relation $\delta E = \delta m c^2$. This excess energy is almost entirely converted into kinetic energy of the resulting particles, and when considering all reactions over an ensemble of nuclei, it can be interpreted as an increase in the temperature of the resulting particles. Since the minimum nuclear binding energy per nucleon can be achieved by both

[1]The convention shown with nuclear binding energy as negative reflects that the more stable nuclei sit in a deeper potential well, and more energy must be added to break their bonds.

heavy elements undergoing reactions to produce lighter elements and also lighter elements undergoing reactions to produce heavier elements, there are two kinds of nuclear reactions: fission and fusion.

1.1.2 Nuclear Reactions

Mankind has already successfully harnessed the power released from fission reactions, with power plants spread across the globe. To induce a fission reaction, a heavy element, like uranium-235, is bombarded with energetic neutrons and, when a neutron strikes a uranium nucleus, the nucleus splits into two smaller nuclei and additional energetic neutrons. However, when heavy nuclei are split into lighter elements they often have extra neutrons as compared to more stable isotopes of the resultant element. This makes the products of fission reactions unstable to radioactive beta decay, where a neutron spontaneously decays into a proton and an energetic electron. The energetic electrons are expelled from the nuclei at high speeds and can do damage to nearby organisms, either directly killing their cells, or causing harmful mutations to their DNA. The half-life of these radioactive fission products can be on the order of human lifetimes, making the delicate storage of this waste the major drawback of fission power.

Fortunately, the fusion reaction does not produce the same amount of radioactive material; unfortunately though, it has proven much more difficult to properly induce and harvest energy from fusion reactions than was the case for fission reactions. While triggering a fission reaction is akin to shooting a target with a bullet, the fusion reaction can be thought of as shooting a volley of bullets towards one another and waiting for two to collide. An example of a fusion reaction can be seen in Fig. 1.2 where a collision of deuterium and tritium nuclei results in the production of a helium nucleus, a free neutron, and 17.6MeV of energy from

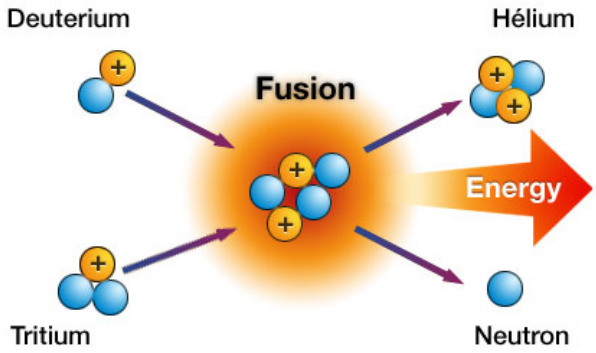

Figure 1.2: Illustration of a fusion reaction from *Barabaschi* (2015). A collision between deuterium and tritium nuclei results in a helium nucleus, a free neutron, and 17.6 MeV of energy from the restructuring of the nuclear bonds.

the restructuring of the nuclear bonds. From conservation of momentum, the helium nucleus and neutron respectively receive 1/5 and 4/5 of this energy as kinetic energy.

In order for nuclei, which are positively charged, to overcome their mutual electrical repulsion and fuse together, they must have a large kinetic energy. To produce nuclei with large kinetic energies there are two main approaches, strip neutral atoms of their electrons to create charged particles and accelerate them with electric fields, or heating up a gas to undergo thermonuclear collisions. To accomplish the latter, we first start by heating up a molecular gas; this causes low energy collisions between molecules causing them to break their molecular bonds and decompose into individual atoms. As we continue to heat up the now monatomic gas, higher energy collisions take place that separate orbiting electrons from their central nucleus, ionizing the gas. When the temperature has increased sufficiently, a majority of the atoms are ionized and the matter takes the form of a plasma. Because the plasma is composed of charged ion nuclei and free electrons, it reacts to the Lorentz force, which greatly complicates the dynamics compared to a normal gas. As we continue to heat up the plasma, nuclei undergo thermonuclear collisions once a sufficient temperature is

reached.

1.1.3 Lawson's Criterion to Achieve Fusion

Two techniques have been been successful in creating an environment on Earth where thermonuclear fusion reactions may controllably occur, inertial and magnetic confinement. While it is well known that fusion reactions happen in the core of stars between hydrogenic ions that are trapped in immense gravitational fields (for millions of years before a reaction takes place!), because we have not yet been able to create the same gravitational well to contain fusion particles here on Earth, these other confinement methods were engineered. Inertial confinement uses powerful lasers to ablate the outer shell of a target, compressing the inner fuel to create an extremely high density and temperature plasma for a very short time. Contrast this with magnetic confinement, the topic of this dissertation, which attempts to use magnetic fields to contain lower density fuel plasma at high temperatures for long times by taking advantage of the Larmor motion of charged particles.

In both techniques introduced above and also in the core of stars, the ultimate requirements for fusion are the same: a sufficient density of fuel must be held at a sufficient temperature for a sufficient amount of time (*Lawson*, 1957). For peak values of temperature $\hat{T}$ and density $\hat{n}$, this criterion is given quantitatively by

$$\hat{n}\hat{T}\tau_E > 5 \times 10^{21} \ \mathrm{m}^{-3}\,\mathrm{keV\,s}, \tag{1.1}$$

where τ_E is the energy confinement time (*Wesson*, 1987). This condition quantifies the balance between the dominant energy production and loss mechanisms, where there is more energy produced than lost when satisfied. Figure 1.3 reprinted from *Wesson* (1987), shows

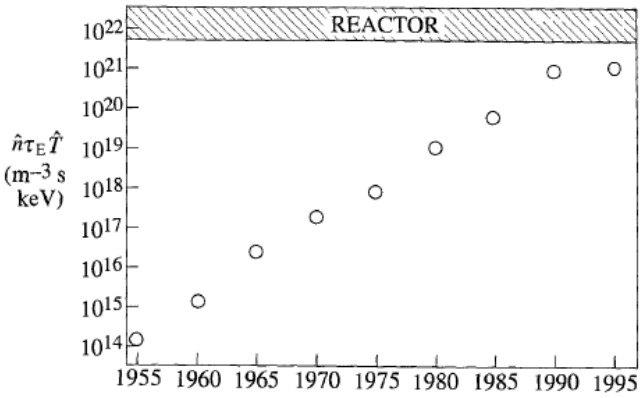

Figure 1.3: Evolution of the triple product of density, temperature, and confinement time achieved in tokamaks from *Wesson* (1987). Exponential growth was exhibited until 1990 where it has stagnated for the past decades due to hurdles in scientific understanding, technological constraints, and economic barriers.

the progress made toward this "breakeven" point in devices called tokamaks, the favored device of the magnetically confined fusion community discussed in the next section. Since 1955, the achieved triple-product has exhibited exponential growth similar to Moore's law, and while Fig. 1.3 shows growth slowed in the 1990's, the breakeven point continues to be approached by current and planned machines [e.g. *Webster* (2003)].

1.1.4 Tokamaks

Magnetic fields are useful for containing the charged particles in a fuel plasma due to the nature of the magnetic force. Mathematically, this part of the Lorentz force is described (in Gaussian units) by the equation

$$\mathbf{F_B} = q\frac{\mathbf{v}\times\mathbf{B}}{c}, \tag{1.2}$$

which shows that the resulting force is perpendicular to both the direction of motion and the magnetic field, and zero when the velocity is in the direction of the field. The consequence of the magnetic force having this form is that charged particles orbit perpendicular to the field

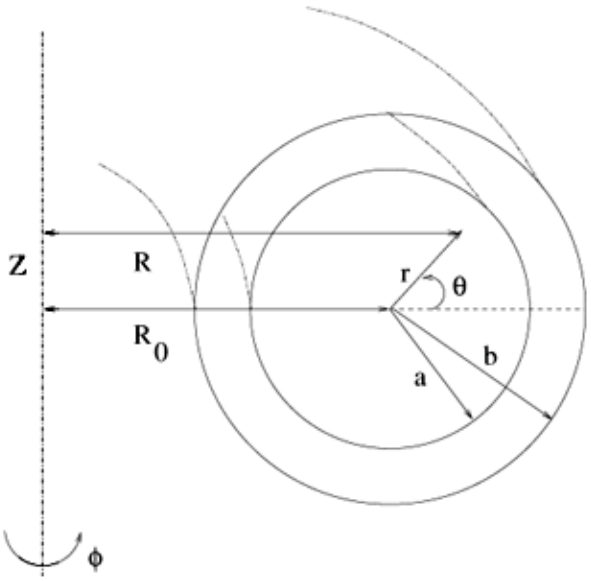

Figure 1.4: Coordinate systems utilized to quantify tokamak dynamics from *Caldas et al.* (2002). Cylindrical (R, ϕ, Z) and quasi-toroidal coordinates (r, ϕ, θ) are shown where ϕ is the toroidal direction along a circle of major radius R_0, and θ is the poloidal direction in the plane normal to $\hat{\phi}$ along a circle of minor radius r.

direction at a radius determined by particle energy and local field magnitude in a direction prescribed by Lenz's law, and move unimpeded along the direction of the magnetic field; this is a description of the Larmor motion mentioned previously in the context of magnetically confined fusion.

The magnetic field can be thought of as lines that are aligned with the local direction of the field and have a spatial density proportional to the magnitude of the field. With this interpretation in mind, for a uniform field, charged plasma particles are constrained to move in helices having their axes along magnetic field lines. By creating a magnetic field configuration in which field lines wrap around upon themselves into a torus, we can hope to confine a plasma for long times; this is the main principle behind magnetic confinement.

However, for a magnetic field generated by a current along the Z axis, as sketched in Fig. 1.4, the magnetic field decreases like $1/R$, where R is the major radius defined from the

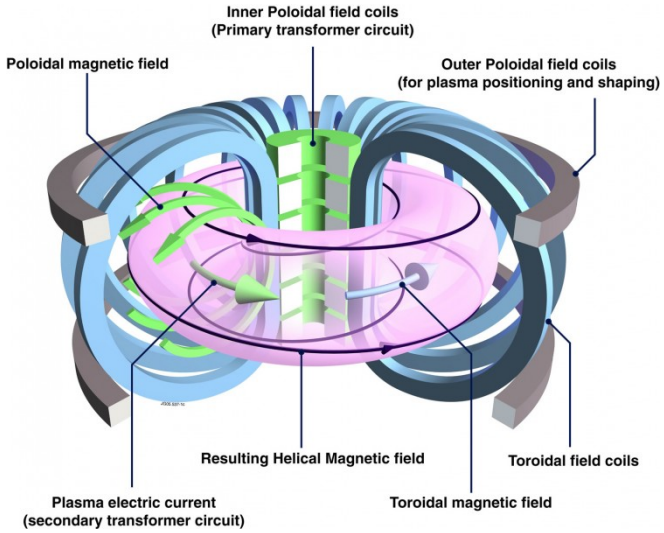

Figure 1.5: Schematic diagram of a tokamak from www.efda.org (EFDA-JET). Shown are the poloidally and toroidally aligned current coils, which set up the toroidal and poloidal magnetic field components that combine to create the resulting helical magnetic field containing the tokamak plasma. Also represented is the primary and secondary transformer circuits used to ohmically drive toroidal current in the plasma.

azimuthal axis of the torus in the cylindrical coordinate system (R, ϕ, Z). At the center of the plasma column, the major radius is denoted as R_0; we refer to the inboard side of the torus where $R < R_0$, and the outboard side of the torus where $R > R_0$. Additionally, the minor radial location r of the quasi-toroidal coordinates (r, ϕ, θ) increases outward from R_0. Completing the coordinate systems, ϕ is the toroidal direction along a circle of constant R, and θ is the poloidal direction in the plane normal to $\hat{\phi}$ along a circle of constant r.

Due to the gradient in magnetic field strength, the Larmor radius of plasma particles changes throughout an orbit, causing particles to drift perpendicular to the field direction and out of confinement! To combat these particle drifts, another component of magnetic field perpendicular to the first must be added so particle drifts offset while traveling around the device; the original (and dominant) field is in the toroidal direction, and the perpendicular field is in the poloidal direction. A tokamak is a device that has a helical magnetic field composed of toroidal and poloidal components, as sketched in Fig. 1.5.

Tokamaks are devices composed of poloidal and toroidal current coil loops, which also includes the current driven toroidally through the contained plasma as depicted in Fig. 1.5. The magnetic configuration of toroidal and poloidal fields is consistent with Ampère's law $(4\pi/c)\mathbf{J} = \nabla \times \mathbf{B}$, where the poloidal currents generate the toroidal field and vice versa. By carefully constructing the external current coils, and driving a controlled current through the plasma, the resulting magnetic fields wrap around the torus helically, and be bound to closed, nested surfaces; in this way, closed two dimensional magnetic field surfaces can be used to contain plasma in a three dimensional shape. Trying to contain the plasma in this way was once described at the first unofficial Sherwood Fusion Theory meeting in 1955 by Edward Teller (*Chen*, 2011) as, "It's like holding jello with rubber bands!" This description remains applicable today.

1.1.4.1 Tokamak Operation

Magnetic fields have proven useful for containing plasma for relatively long times, but to stimulate fusion reactions, the plasma must also be heated to high temperatures. While it is possible to heat the plasma Ohmically from collisions of the particles flowing in plasma currents, we discuss in a later section that charged particles collide less frequently at higher temperatures, limiting the usefulness of this mechanism. Several tools have been engineered to heat the plasma, including neutral beam deposition and resonant electromagnetic (EM) wave heating.

Neutral beam deposition works by accelerating ions outside of the tokamak, and then directing them through a neutralizing electron bath and into the device. While charged particles are deflected by the confining magnetic fields, neutral particles can cross these fields and deposit their energy into the plasma through collisions. Neutral beams also impart

their momentum through these collisions, which is a source of toroidal rotation appearing in tokamak plasmas. The plasma can also be heated by Landau damping of lower hybrid (LH) waves, which arise in plasmas due to density gradients. By using an antenna that launches EM waves with a frequency at the LH frequency, LH waves are driven in the plasma. LH waves then Landau damp with particles flowing near their propagation speed, coupling their energy into plasma, thereby heating it. Another non-inductive heating technique is also particularly useful for driving currents locally in the plasma, ion and electron cyclotron resonance heating and current drive. Because charged plasma particles gyrate in Larmor orbits, circularly-polarized EM waves can be resonantly matched to the gyration (cyclotron) frequency of ions and electrons, coupling their energy through cyclotron damping. As we discuss in the next chapter, the cyclotron frequency depends on the local magnetic field, so wave energy is only coupled to the charged particle populations in a well defined location, driving currents and heating the plasma locally.

Using non-inductive heating methods along with neutral beam deposition, a tremendous amount of energy is available to couple into a tokamak plasma. A recent major surprise in tokamak research was that after a sufficiently large amount of energy is coupled into the system, the plasma configuration spontaneously transforms into a high-confinement configuration (H-mode), exhibiting a sharp gradient in the gas pressure near the outward edge of the plasma column. This configuration exhibits lower levels of particle and energy transport across the newly formed edge barrier. While H-mode has become the preferred operating configuration in tokamaks, it still holds the danger of disruptions and other deleterious transient events. Disruptions are a complete breakdown of plasma confinement, where all the contained energy is released simultaneously, while transient events are a temporary leak of plasma and thermal energy; both have the capability to damage the tokamak vessel. These

issues still remain, but are currently being addressed leading up to the construction of the first international tokamak experiment, formerly known as the International Thermonuclear Experimental Reactor, and now simply as ITER.

1.1.5 Rational Surfaces and instabilities

A convenient way to describe the magnetic configuration is to trace the magnetic field starting from an initial position for many toroidal windings N and take the ratio with the number of poloidal revolutions M along the path; this is known as the safety (or quality) factor $q(r) \equiv N/M$. Simply put, the safety factor describes the "twistedness" of the magnetic field. In general, the safety factor varies with location, which is consistent with a sheared magnetic field that changes direction as one moves out in r.

It should be noted that q averages the magnetic field twist over the poloidal and toroidal directions, limiting its usefulness in describing local phenomena. However, when the magnetic field lines are assumed to have toroidally axisymmetric circular cross-sections and a large aspect ratio R/r, setting $R \sim R_0$, the safety factor can be conveniently expressed as

$$q(r) = \frac{rB_\phi(r)}{R_0 B_\theta(r)}, \tag{1.3}$$

where B_ϕ and B_θ are the toroidal and poloidal magnetic fields. In standard tokamak configurations, this value often has a minimum around 1 in the core and monotonically increases toward the edge to ~ 5.

For the locations where N and M take integer values, q is a rational number, and magnetic field lines close upon themselves. These closed field lines are more susceptible to being unstable to perturbations. To model these perturbations in a tokamak, which has periodicity

in the toroidal and poloidal directions, we Fourier transform system variables, denoted in general by f, over ϕ and θ. For a circular cross section, perturbations take on the form

$$\tilde{f}(r,\theta,\phi) = \tilde{f}(r)e^{i(m\theta - n\phi)}, \tag{1.4}$$

where $\tilde{f}(r)$ is the amplitude of the perturbation, and m, n are the poloidal and toroidal mode numbers, respectively. Note that the mode numbers m, n are different from the winding numbers M, N.

Perturbations that lead to instabilities are ones that decrease the potential energy. Because stretching or bending magnetic fields requires an input of energy, the most important (unstable) perturbations are those that do not bend or stretch field lines. These perturbations only shift the field, and are quantified by the relation (*Bateman*, 1978)

$$\mathbf{b} \cdot \nabla \tilde{f} = 0, \tag{1.5}$$

where $\mathbf{b} = \mathbf{B}/|B|$ is the direction of the local magnetic field. For plasma columns with circular cross-section, $b_r = 0$, so writing Eq. 1.5 with perturbations of the form in Eq. 1.4 gives

$$\mathbf{b} \cdot \nabla \tilde{f} = -b_\phi \frac{in}{R_0}\tilde{f} + b_\theta \frac{im}{r}\tilde{f} = 0, \tag{1.6}$$

where a large aspect ratio ($R \sim R_0$) was assumed. This is satisfied for helical magnetic fields in a direction given by

$$\hat{h} \equiv \hat{\phi} + \frac{nr}{mR_0}\hat{\theta}, \tag{1.7}$$

corresponding to helices of a circular cross-section with different pitch given by m, n. Writing the total magnetic field $\mathbf{B} = B_\phi\hat{\phi} + B_\theta\hat{\theta}$ in terms of $\hat{h}$ instead of $\hat{\phi}$, we find $\mathbf{B} = B_\phi\hat{h} + B_*\hat{\theta}$,

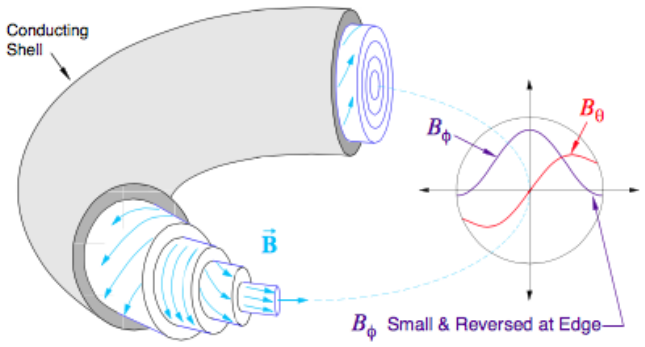

Figure 1.6: The Madison Symmetrical Torus (*Sarff et al.*, 2005) is a reversed field pinch (RFP) that is similar to a tokamak, in that it is composed of nested magnetic surfaces that are sheared relative to each other. At rational surfaces in both tokamaks and RFPs, perturbations drive tearing and magnetic reconnection where dissipative process allow magnetic energy to be converted into kinetic energy of driven plasma jets.

where

$$B_*(r) = B_\theta - \frac{nr}{mR_0}B_\phi = B_\theta\left(1 - \frac{n}{m}q\right). \tag{1.8}$$

Thus, on surfaces satisfying $q = N/M = m/n$, where magnetic fields close upon themselves, $B_* = 0$ and the direction of the magnetic field is aligned with $\hat{h}$. On these aptly named "rational surfaces", perturbations trigger the magnetic configuration into releasing its energy through various instabilities depending on the particular rational surface. From a plasma physics perspective, a large part of the reason tokamaks are not yet used for widespread power production is due to instabilities distorting or breaking magnetic surfaces.

1.2 Sawteeth

1.2.1 Tearing and Reconnection

While electric currents flowing through the plasma of a tokamak are needed to maintain the toroidally nested magnetic surfaces, they are also a source of energy that can drive instabilities. The instabilities of import to the present study are tearing and reconnection,

which occur where magnetic fields change direction and draw their energy from gradients in the current profiles. Magnetic field lines on adjacent nested magnetic surfaces in a tokamak typically have a nonzero amount of relative shear, so the magnetic field B_* projected onto the plane perpendicular to the local field direction at the rational surface ($\hat{h}$ from the last section if the cross section is circular) changes direction at the rational surface, making it prone to reconnection. We define this plane as the reconnection plane for reasons that will soon become apparent. The relative shear between adjacent nested surfaces is shown in Fig. 1.6 for a different toroidal configuration known as a reversed field pinch.

By Ampère's law, an antiparallel magnetic field configuration is consistent with a current profile peaked where the field exhibits the greatest amount of shear, which for a tokamak is generally in the vicinity of the rational surface. If the width of the current profile becomes sufficiently narrow, or rather a sufficiently large magnetic shear is present, dissipative processes (e.g. collisions and electron inertia) allow for magnetic field lines to break and reconnect (*Dungey*, 1953; *Sweet*, 1958; *Parker*, 1957). For small perturbations from the equilibrium (the linear regime) this process is known as tearing (*Furth et al.*, 1963), and when the perturbations grow large (the nonlinear regime) it is known as magnetic reconnection[2].

The reconnection process is sketched in Fig. 1.7. In the top panel, the oppositely directed components of the equilibrium magnetic field in the inflow regions of the reconnecting plane are flattened. When the field is able to break and reconnect, it cross connects to form the configuration in the bottom panel of Fig. 1.7. Plasma jets are driven in the outflow regions as these newly reconnected field lines release their tension. Due to mass continuity this induces an inflow of plasma from upstream toward the reconnection site. The inflow also brings in

[2]Since tearing and reconnection are essentially different limits of the same process, for much of the remainder unless otherwise noted, the term reconnection is understood to include both processes.

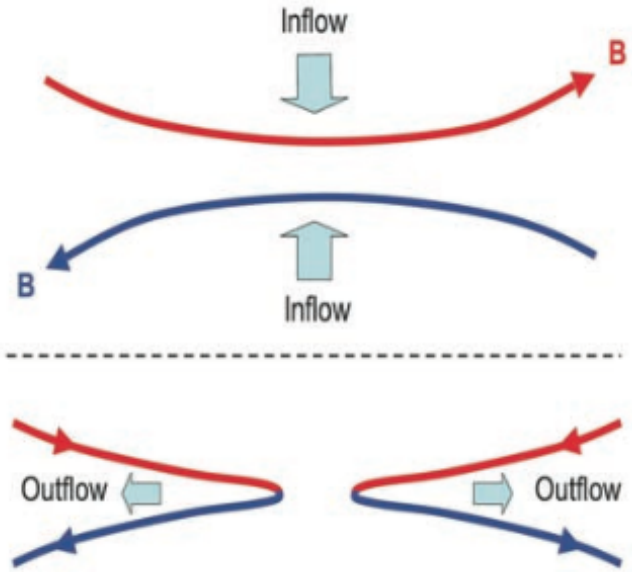

Figure 1.7: An illustration of the magnetic configuration of tearing and magnetic reconnection (*Cowley et al.*, 2007). Magnetic fields in the inflow region convect toward the X-line, where dissipative effects allow them to break and reconnect. These strongly bent fields subsequently release their tension in the outflow region, driving plasma jets and inducing additional inflow due to mass continuity.

additional magnetic flux, *so the process is self-reinforcing.* Where the inflow and outflow regions meet at the center of the reconnection site is often referred to as an "X-line"

It is also observed that the magnitude of the magnetic field in the outflow regions is greatly diminished from that in the inflow regions, suggesting a conversion of magnetic energy in the inflow region into kinetic energy of the outflow jets. By a simple scaling argument balancing the magnetic energy density in the inflow region $B_{rec}^2/8\pi$ with the kinetic energy density in the outflow region $m_i n v_{out}^2/2$, *Parker* (1957) showed the jets have an outflow speed v_{out} of

$$v_{out} \sim \frac{B_{rec}}{\sqrt{4\pi m_i n}} = c_A, \tag{1.9}$$

the Alfvén speed based on the magnetic field strength of the inflow region.

In tokamaks, where magnetic reconnection takes place on rational surfaces, the nested

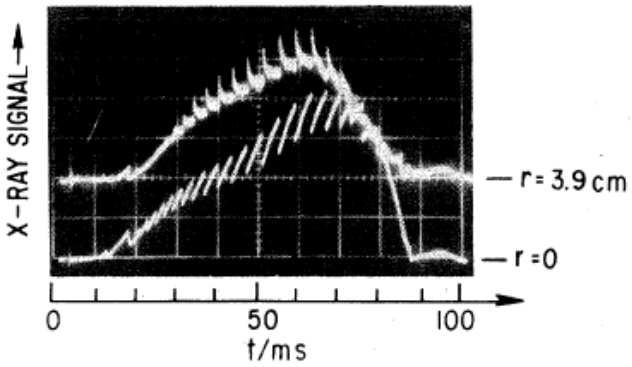

Figure 1.8: The first observation of sawteeth in the ST tokamak (*von Goeler et al.*, 1974). Intensity of soft X-rays from electron bremsstrahlung emission are proportional to the square root of the electron temperature. The signal from the core (bottom trace) shows a slow rise phase followed by a rapid crash phase, while a signal from the edge (top trace) shows the reverse process, signifying a substantial thermal transport during the sawtooth crash.

magnetic surfaces that used to be topologically isolated are now connected, and the hot plasma in the interior can get out to the exterior. Reconnection usually starts abruptly, leading to a rapid loss of confinement.

1.2.2 Early Observations and Model

When magnetic reconnection occurs at the $q = 1$ rational surface, the resulting explosive transport of thermal energy is known as the sawtooth crash. The sawtooth was first observed by *von Goeler et al.* (1974) in the X-ray emission due to electron bremsstrahlung in the Symmetric Tokamak (ST); the time history of X-ray emission during an ST discharge is shown in Fig. 1.8. The two traces correspond to the electron temperature at locations in the core ($r = 0$) and edge ($r = 3.9$ cm); the oscillatory pattern earned it the name sawtooth. The core trace shows a slow rise phase (~ 5 ms) followed by a rapid crash, while the edge trace shows a slow decline followed by a spike. This is a strong indication that there is a sudden transport of particles and thermal energy out of the high temperature core, which decreases the core temperature and confinement of the plasma. Remembering that the Lawson criteria

in Eq. 1.1 requires the temperature and confinement to be high, sawteeth are deleterious for fusion reactions.

This observation was first explained by *Kadomtsev* (1975) as a magnetic reconnection event of the $(m, n) = (1, 1)$ resistive tearing mode. The perturbation that drives the energy release at the $q = m/n = 1$ surface comes from the internal kink mode, an ideal-magnetohydrodynamic (MHD) instability [e.g. *Freidberg* (1987)]. As current is driven in the toroidal plasma column it tends to be peaked centrally, increasing the poloidal field B_θ in the interior, and from Eq. 1.3 lowering the central safety factor $q_0 = q(r = 0)$. When the central safety factor satisfies $q_0 < 1$, the internal kink mode is unstable (*Bussac et al.*, 1975). The physics of the kink instability is that perturbations bend the plasma column and produce a gradient in the poloidal magnetic pressure, which leads to a force that reinforces the perturbation.

In Kadomtsev's model, the time it takes for the crash to occur is the time for reconnection to process *all* of available magnetic flux in the core. Equivalently, the safety factor q exceeds 1 everywhere after the event; this is called "complete reconnection", and is an important aspect of Kadomtsev's model. Crash times were consistent with the time it takes resistive Sweet-Parker reconnection to process all available magnetic flux ($\sim 30\ \mu s$ for the ST tokamak), and early simulations (*Sykes and Wesson*, 1976; *Denton et al.*, 1986) were largely consistent with this picture.

1.2.3 Additional Experimental Observations

Sawteeth are a near-ubiquitous feature of tokamaks, appearing across different machines with a variety of discharge parameters. In this section, we discuss several interesting results of relevance to the present work.

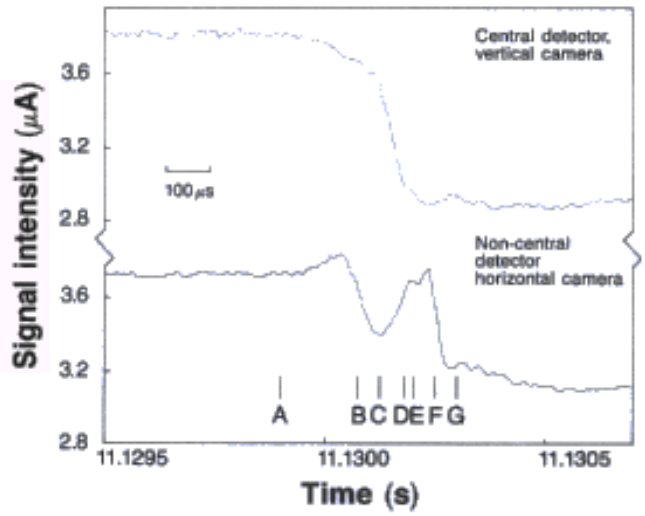

Figure 1.9: Figure (1) adapted from *Edwards et al.* (1986) that shows the central and a non-central soft X-ray detector data during a sawtooth crash phase in JET. The timescale of the crash phase orders on 100 μs, and evidence of the $(m, n) = (1, 1)$ mode is seen in the data from the off-center trace.

While the von Goeler observation was indicative of internal transport of core plasma on a much faster timescale than the total discharge time, the spatial resolution of the soft X-ray diagnostic was too low to diagnose the evolution of the sawtooth mode. Shortly after, on the Joint European Torus (JET) in the early 1980s, multiple upgraded, soft X-ray detectors were arranged to provide high temporally resolved ($\sim$ μs) and 2D tomographically resolved ($\sim$ 8 cm) signals of the plasma electron temperature (*Edwards et al.*, 1986). In Fig. 1.9, we show the expanded view of the central and a non-central detector from Fig. (1) of *Edwards et al.* (1986). The top trace shows the crash phase of a sawtooth cycle from the central detector, exhibiting a timescale the order of 100 μs. The bottom trace shows the data from an off-center detector that is much more complicated, suggesting a complex evolution of the central region of the plasma.

The times denoted by letters in Fig. 1.9 correspond to tomographical reconstructions of the electron temperature shown in Fig. 1.10. During the early evolution, the shift of

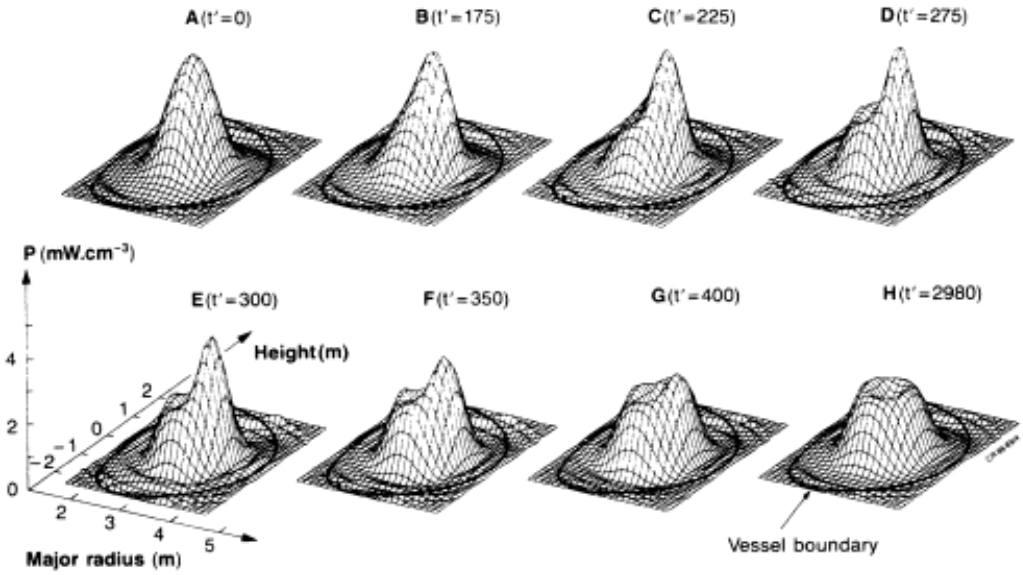

Figure 1.10: 2D tomographical reconstructions of soft X-ray data from JET (*Edwards et al.*, 1986) corresponding to the times given in Fig. 1.9. Seen are the early evolution of the kink mode (A&B), the processing of the core plasma during the reconnection phase (C-G), and the complete reconnection of the core (H).

the plasma core due to the kink mode can clearly be seen, giving way to reconnection in (C). The reconnection process continues, as implied by the shrinking hot core, until it fully processes the core plasma sometime between (G) and (H). Reconnection is complete for this sawtooth cycle consistent with Kadomtsev's model. However the timescale of the crash is much quicker than expected for this discharge, which was estimated to be on the order of several milliseconds. This discrepancy is due to the model assuming resistive reconnection of the $(m, n) = (1, 1)$ mode. Resistivity is modelled in plasmas by electron-ion collisions, where $\eta \equiv m_e \nu_{ei}/ne^2$ is the collisional resistivity, and ν_{ei} is the electron-ion collision frequency which is proportional to $n/T_e^{3/2}$ (*Spitzer and Härm*, 1953). JET had $T_e \sim 4$ keV, while ST had $T_e \sim 0.7$ keV, so due to the inverse 3/2-power dependence of the electron temperature in the resistivity, neglecting other effects, the crash time is estimated to be ~ 14 times longer, but was observed to be only ~ 3 times longer. This suggests that additional physics is

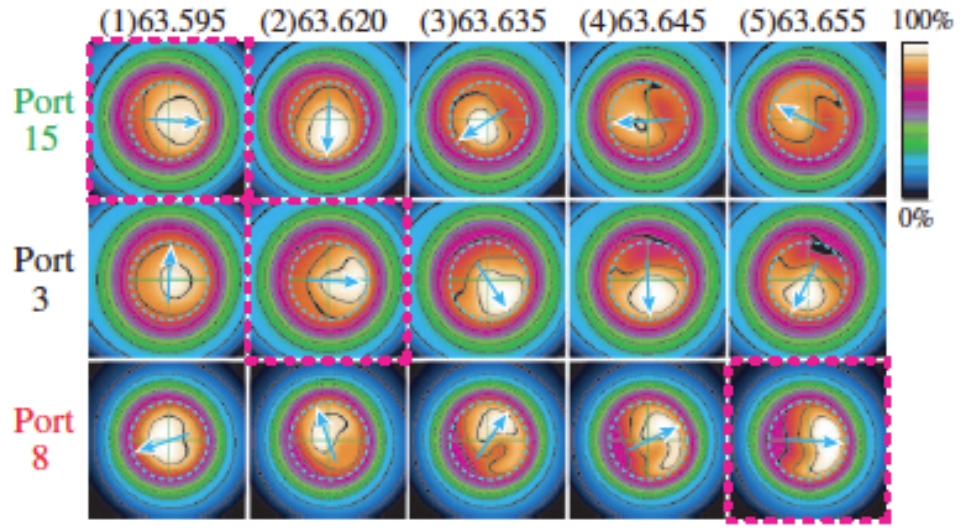

Figure 1.11: Toroidally resolved soft X-ray data from the WT-3 tokamak (*Yamaguchi et al.*, 2004). Data from ports 15, 3, and 8 are at toroidal angle $\phi = 0^{\circ}$, 90°, and 202.5°. The reference time is given in milliseconds, the blue arrows indicate which edge of the device the mode is offset towards, the red dashed boxes indicate where the helical mode intersects the outboard side of the device, and the dashed white circles show the $q = 1$ rational surface. With the toroidal plasma current opposite to the toroidal direction, the helical mode has a counter-clockwise polarity, and with a neutral beam causing rotation in the positive toroidal direction, the mode is observed to rotate in the clockwise poloidal direction.

needed to properly explain the crash time of sawteeth; we discuss this topic more in the next chapter.

Kadomtsev's model described the sawtooth crash as a reconnection event of the $(m, n) = (1, 1)$ mode, and the non-central detector data in Fig. 1.9, along with the 2D tomographical reconstruction in Fig. 1.10, shows a non-trivial behavior in the evolution of the electron temperature. As was discussed in Sec. 1.1.5, the helical $(m, n) = (1, 1)$ mode wraps around the tokamak, so viewing data from a single toroidal angle misses out on important information on how the mode evolves. It was not until the WT-3 tokamak was built in the early 2000s that multiple soft X-ray detector arrays were placed around the device at different toroidal angles (*Yamaguchi et al.*, 2004). On WT-3, detector arrays were positioned at $\phi = 0^{\circ}$, 90°, and 202.5°, in the 15th, 3rd, and 8th diagnostic ports, respectively. Data from the beginning

of the sawtooth crash phase can be seen in Fig. 1.11, where the reference time is given in milliseconds and the total elapsed time is 60 microseconds.

For this discharge, the plasma current is directed oppositely to the toroidal magnetic field in the positive toroidal direction, giving the reconnection mode a counter-clockwise helical polarity. With a neutral beam causing rotation in the positive toroidal direction, the mode is observed to rotate in the clockwise poloidal direction, as expected. Aside from the observation that the mode rotates, it is also apparent that the poloidal location of reconnection affects the structure of the electron temperature. When the hot core is offset towards the outboard side, the electron temperature profile elongates along the $q = 1$ surface. Furthermore, when the core is offset towards the top or bottom, there is an asymmetry of the temperature towards the outboard side.

1.2.4 Impact of Sawteeth

In more than 40 years since the first observation of sawteeth, the fusion community has come to better understand their role in the containment of fuel plasma and general operation of tokamaks. Many of the diagnostics developed to probe the internal magnetic field and plasma current profiles were motivated by the need to characterize sawtooth behavior (*Soltwisch*, 1992). In the same time span, technologies have become available that allow us to heat specific populations of plasma particles and drive currents non-inductively in local regions of the plasma, largely without affecting the rest of the tokamak, by resonantly coupling injected wave energy to the gyromotion of the charged plasma particles as discussed in Sec. 1.1.4.1. It was demonstrated that energetic ions have a stabilizing effect on sawtooth dynamics (*Porcelli*, 1991), whether the energetic ions are from fusion-born alpha particles or non-inductively heated populations (*Porcelli et al.*, 1996). Additionally, currents driven

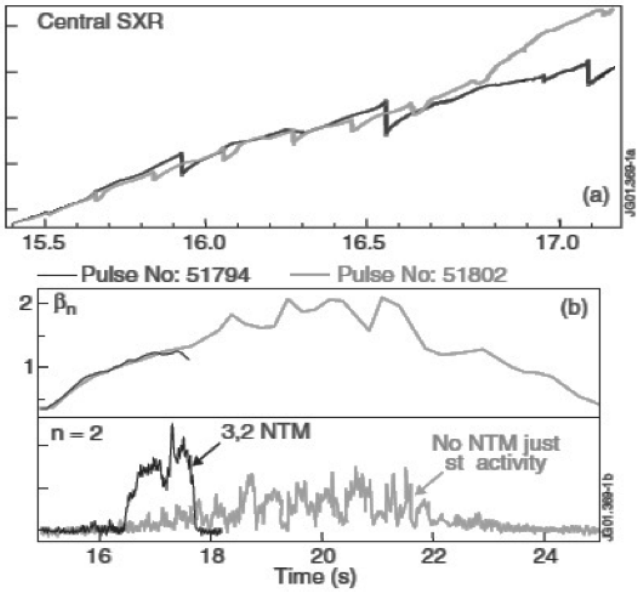

Figure 1.12: Soft X-ray observations of sawteeth with periods that were increased (black trace) and decreased (grey trace) by non-inductively driving ions in JET (*Sauter et al.*, 2002). Delayed sawteeth are seen to trigger an $(m, n) = (3, 2)$ NTM, while triggered sawteeth do not couple their energy into these deleterious modes.

by non-inductively energized charged particles have been used to directly trigger sawteeth [see *Chapman* (2011a) for a review], by changing the magnetic shear locally at the $q = 1$ rational surface (*Prater*, 2004).

Without the use of control techniques, the sawtooth period and amplitude vary and in some cases can lead to catastrophic "monster sawteeth", where the internal kink mode is stabilized for long times until it is terminated by a large crash (*Campbell et al.*, 1986). These sawteeth are often more violent and more likely to trigger neoclassical tearing modes (NTMs). NTMs (*Chang et al.*, 1995) arise on higher numbered rational surfaces, most notably $(N, M) = (3, 2)$ and $(2, 1)$ surfaces, and act similarly to sawteeth but much closer to the edge of the plasma. They allow for much faster thermal transport and can lead to full tokamak disruptions (*La Haye et al.*, 1997). By triggering the crash with non-inductive current drive, the sawtooth period can be shortened, with relatively smaller crashes that

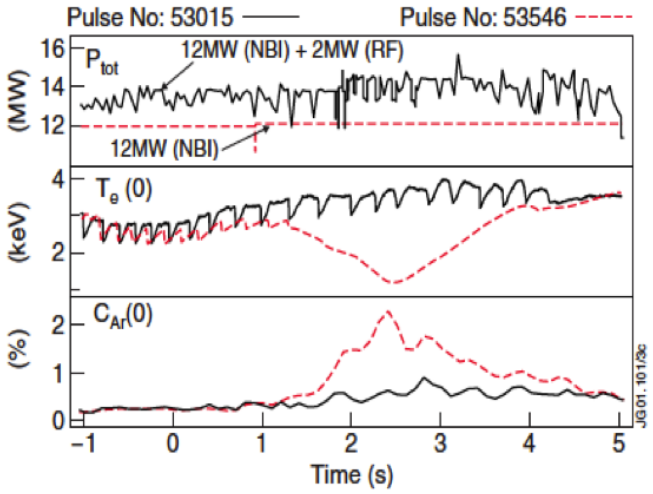

Figure 1.13: The presence of sawteeth correlate well to decreased levels of impurities in the plasma core in JET (*Nave et al.*, 2003). Ar impurity injection was used to enter H-mode, and when sawteeth stabilized (red trace) Ar impurities accumulated in the core, leading to large levels of radiative bremsstrahlung losses. However, when ions were driven non-inductively, sawteeth were maintained and the core impurity density was limited.

are less likely to trigger NTMs. In Fig. 1.12, data is shown from JET (*Sauter et al.*, 2002), where energetic ion populations were driven to lengthen and shorten the sawtooth period in order to control NTMs. This is seen in the top panel, where the black trace shows where the sawtooth period was lengthened and the grey trace shows where the sawtooth period was decreased. The bottom figure in the lower panel shows the magnetic signal for $n = 2$ modes and, when the sawtooth period is elongated, it is seen that a $(m, n) = (3, 2)$ NTM is triggered.

The main effect of sawteeth is the expulsion of hot plasma from the core of the tokamak, mediated by the change in magnetic topology at the $q = 1$ rational surface that allows particle transport. This is important for several of the energy loss mechanisms factoring into Eq. 1.1, one of those being the bremsstrahlung radiation of accelerating charged particles compromising the fuel plasma. The radiated energy is proportional to the square of the accelerating charge: for hydrogenic species this is small where the atomic number is $Z = 1$,

but the heavier particles making up the confinement vessel have much larger Z and the radiation losses are much greater. In *Nave et al.* (2003), JET discharges in high-confinement (H-mode) with Ar injection were observed to be free of sawteeth, and were accompanied by increased levels of Ar in the tokamak core as seen in Fig. 1.13; this led to a sudden and unexpected loss of containment. However, when ions were used to non-inductively drive current to alter the q-profile and stimulate sawteeth, the core impurity density was limited and good confinement was maintained throughout the discharge. Thus, sawteeth can be beneficial despite their other deleterious effects.

In this section, we discussed the impacts of sawteeth on tokamak operation. While sawteeth allow for the adverse transport of hot fuel plasma from the core, their absence gives rise to unfavorable conditions as well. Thus, controlling sawteeth should be the desired operating scenario in tokamaks. However, this requires a more complete knowledge of the underlying physics of sawteeth.

1.3 Incomplete Reconnection in Sawteeth

1.3.1 Observations

We saw in the last section that the sawtooth period can be controlled by utilizing methods that non-inductively heat and drive currents in the plasma, for either triggering or delaying the crash onset. However, there is much less understanding of the duration of the sawtooth crash phase. While the model in Sec. 1.2.2 was successful at explaining sawtooth phenomena and timing initially [e.g. *McGuire and Robinson* (1979)], crash times in the larger and hotter tokamaks JET (*Edwards et al.*, 1986; *Wesson et al.*, 1991) and TFTR (*Yamada et al.*, 1994) (~ 100 μs) were much faster than Kadomtsev's prediction (several milliseconds) as discussed

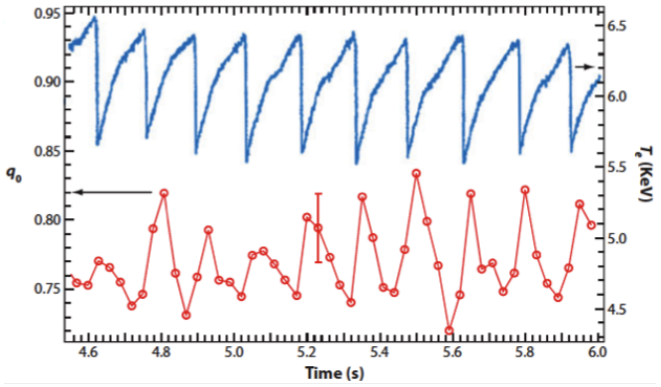

Figure 1.14: Observations of incomplete sawteeth in TFTR (*Yamada et al.*, 1994). The blue trace corresponds to the central electron temperature, which shows the standard sawtooth oscillation. The red trace shows that the central safety factor always satisfies $q_0 < 1$, which signifies excess unreconnected magnetic flux at the end of the crash phase.

in Sec. 1.2.3. Several of these faster crash times were accompanied by the curious observation of "incomplete reconnection", meaning the central safety factor q_0 remains below 1 and not all available magnetic flux is reconnected by the end of the crash phase. This was also observed at Tokapole II (*Osborne et al.*, 1982), TFR (*Dubois et al.*, 1983), TEXT (*West et al.*, 1987), TEXTOR (*Soltwisch*, 1988), JET (*Campbell et al.*, 1988), PBX-M (*Levinton et al.*, 1989), DIII-D (*Wroblewski and Lao*, 1991), MTX (*Rice*, 1992). Note that not all sawteeth are incomplete either; q_0 was near 1 in sawteeth in ATC and ASDEX [e.g. *Soltwisch* (1992)]. An example of the time history of q_0 (red trace) and central electron temperature T_e (blue trace) for incomplete sawteeth on TFTR (*Yamada et al.*, 1994) is in Fig. 1.14. The observation that the safety factor in the core never rises above one throughout the temperature oscillations indicates that there is still magnetic flux in the core that is available to undergo magnetic reconnection.

Incomplete sawteeth continue to be actively researched, helped in part by the advancement of diagnostic systems. As an example, a recently upgraded Thomson scattering diagnostic system on the Mega Ampere Spherical Tokamak (MAST) has shown incomplete

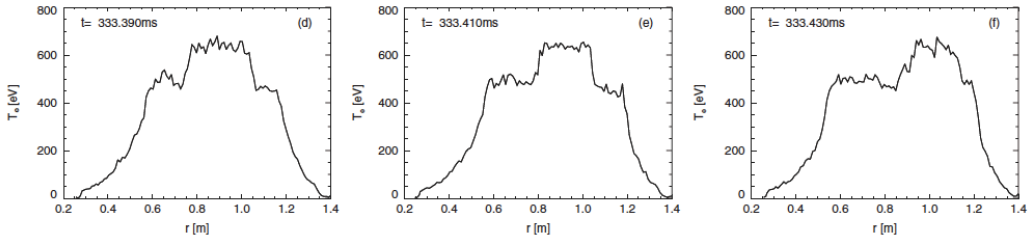

Figure 1.15: Thomson scattering measurements towards the end of a sawtooth crash cycle on MAST (*Chapman et al.*, 2010). The high time and spatial resolution of the upgraded diagnostic system allows the observation of a transition from a well-confined core in the second frame to turbulence in the third frame.

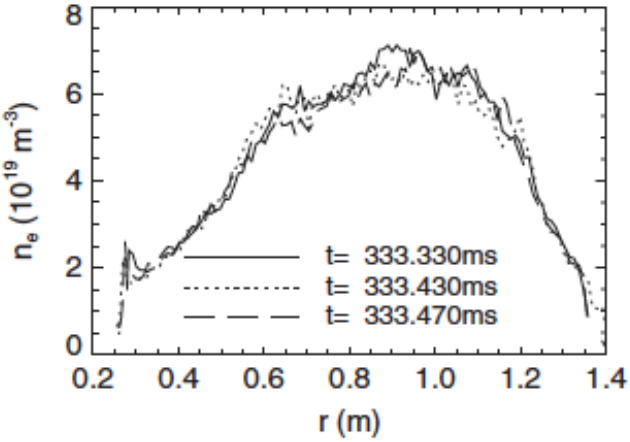

Figure 1.16: Profiles of the electron density during the MAST discharge shown in Fig. 1.15 as reproduced from *Chapman et al.* (2010). Since the density remains approximately constant as the temperature completely relaxes, reconnection during the sawtooth crash phase is incomplete.

reconnection during a sawtooth cycle as seen in Fig. 1.15 reproduced from *Chapman et al.* (2010). In (d) and (e) the core is well-defined with a sharp boundary between it and the island formed from reconnection. The boundary becomes turbulent in (f), and a full relaxation of the core electron temperature takes place within 20 μs (not shown). As the core temperature relaxes, the electron density remains essentially unchanged as can be seen in Fig. 1.16; along with measurements that indicate that the central safety factor remains below 1, the observation of unchanged core density is evidence of incomplete reconnection.

While a definitive model for how reconnection evolves during the sawtooth crash phase

has been elusive, toroidal simulations with extended-MHD physics have observed partial reconnection (*Breslau et al.*, 2007). Simulated using the M3D code (*Park et al.*, 1999) with ion diamagnetic terms included, a sawtooth cycle exhibited incomplete reconnection as seen in the Poincaré plots[3] of Fig. 1.17. The first reconnection phase takes place in plots (a)-(c), and a second reconnection cycle is shown in (d)-(e) that ends before processing all the core flux, a sawtooth cycle with incomplete reconnection! Compared to a similar resistive-MHD simulation (not shown), the reconnection mode in this simulation can be observed to rotate in the poloidal direction, consistent with the addition of the diamagnetic effects, as we discuss later. While *Breslau et al.* (2007) was unable to conclude if the incomplete reconnection was due to the inclusion of two-fluid effects or a consequence of the lesser energy of the second crash, this is still the first simulation result showing incomplete reconnection in a 3D toroidal geometry.

To understand why reconnection is incomplete, one must determine how reconnection can cease despite the presence of free magnetic energy. Referring to Sec. 1.2.1, once magnetic fields break, reconnect, and subsequently release their tension, mass continuity induces inflows that bring in additional magnetic flux. To interrupt this process, there must be additional effects besides the local magnetic shear. In the previous section, we saw that another source of energy from energetic populations of plasma particles affects the reconnection process. Other possible sources of energy that could play an important role at the $q = 1$ rational surface are flow shear, pressure gradients (diamagnetic effects), and tokamak shaping. Determining which, if any, of these energy sources contribute to incomplete reconnection remains an open issue and is the main concern of this dissertation.

[3]In the context of tokamaks, Poincaré plots map where magnetic fields intersect a plane defined by a specific toroidal angle. By seeding different starting points in such a plane, the value of the local magnetic field is used to trace along the field for multiple toroidal transits. Recording where the field "punctures" the plane on each transit gives the plots shown in Fig. 1.17.

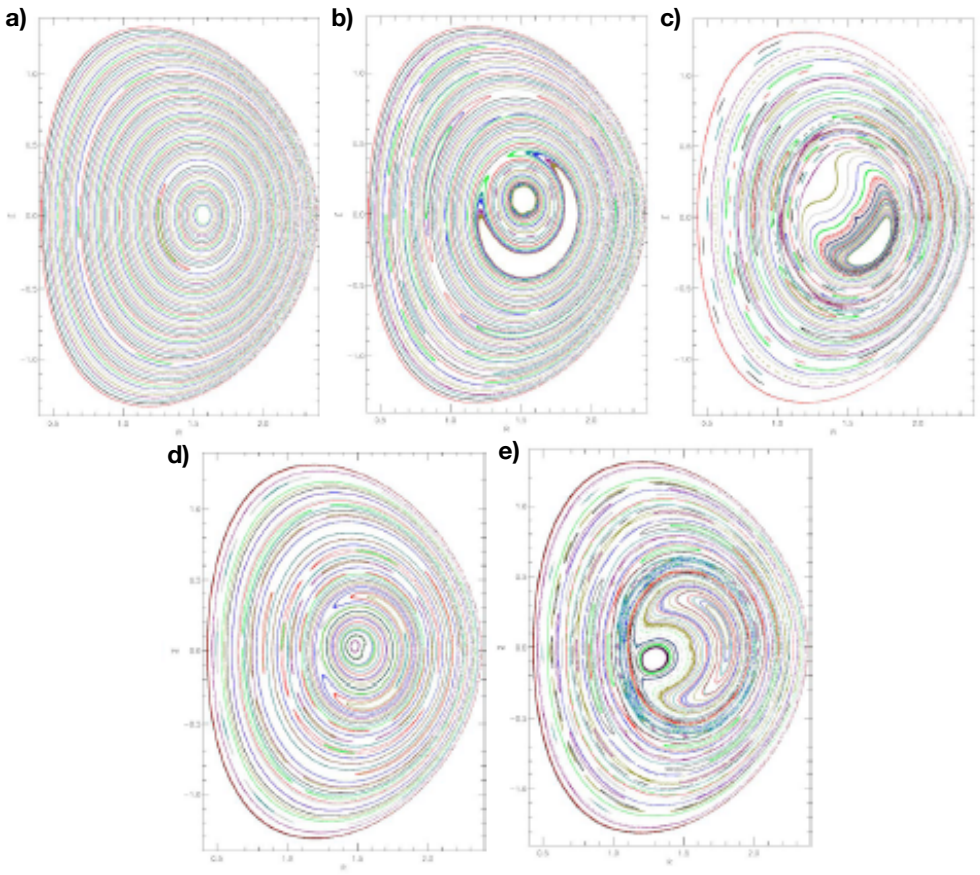

Figure 1.17: Poincaré sections showing the reconnection phases of two sawtooth cycles for extended-MHD simulations including ion diamagnetic effects (*Breslau et al.*, 2007). The first sawtooth crash (a)-(c) exhibits complete reconnection, while in the second crash (d)-(e) reconnection is incomplete. Rotation of the reconnection mode in the poloidal direction is due to the inclusion of diamagnetic effects.

1.3.2 Impact of Incomplete Reconnection

Sawtooth phenomena are projected to threaten operation in ITER [e.g. *Hender et al.* (2007)], so it is critical to accurately predict sawtooth phenomena. Sawtooth events degrade confinement of fusion alpha particles generated in the core of the tokamak, limiting their ability to transfer their energy to the plasma; the timescale of the sawtooth crash (i.e., whether reconnection is complete or incomplete) directly determines the importance of these losses. It was recently argued that fast-ion transport strongly depends on the crash time (*Muscatello et al.*, 2012), though there is no accepted model of the crash time because incomplete reconnection is not well understood.

The uncertainty of the cause of incomplete reconnection impacts tokamak transport modeling. Low-dimensional transport models capture the sawtooth period and amplitude (*Porcelli et al.*, 1996), but the fraction of flux reconnected is an input parameter rather than self-consistently calculated [e.g. *Bateman et al.* (2006)]. Therefore, a first principles self-consistent understanding of incomplete reconnection is crucial to understand transport and predict the viability of future fusion devices such as ITER.

1.4 Summary of Results

The remainder of this manuscript focuses on understanding the of role magnetic reconnection during the crash phase of sawteeth. In the next chapter, we continue by introducing collisionless reconnection, in particular how it evolves under the conditions relevant for sawteeth, where pressure gradient effects, or diamagnetic effects, play an important role. In the third chapter, we return our discussion to sawteeth, but focus primarily on models of incomplete reconnection in sawteeth. This includes the introduction of a new model detailing

how magnetic reconnection can self-consistently cease during a crash phase, and a series of two-fluid simulations in a 2D slab geometry that support the model. In the fourth chapter, we transition to simulations in a 3D toroidal geometry. By viewing the simulation data using a novel technique, we properly diagnose collisionless reconnection in 3D toroidal simulations for the first time during a sawtooth crash phase. The final chapter summarizes our work, and suggests additional interesting lines of inquiry.

Chapter 2

Review of Magnetic Reconnection

2.1 Collisionless Reconnection

With the main consideration of this work being to further understand the causes and effects of incomplete reconnection, the observation of a shorter crash time compared to Kadomtsev's theory suggests that additional physics to the resistive $(m, n) = (1, 1)$ tearing mode is necessary. Rather than the resistive (slow) reconnection model of Sweet and Parker utilized by Kadomtsev, the fast time scales of the crash phase imply that collisionless (fast) reconnection effects are important [e.g. *Biskamp* (2000)].

In order to quantify the rate of reconnection, we assume that the plasma flow is incompressible (i.e. $\nabla \cdot \mathbf{v} = 0$) outside of the region where magnetic field lines reconnect, which leads to the scaling

$$\frac{v_{in}}{\delta} \sim \frac{v_{out}}{L} \Rightarrow E_r \equiv \frac{v_{in}}{v_{out}} \sim \frac{\delta}{L}, \tag{2.1}$$

where δ and L are the respective thickness (in the inflow direction) and length (in the outflow direction) of the reconnection region, and v_{in} and v_{out} are the velocity of the flow

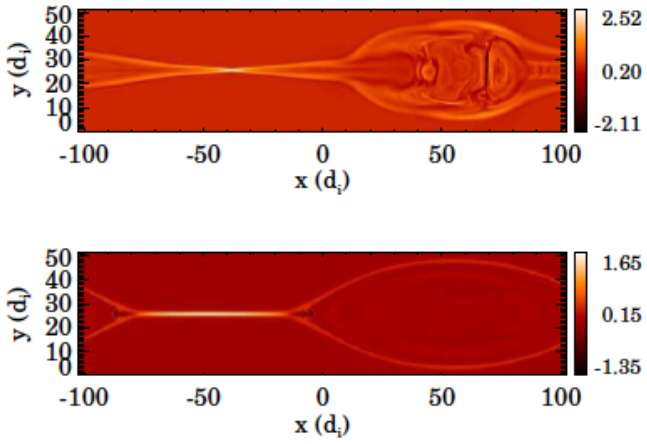

Figure 2.1: Magnetic geometry of Petschek (top) and Sweet-Parker (bottom) reconnection (*Cassak*, 2006). Note the opening angle of the reconnection site, leading to an X outflow structure and elongated outflow structure, for Petcheck and Sweet-Parker reconnection, respectively.

into and out of the reconnection region, respectively. The reconnection rate E_r, or the normalized rate at which flux is processed, is the ratio between the inflow speed and the outflow speed from the reconnection site (*Parker*, 1957). E_r was suggestively chosen to represent the reconnection rate, because E_r is also equal to the out-of-plane electric field at the reconnection site (*Vasyliunas*, 1975), which, from Faraday's law, is related to the time rate of change of magnetic flux.

In the Sweet-Parker model, the outflow speed is Alfvénic and the length of the reconnection region is set by the global scale L_g (*Biskamp*, 1986; *Scholer*, 1989a; *Uzdensky and Kulsrud*, 2000; *Jemella et al.*, 2003, 2004) as seen in the bottom plot of Fig. 2.1 from *Cassak* (2006). One can show the reconnection rate is $E_r = S^{-1/2}$ (*Parker*, 1957; *Sweet*, 1958), where $S = \mu_0 L_g c_A/\eta$ is the Lundquist number, representing the ratio between the resistive diffusion time and the Alfvénic convection time. Thus, $E_r \sim \eta^{1/2}$, and as we saw in the last chapter, η scales like $T^{-3/2}$, showing that Sweet-Parker reconnection has a lower rate at higher plasma temperatures.

To reconcile the observations of fast rates of reconnection at high Lundquist numbers in

astrophysical and space plasmas, *Petschek* (1964) proposed a model where the reconnection site is localized in the outflow direction, rather than stretching over global scales. Referring to Eq. 2.1, decreasing the outflow scale relative to the inflow scale increases the rate of reconnection, effectively decreasing the nozzle-effect and allowing more magnetic flux to be processed. However, computations (*Biskamp*, 1986) showed this geometry cannot be sustained with a simple uniform resistivity. Instead, the resistivity must increase locally at the X-line, leading to several models of *anomalous resistivity* (*Papadopoulos*, 1977; *Galeev and Sagdeev*, 1984; *Drake et al.*, 2003). We will see in Sec. 2.3 that the difference in characteristic length scales between electrons and ions due to their disparate masses allow for a Petschek reconnection geometry in the absence of collisions, as seen in the top plot of Fig. 2.1. However, the mechanism by which two-fluid effects allow this configuration to arise is still under debate.

2.2 Magnetohydrodynamics

In order to ascertain the dominant physics that controls the reconnection process in the sawtooth crash, we must begin by choosing a proper model. Rather than keeping information about each individual particle, or using a distribution function that describes the ensemble of plasma particles in phase $(\mathbf{x}, \mathbf{v}, t)$ space, we use the two-fluid model, which captures the minimum physics needed to model collisionless reconnection by treating ions and electrons as separate fluids using the framework of magnetohydrodynamics, or MHD for short. This choice is reinforced by the results of the GEM challenge, where Fig. 2.2 shows a benchmark of several models used to study reconnection (*Birn et al.*, 2001). The "Hall-MHD" model, which is similar to the two-fluid model, exhibits a comparable amount of reconnected magnetic flux

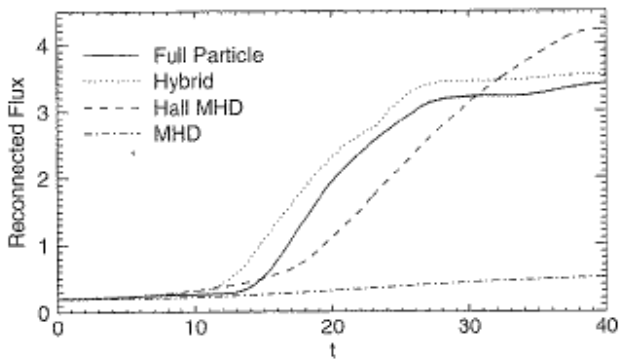

Figure 2.2: A benchmark of different models used to study reconnection in plasmas (*Birn et al.*, 2001). The models compared include resistive-MHD, Hall-MHD (similar to two-fluid), a hybrid model where ions are treated as particles and electrons are treated as a fluid, and a full particle model. While reconnection is slow for resistive-MHD, the other three models are qualitatively consistent with collisionless reconnection.

as the full particle and hybrid models, which dramatically outpaces the slower resistive-MHD model.

However, we start our discussion by describing MHD. It employs an approximation to model the different species of charged particles comprising a plasma as a single fluid, and when coupled with Maxwell's equations for electromagnetism, the resulting set of equations is MHD [e.g. *Chen* (1974)]. Additionally, we allow for collisions between the ion and electron species that enter the system of equations through Ohm's law as a resistivity; in the next section, we expand this to a "generalized Ohm's law" to include the physics of the two-fluid model, which treats ions and electrons as separate populations as contrasted to the single fluid of MHD.

The set of resistive-MHD equations include the mass, momentum, and pressure (or alternatively, energy) evolution equations, Faraday's law, Ampère's law (where the displacement current term is ordered out), and the resistive Ohm's law, given by *Forbes* (2007) in Gaussian

units as:

$$\frac{d\rho}{dt} = -\rho\nabla\cdot\mathbf{v}, \tag{2.2}$$

$$\rho\frac{d\mathbf{v}}{dt} = -\nabla p + \frac{\mathbf{J}\times\mathbf{B}}{c}, \tag{2.3}$$

$$\frac{dp}{dt} = -\gamma p\nabla\cdot\mathbf{v} + (\gamma-1)\eta J^2, \tag{2.4}$$

$$\frac{\partial\mathbf{B}}{\partial t} = -c\nabla\times\mathbf{E}, \tag{2.5}$$

$$\nabla\times\mathbf{B} = \frac{4\pi}{c}\mathbf{J}, \tag{2.6}$$

$$\mathbf{E} + \frac{\mathbf{v}\times\mathbf{B}}{\mathbf{c}} = \eta\mathbf{J}. \tag{2.7}$$

Here, $d/dt = \partial/\partial t + \mathbf{v}\cdot\nabla$ refers to the time derivative moving with the plasma, where $\partial/\partial t$ is the local time derivative and $\mathbf{v}\cdot\nabla$ is the convective derivative due to flow through a spatially varying plasma. The plasma mass density is denoted by $\rho \simeq m_i n$ for $m_i \gg m_e$, where n is the quasineutral particle density (i.e., electron and ion densities are equal $n_e \simeq n_i$), $p = p_i + p_e$ is the (isotropic) plasma pressure, and γ is the ratio of specific heats. $\mathbf{E}$ denotes the electric field, $\mathbf{B}$ is the magnetic induction field, $\mathbf{J}$ is the electric current density, and η is the collisional resistivity described in Sec. 1.2.3. Closing the hydrodynamic equations with the adiabatic equation of state in Eq. 2.4 describes convection, compression, and Ohmic heating, ignoring other effects[1].

In this formulation, the quasineutral plasma flow $\mathbf{v} = (m_i\mathbf{v_i} + m_e\mathbf{v_e})/(m_i + m_e) \simeq \mathbf{v_i} + \mathbf{v_e}(m_e/m_i)$ upon using $m_i \gg m_e$, is largely independent of the electron flow, making this "one-fluid" flow heavily dependent upon the ions. Interestingly, Eq. 2.7 is consistent with $\mathbf{E} = 0$ in the reference frame moving with the plasma [e.g. *Choudhuri* (1998)], except

[1] *Braginskii* (1965) provides a rigorous treatment, deriving the two-fluid equations from the Vlasov equation (including collisions), which describes the time evolution of the plasma distribution function.

where electron-ion collisions allow slippage of the plasma fluid relative to the magnetic field. This is known as the "frozen-in" condition, which describes how the magnetic flux through any closed surface moving with the plasma cannot change, prescribing the magnetic field and plasma move together in the absence of dissipation (*Axford*, 1984; *Choudhuri*, 1998). Combining Eq. 2.5 with Eq. 2.7 gives

$$\frac{\partial \mathbf{B}}{\partial t} = c\nabla \times \left(\frac{\mathbf{v} \times \mathbf{B}}{c} - \eta \mathbf{J} \right) \tag{2.8}$$

for the evolution of the magnetic field in resistive MHD. The first term on the right is due to convection, compression, and bending of the magnetic field, consistent with the frozen-in condition, while the second term describes diffusion of the magnetic field. Upon using Ampère's Law, the effect of diffusion on magnetic field evolution scales like

$$\frac{\partial \mathbf{B}}{\partial t} \sim \frac{\eta c^2}{4\pi} \nabla^2 \mathbf{B}. \tag{2.9}$$

In Sweet-Parker reconnection, this diffusion is what allows the magnetic fields to break and convert their energy into the kinetic energy of the reconnection outflows and heat; it is this type of reconnection that Kadomtsev's model of sawteeth uses. However, for higher temperatures in modern tokamaks such as DIII-D, Kadomtsev's resistive reconnection timescale is on the order of 1 ms, while observed crash times are on the order of 40 μs (*Lazarus et al.*, 2006). As discussed earlier, because the Spitzer resistivity is inversely proportional to $T_e^{3/2}$, as temperatures increase the magnetic diffusion time increases as well, while the sawtooth crash time is observed to remain approximately constant.

However, when electrons are treated independently from the ions in a plasma, their presence gives rise to dynamics on much faster time scales than diffusion alone, and their

inertia allows for the breaking of magnetic fields even in the absence of collisions.

2.3 Two-fluid Physics in Reconnection

2.3.1 Two-Scale Separation

Ions and electrons gyrate around magnetic fields, as discussed in Sec. 1.1.4. The Larmor radius r_L for an ion travelling at the Alfvén speed c_A revolving at a gyrofrequency $\Omega_{ci} = eB/m_i c$ is given by

$$r_L = \frac{c_A}{\Omega_{ci}} = \frac{c}{\omega_{pi}} = d_i \tag{2.10}$$

where $d_i = c/\omega_{pi} = c\sqrt{m_i/4\pi ne^2}$ is the ion inertial length in a quasi-neutral plasma. In antiparallel reconnection at scale lengths shorter than d_i from the X-line, the ions no longer gyrate about a particular magnetic field line. During a gyro-orbit, the ion sees an oppositely directed magnetic field, and reverses its orbit direction, effectively demagnetizing ions in this "ion diffusion region". After averaging over the motion in this region, $\mathbf{v_i} \approx 0$. Additionally, since the Larmor orbit also depends on the square root of the mass of the charged particle, the Larmor radius for electrons, everything else the same, is a factor of ~ 40 smaller than that for ions. In the area between the ion Larmor radius d_i (the ion diffusion layer) and the electron Larmor radius d_e (the electron diffusion layer), the ions are demagnetized while the electrons are still frozen into the magnetic field.

The discussion of *finite Larmor radius (FLR) effects* in the last paragraph can be visualized in Fig. 2.3 from *Drake and Shay* (2007). The reconnecting magnetic fields at the top and bottom are consistent with the out-of-plane current at the center of the reconnection site. The ion and electron flows are shown by the dotted and dashed lines respectively, and

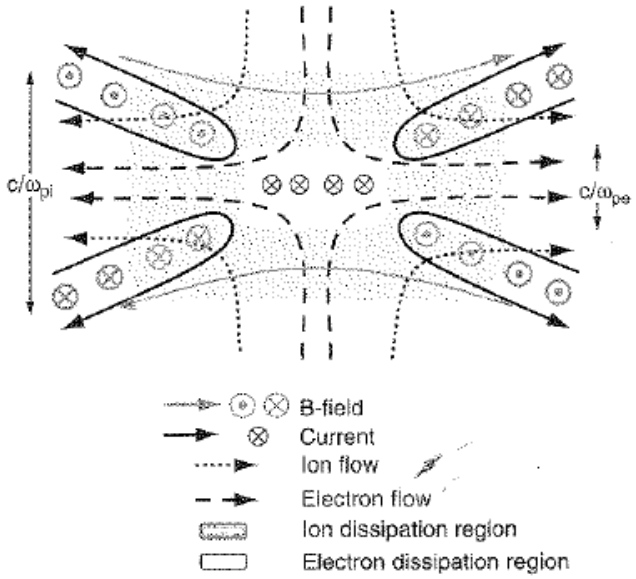

Figure 2.3: Two-scale structure of collisionless reconnection where ions and electrons decouple due to their disparate masses (*Drake and Shay*, 2007). The ion and electron diffusion regions are shown by the shaded and inset clear regions, with flows dotted for ions and dashed for electrons. Due to the disparate scales of the ion and electron diffusion layers, a (Hall) current is driven in the reconnection plane shown by the solid line in the figure, along with the associated quadrupolar out-of-plane magnetic field.

the ion and electron diffusion regions are the centrally nested shaded and clear rectangles with the electron diffusion region inside the ion region. The diagram shows that once the ions enter the ion diffusion region, they are quickly swept downstream in broad outflows scaling with the width of the ion diffusion region. Similarly, the electrons enter the inflow region and travel toward the electron diffusion region before being swept downstream.

A consequence of the ions and electrons decoupling due to their disparate Larmor radii is that while the magnetic field is frozen-in to the bulk plasma outside of the ion dissipation region, inside this region the magnetic field is frozen-in to the electron fluid alone. This yields a current, which should also be included in the model. By adding additional physics to the resistive Ohm's law in Eq. 2.7, these effects can be quantified through a *generalized Ohm's law* and solved self-consistently with the other MHD equations to diagnose reconnection

with collisionless physics.

2.3.2 Generalized Ohm's Law

Two-scale ion and electron physics is included in the *two-fluid* model, a generalization of MHD to include sub-ion Larmor radius effects. To get from the set of resistive-MHD equations in the last section to the two-fluid model, an evolution equation for the electron pressure must be added and Eq. 2.7 is augmented to give

$$\mathbf{E} + \frac{\mathbf{v} \times \mathbf{B}}{c} = \eta \mathbf{J} + \frac{\mathbf{J} \times \mathbf{B}}{nec} - \frac{1}{ne} \nabla \cdot \mathbf{P_e} + \frac{m_e}{e^2} \frac{d}{dt} \left(\frac{\mathbf{J}}{n} \right). \tag{2.11}$$

In addition to the convection and resistive terms, the second term on the right is known as the Hall term including the physics of the disparate ion and electron scales, the third term is the divergence of the electron pressure tensor, and the final term contains the physics of electron inertia.

To understand the physics contained in Eq. 2.11, we begin with the electron fluid equation of motion

$$m_e \frac{d\mathbf{v_e}}{dt} = -\frac{1}{n_e} \nabla \cdot \mathbf{P_e} - e \left(\mathbf{E} + \frac{\mathbf{v_e} \times \mathbf{B}}{c} \right) + m_e \nu_{ei} (\mathbf{v_e} - \mathbf{v_i}). \tag{2.12}$$

Solving this for $\mathbf{E}$ gives Eq. 2.11. From the equation of motion, we approximate $\mathbf{v_e}$ by employing the quasi-neutral approximation mentioned in the last section, $n_i = n_e = n$, along with the definition of electric current to write

$$\mathbf{J} = ne(\mathbf{v_i} - \mathbf{v_e}) \Rightarrow \mathbf{v_e} = \mathbf{v_i} - \frac{\mathbf{J}}{ne} \simeq \mathbf{v} - \frac{\mathbf{J}}{ne}, \tag{2.13}$$

where we also took the limit that $\mathbf{v_i} \simeq \mathbf{v}$ for $m_i \gg m_e$. When substituted into Eq. 2.12,

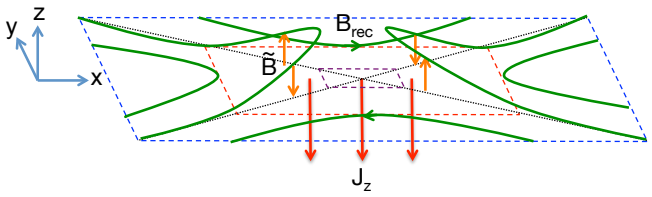

Figure 2.4: Illustration of a reconnection site, where the nested, dashed red and purple boxes indicate the ion and electron diffusion regions, and the opening angle of the X-line is shown in black. The green magnetic fields are convected out of the plane by the electrons making up the reconnection current J_z (red arrows) in the ion diffusion region. This out-of-plane convection leads to a quadrupolar field structure $\tilde{B}$, shown by the orange arrows.

this expression for the electron flow gives rise to the $\mathbf{J} \times \mathbf{B}$ Hall term and the form of the electron inertia term[2] appearing in Eq. 2.11. Physically, as is the case for collisions in the resistive Ohm's law, in the generalized Ohm's law, while electrons attempt to short out any electric fields arising in the plasma, mechanisms arise at the ion and electron gyroscales that limit the electrons ability to negate local charge accumulation, described by the terms on the RHS of Eq. 2.11.

The Hall term describes the ions decoupling from the magnetic field while the electrons remain frozen-in. There is the appearance of a Hall current, as seen in Fig. 2.3 by the solid black arrows. Since the Hall currents are opposite to the electron flow in the ion diffusion layer from the first equality in Eq. 2.13, Hall currents are directed from the outflow to the inflow regions. By Ampère's law, these currents set up an out-of-plane quadrupolar magnetic field along the outflow openings from the X-line consistent with the illustration in Fig. 2.3. This quadrupole structure is also consistent with the out-of-plane electron flow in the ion diffusion layer, illustrated in Fig. 2.4. Since $\mathbf{v_i} \simeq 0$ in the ion dissipation region (the dashed red box), the out-of-plane electron flow is opposite to that of the reconnection current J_z consistent with the (green) magnetic field B_{rec}. The electrons are frozen-in in this region, so

[2]Electron inertia physics only becomes important inside the electron diffusion region where $v_i \simeq 0$, so the fourth term in Eq. 2.11 makes this additional approximation.

they convect the magnetic field out of the reconnection plane (*Terasawa*, 1983; *Mandt et al.*, 1994), producing the quadrupolar out-of-plane field structure $\tilde{B}$ indicated by the orange arrows.

We can find where the Hall term becomes important by applying a scaling analysis similar to that originally done by *Vasyliunas* (1975). By balancing the convection of magnetic field into the ion dissipation region with the Hall term

$$\frac{|\mathbf{v}\times\mathbf{B}|}{c} \sim \frac{|\mathbf{J}\times\mathbf{B}|}{nec} \Rightarrow c_A B \sim \frac{cB^2}{4\pi ne\delta} \Rightarrow \delta_i \sim c_A/\Omega_{ci} \equiv d_i, \tag{2.14}$$

where $B/\delta \sim 4\pi J/c$ from Ampère's law. Thus, we find that the Hall effect becomes important precisely where the ions decouple from the magnetic field in the vicinity of the X-line! Numerical simulations (*Shay et al.*, 1998) and laboratory experiments (*Yamada et al.*, 2006) confirm that the thickness of the ion dissipation region scales like d_i. Additionally, a similar scaling analysis of the electron dissipation layer (*Drake and Shay*, 2007) show its width scales as $\delta_e \sim d_e$, where $d_e = \sqrt{m_e/m_i}d_i$ is the electron inertial length; this is corroborated by simulations (*Zeiler et al.*, 2002).

2.4 Guide-field Reconnection

In the preceding section, we discussed reconnection for an equilibrium magnetic configuration where the fields are antiparallel, lying in a plane without a field component in the direction perpendicular to the reconnection plane. This is a special case of magnetic reconnection; in general, there can be a component of the field perpendicular to the reconnection plane, which is known as a "guide-field". Even with the inclusion of a guide-field, only the components of the magnetic field in the reconnection plane undergo reconnection. An example of this

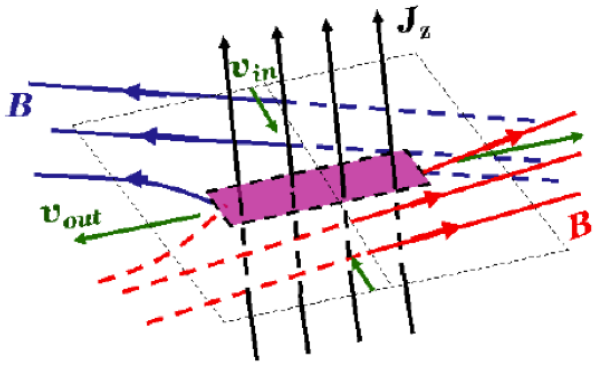

Figure 2.5: Illustration of a reconnection geometry including an additional out-of-plane component of the magnetic field to the reconnecting, antiparallel field (*Cassak*, 2006). The addition of the guide-field leads to a much different structure of the ion and electron dissipation regions in collisionless reconnection.

configuration is illustrated in Fig. 2.5, where the plane of reconnection is defined by black dotted rectangle and the magnetic field is seen to have a component perpendicular to this plane. Reconnection with a guide-field, also known as component reconnection, is the general state of reconnection in many systems including the solar wind, the sunward side of Earth's magnetosphere, and toroidal fusion devices, where the guide field is much larger than the reconnecting field[3].

2.4.1 Pressure Quadrupole

Numerical simulations show that guide-field Hall reconnection is fast[4] when the Hall term is big enough to dominate electron physics (*Kleva et al.*, 1995; *Hesse et al.*, 1999; *Pritchett*, 2001; *Rogers et al.*, 2001; *Hesse et al.*, 2002; *Huba*, 2005), meaning it looks like the top panel in Fig. 2.1, not the bottom panel. Interestingly the inclusion of a sizable guide-

[3]We see in Ch. 3 that the guide-field is estimated to be four orders of magnitude larger than the reconnecting field in the MAST tokamak!

[4]Fast reconnection with a guide-field was also recently reported without the inclusion of Hall effects (*Cassak et al.*, 2015). When an electron pressure anisotropy described by the Chew-Goldberger-Low gyrotropic equations of state is included in the generalized Ohm's law, this effect can dominate the Hall term in plasmas typical of the solar wind and some tokamaks.

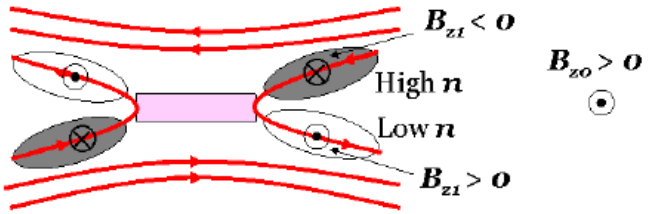

Figure 2.6: Illustration showing the polarity of the density (pressure) quadrupole for the case of collisionless reconnection with a guide-field *Cassak* (2006). Note that the polarity of the density quadrupole is opposite to that of the out-of-plane magnetic field produced by the Hall current, in order to maintain total pressure balance.

field substantially changes the structure of the dissipation regions surrounding the X-line. Physically, this can be understood in terms of pressure balance across the ion dissipation region in the inflow direction. The equation for pressure balance is found from the steady-state ($\partial/\partial t \to 0$) of the momentum evolution equation Eq. 2.3. After using Ampère's law to write $\mathbf{J} \times \mathbf{B} = (c/4\pi)[-\nabla(B^2/2) + (\mathbf{B}\cdot\nabla)\mathbf{B}]$, but neglecting the second term on the RHS since magnetic curvature upstream of the diffusion region is small, we find

$$\nabla\left[p + \frac{B^2}{8\pi}\right] = 0, \tag{2.15}$$

or that the gas pressure plus the magnetic pressure is a constant in space. Recalling the quadrupole magnetic field $\tilde{B}$ in Fig. 2.4, we allow for all quantities to be composed of an equilibrium part and a quadrupole part (perturbation) consistent with two-fluid reconnection, e.g., $p = p_0 + \tilde{p}$. With this substitution, Eq. 2.15 becomes

$$(p_0 + \tilde{p}) + \frac{(\mathbf{B_0} + \tilde{\mathbf{B}})^2}{8\pi} \sim \text{constant} \Rightarrow \tilde{p} \sim \frac{2\mathbf{B_0}\cdot\tilde{\mathbf{B}} + \tilde{B}^2}{8\pi}, \tag{2.16}$$

where the equilibrium terms satisfying $p_0 + B_0^2/8\pi = $ constant have been dropped, since that is the condition which sets the equilibrium. Then we assume that quantities due to

the reconnection quadrupole are small compared to the equilibrium fields, dropping the $\tilde{B}^2$ term. Next, considering that the magnetic field is composed of reconnecting and out-of-plane components $\mathbf{B} = B_{rec}\hat{o} + B_h\hat{h}$, where $\hat{o}$ and $\hat{h}$ are the outflow and out-of-plane directions, for the strong guide-field case where $B_h \gg B_{rec}$, $\mathbf{B_0} \cdot \tilde{\mathbf{B}} = B_{0,rec}\tilde{B}_{rec} + B_{0,g}\tilde{B}_g \sim B_{0,g}\tilde{B}_g$, and Eq. 2.16 reduces to

$$\tilde{p} \sim -B_{g,0}\tilde{B}_g/4\pi. \tag{2.17}$$

Thus, when a guide-field is present, there will be a pressure quadrupole along the reconnection site outflow openings as illustrated in Fig. 2.6 to balance out the guide-field quadrupole due to Hall currents. Additionally, since it is the total pressure that must be balanced, the gas pressure quadrupole has a polarity opposite to that of the magnetic guide-field quadrupole. This depletion and enhancement of the density along the outflow openings has been observed in many simulations (*Kleva et al.*, 1995; *Tanaka*, 1996; *Pritchett and Coroniti*, 2004; *Drake et al.*, 2005).

An alternative way to understand the existence of the pressure gradient for collisionless reconnection with a guide-field is to again consider the physics in Ohm's law, namely how the electrons attempt to short out any charge imbalances. Without a guide-field, electrons in the ion dissipation region attempt to short out the electric field produced by the reconnecting field, which drags the field in the out-of-plane direction. The effect of electron migration on the pressure profile can be seen in the top plot in Fig. 2.7, from *Rogers and Denton* (2003), where the pressure is peaked in center of the outflows. However, when a guide-field is present that is in the same direction as the out-of-plane electric reconnection field, electrons can move across the midplane in the inflow direction to short out this field. This leads to the depleted and augmented regions of the pressure quadrupole seen in the bottom plot of Fig. 2.7.

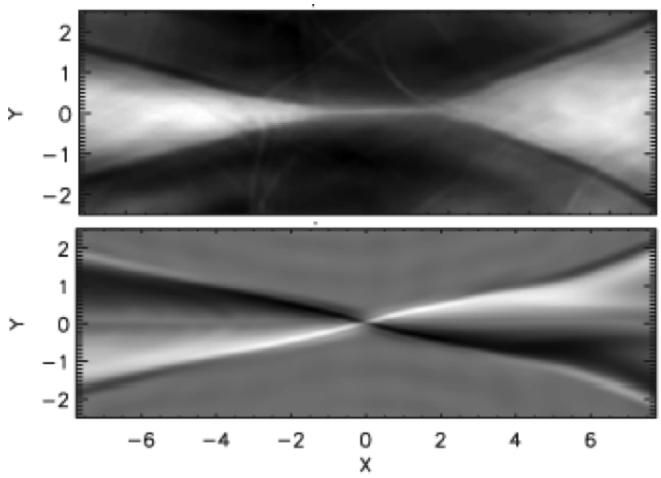

Figure 2.7: Plots of the gas pressure during collisionless two-fluid reconnection for zero guide-field (top) and a guide field 30 times larger than the reconnecting field (bottom) (*Rogers and Denton*, 2003); note that the equilibrium pressure is 30 times greater for the large guide-field case. The pressure is centrally peaked in the outflows in the absence of a guide-field, and exhibits a quadrupole structure for a large guide-field.

2.4.2 Electron Diamagnetic Effects

The scaling argument we used earlier to ascertain the length scale at which the Hall effect becomes important for antiparallel reconnection was valid because there were only two dominant physical processes in question, convection of magnetic fields and the Hall effect. However, compression plays an active role with the introduction of a guide-field, so this simple scaling analysis does not encapsulate the intricate balance between the different physical processes. For guide-field reconnection, the length scale at which the Hall effect becomes important is (*Zakharov and Rogers*, 1992)

$$\delta_i \sim \rho_s, \tag{2.18}$$

where $\rho_s = \sqrt{\beta/2} d_i = c_s/\Omega_{ci}$ is the Larmor radius based on the sound speed $c_s = \sqrt{\gamma_e Z_{eff} k_B T_e/m_i}$, where k_B is Boltzmann's constant, Z_{eff} is the effective ion charge due to impurities and multiple ionization states, and $\beta = 8\pi n k_B T_e/B^2$ is the ratio of the

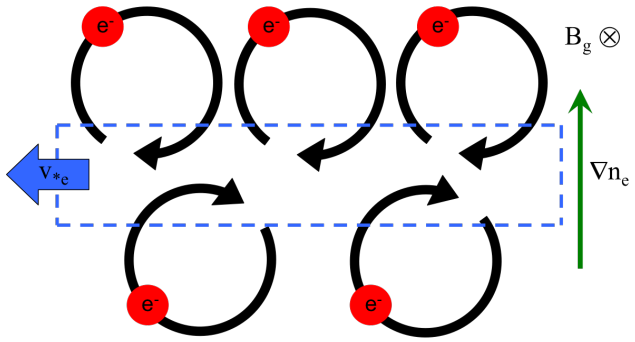

Figure 2.8: Due to density (pressure) gradients on the electron Larmor orbit length-scale when a guide-field is present, the non-uniform concentration of gyro-orbits results in a bulk flow consistent with $\mathbf{v_{*e}} = (c/neB^2)\nabla p_e \times \mathbf{B}$. Note that the electron diamagnetic drift v_{*e} is perpendicular to the direction of the guide-field and the pressure gradient as shown.

electron gas pressure to the magnetic pressure in a plasma. This scaling has been confirmed numerically (*Kleva et al.*, 1995) and observed experimentally (*Egedal et al.*, 2007). Additionally, the guide-field also constrains electrons at smaller scales than was the case for antiparallel reconnection, resulting in a narrower electron dissipation region that scales like $\delta_e \sim \rho_e$ (*Hesse et al.*, 2002, 2004), where $\rho_e = \sqrt{m_e/m_i}\rho_s$ is the electron thermal Larmor radius.

At small length scales inside the ion dissipation layer, the pressure quadrupole that extends along the guide-field reconnection outflow openings converges at the electron dissipation layer, which leads to large electron pressure gradients downstream of the reconnection site. These gradients are important due to diamagnetic effects, as pictured in Fig. 2.8. When pressure gradients (the simplified case of an electron density gradient is shown in Fig. 2.8) arise in a plane perpendicular to a magnetic field, there is a non-uniformity in the concentration of particle gyro-orbits. Due to this non-uniformity, there are an unbalanced number of particles in each half of their orbit locally, which leads to a bulk flow normal to both ∇p_e and $\mathbf{B}$ known as a diamagnetic drift. For a collisionless reconnection site with a guide-field, the pressure quadrupole sets up gradients aligned in the inflow direction as seen in Fig. 2.6,

so the electron diamagnetic drifts are directed along the reconnection outflows.

An alternative way to see the effect of the electron pressure quadrupole in the ion dissipation layer starts with the electron equation of motion, Eq. 2.12. We ignore electron inertia and collisions with ions, and assume an isotropic electron pressure ($\nabla \cdot \mathbf{P_e} \rightarrow \nabla p_e$) for simplicity. Taking the cross product of the remaining terms with the magnetic field and rearranging, we find that the electron velocity perpendicular to the magnetic field satisfies

$$\mathbf{v}_{\mathbf{e},\perp} = c\frac{\mathbf{E} \times \mathbf{B}}{B^2} + c\frac{\nabla p_e \times \mathbf{B}}{neB^2}. \tag{2.19}$$

The first term on the RHS is the well known "E cross B drift" [e.g. *Chen* (1974)], and the second term is the electron diamagnetic drift $\mathbf{v}_{*\mathbf{e}}$. While the $E \times B$ drift is consistent with outflows driven by bent magnetic field lines, numerical simulations of collisionless reconnection have shown electron jets that exceed this speed (*Hesse et al.*, 2008). *Hesse et al.* (2008) showed that this excess is due to electron diamagnetic flows.

2.5 Suppression of Reconnection

Up to this point, this chapter has focused on properties of collisionless reconnection in a steady state. While it all pertains to reconnection during the crash phase of a sawtooth, the main problem we set out to answer was why reconnection can stop suddenly and end the crash phase prematurely. In this section, we begin to see how this is possible by motivating how reconnection is suppressed by diamagnetic effects. While models describing the diamagnetic effects on sawteeth, or the so called ω_*-effects to be more thoroughly explored in the next chapter, were popular in the early 1990's, fully nonlinear, non-axisymmetric, two-fluid simulations of tokamaks were not computationally available. Thus, we concern our

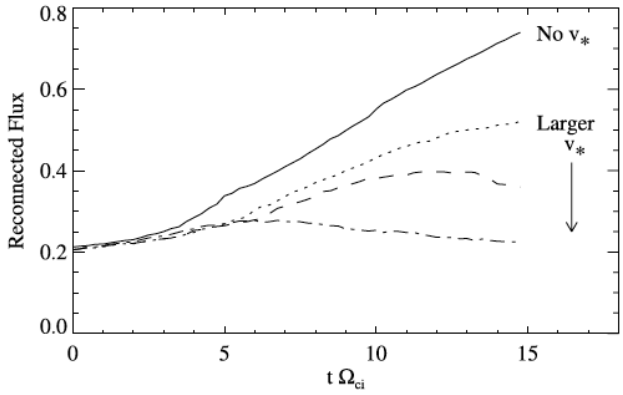

Figure 2.9: Particle-in-cell (PIC) simulations of collisionless guide-field reconnection, where the amount of flux reconnected over time is seen to decrease as diamagnetic effects are increased (*Swisdak et al.*, 2003). The strength of the equilibrium guide-field was varied across the dotted, dashed, and dotted-dashed lines of B_{g0} (1.5, 1.0, and 0) with an equilibrium density gradient across the reconnection inflows. The solid line shows reconnection without any diamagnetic effects for reference.

discussion here to theory and simulations that were initially used to describe reconnection at the sunward side of Earth's magnetosphere (*Swisdak et al.*, 2003), the magnetopause, where there is a large equilibrium density gradient between the outer magnetosphere and the denser plasma of the solar wind. This study has the benefit of using simulations run with a particle-in-cell (PIC) code, which more accurately captures the physics compared to a fluid model.

The initial equilibrium in *Swisdak et al.* (2003) had a gradient in the density across the inflow regions, and with the reconnecting field symmetric, the nonzero guide-field also varied along the inflow direction to maintain total pressure balance. The simulation is initialized with a coherent perturbation of the magnetic flux that sets the X-line, and is large enough that the system begins to reconnect nonlinearly, thereby skipping the tearing phase. By varying the strength of guide-field, while keeping everything else constant, $\mathbf{v_{*e}} = (c/neB^2)\nabla p_e \times \mathbf{B}$ was varied, and numerical results of the amount of magnetic flux reconnected as a function of time are shown in Fig. 2.9. The solid line shows the reference case with no density gradient,

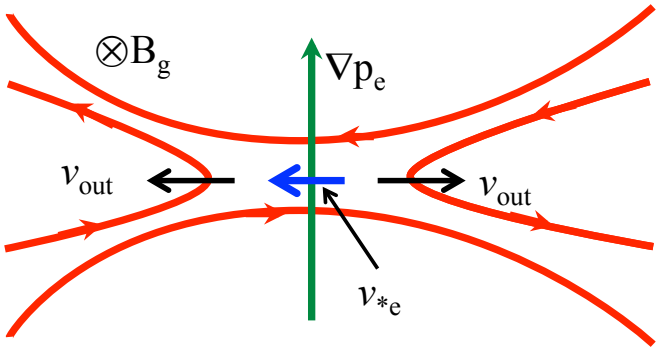

Figure 2.10: For guide-field reconnection with an electron pressure gradient in the inflow direction, there will be an electron diamagnetic flow at the X-line, which causes the X-line to convect in the outflow direction. If the drifting X-line overtakes the reconnection outflow speed, bent field lines can no longer release their tension, and reconnection ceases.

while the dotted, dashed, and dotted-dashed lines have a decreasing value of the guide-field of 1.5, 1.0, and 0. As the guide-field is decreased, the diamagnetic flows are increased, and the amount of reconnected flux decreases as well, a clear indication that diamagnetic effects suppress reconnection.

An imporant aspect of electron diamagnetic flows is that they convect the local magnetic fields (*Coppi*, 1965; *Scott and Hassam*, 1987; *Swisdak et al.*, 2003; *Pritchett*, 2008), as a short derivation shows. Starting from the electron equation of motion, Eq. 2.12, and ignoring electron inertia and resistivity for simplicity gives

$$\mathbf{E} = -\frac{\mathbf{v_e} \times \mathbf{B}}{c} - \frac{\nabla p_e}{n_e e} = -\frac{(\mathbf{v_e} + \mathbf{v_{*e}}) \times \mathbf{B}}{c}. \tag{2.20}$$

Substituting this into Faraday's law, Eq. 2.5, gives

$$\frac{\partial \mathbf{B}}{\partial t} = \nabla \times [(\mathbf{v_e} + \mathbf{v_{*e}}) \times \mathbf{B}]. \tag{2.21}$$

This is analagous to the standard frozen-in condition, where the single fluid velocity $\mathbf{v}$ is replaced by $\mathbf{v_e} + \mathbf{v_{*e}}$. Since magnetic fields convect at velocity $\mathbf{v}$ in ideal-MHD, this implies

that the fields convect with electron flow including the electron diamagnetic drift. Thus, within the ion dissipation region where $\mathbf{v_i} \approx 0$, the electron diamagnetic flows convect the X-line.

Swisdak et al. (2003) finds that when the condition[5]

$$|\mathbf{v}_{*\mathbf{e}}|_{out} \geq v_{out} \tag{2.22}$$

is satisfied, or when the electron diamagnetic flow in the outflow direction at the X-line is greater than the outflows driven by reconnection, reconnection is suppressed. This interplay is illustrated in Fig. 2.10, where an electron pressure gradient across the reconnection layer induces a diamagnetic flow v_{*e} in the same direction as one of the reconnection outflows when a guide-field is present. Physically, if the X-line, convecting with v_{*e}, drifts faster than the reconnection outflow v_{out}, the bent magnetic field lines are no longer releasing their tension in the reference frame of the moving X-line. With no outflow in one of the exhausts, the inflow is throttled and reconnection ceases.

In *Swisdak et al.* (2010), Eq. 2.22 was written in terms of the shear angle θ between the magnetic fields (where $\theta = 180°$ is antiparallel and $0°$ is parallel) as

$$\Delta\beta \geq \frac{2L}{d_i} \tan\left(\frac{\theta}{2}\right), \tag{2.23}$$

where the width of the pressure gradient L corresponds to the gradient length scale, and $\Delta\beta$ is the jump in plasma beta across the reconnection layer. The condition distills the essential physics of reconnection suppression: when pressure gradients ($\Delta\beta$) dominate over magnetic

[5]For completeness, we note that the result in *Swisdak et al.* (2003) used the relative diamagnetic speed between ions and electrons. However, given the discussion in the previous paragraph, we expect that the electron diamagnetic flow is the important physics for suppression.

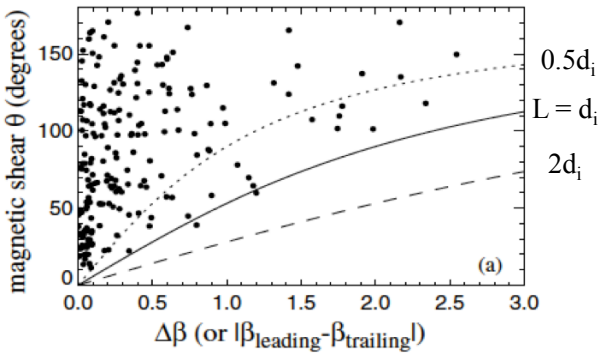

Figure 2.11: Reconnection events in the solar wind as measured by the Wind and ACE spacecraft plotted according to Eq. 2.23 adapted from *Phan et al.* (2010). Only where there is a sufficient amount of magnetic shear in the magnetic field, denoted by the angle θ, compared to the jump in diamagnetic effects across the reconnection layer, quantified by $\Delta\beta$, is reconnection observed. The gradient length scale over which β changes is modeled as the free parameter L, and for $L = d_i$ the data fits above the solid line consistent with Eq. 2.23.

shear (θ), magnetic reconnection ceases. This threshold was tested numerically and verified using solar wind data from reconnection events observed by the *Wind* and *ACE* spacecrafts in the period from 1997 to 2005 (*Phan et al.*, 2010). These data are shown in Fig. 2.11, where the drawn lines correspond to different values modelled for d_i, and each point represents a reconnection event. The distribution of reconnection events confirms that reconnection does not happen when diamagnetic effects are sufficiently large. Additionally, the data suggests that the critical pressure gradient length scale L is equal to the ion inertial scale d_i, since the majority of the reconnection events lie above the solid line in Fig. 2.11. The condition in Eq. 2.23 has also been verified using data from the dayside of Earth's magnetopause, Mercury, Saturn, and the heliopause.

Now that we have motivated the important mechanisms comprising collisionless, guide-field reconnection, and how it can be suppressed due to local pressure gradients at the reconnection site, we are prepared to discuss the problem of reconnection during the sawtooth crash phase in tokamaks. The next chapter will apply knowledge of reconnection to the magnetic configurations of tokamaks, where the magnetic shear and pressure gradients vary

throughout. This will ultimately lead us to a model for incomplete reconnection in sawteeth.

Chapter 3

Incomplete Magnetic Reconnection

3.1 Previous Models of Incomplete Reconnection

There are a number of existing models to explain incomplete reconnection in sawteeth. Many of these models incorporate observations from experiments and simulations of the suppression of sawteeth. However, it is not clear in many cases how the suppression mechanism self-consistently grows and dominates over the tearing/reconnection process.

In *Lichtenberg et al.* (1992), magnetic islands with different pitch, having different N, M characteristic winding numbers consistent with $q = N/M$ from Sec. 1.1.5, overlap, leading to stochastic magnetic fields (*Zaslavskiĭ and Chirikov*, 1972), which was purported to enhance transport and slow reconnection. Modelling by *Igochine et al.* (2007) confirms that stochasticity of overlapping rational surfaces is an important component of the sawtooth crash phase as seen in Fig. 3.1. In each column (a)-(c), numerical data from an equilibrium having a q profile shown in the bottom plot was evolved assuming perturbations having a combination of $(m, n) = (1, 1), (2, 2)$, and $(3, 3)$ helical modes. For the equilibrium with a central safety factor well below 1 shown in (a), many rational surfaces are available to overlap resulting in

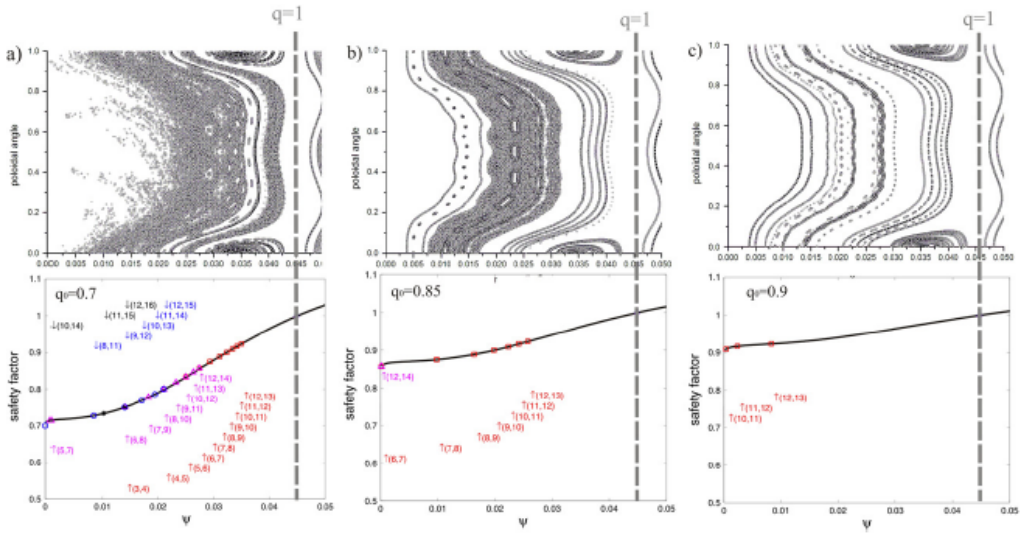

Figure 3.1: (Top) Poincaré plots of the magnetic field for the combination of $(m, n) = (1, 1), (2, 2), (3, 3)$ modes for different safety factor profiles from *Igochine et al.* (2007). (Bottom) q profiles for three equilibria with different central q values. Lower central safety factors include more rational surfaces, leading to increased levels of stochastization.

widespread stochasticity, revealed by space-filling fields in the Poincaré plot in the top row. When $q_0 \lesssim 1$ in (c), the magnetic surfaces are better maintained. While it is accepted that fields become stochastic [e.g. *Borgogno et al.* (2005)], their role was questioned (*Wesson et al.*, 1997) because the transport is caused by motion along the magnetic field, which takes longer than the observed crash times.

It has been directly observed that trapped[1], high energy ion populations prevent sawteeth (*Coppi et al.*, 1988; *White et al.*, 1989, 1990; *Porcelli*, 1991). Whether these energetic populations originate from neutral beams, acceleration by RF sources, or alpha particles produced by the fusion process, they extend the time between sawteeth. The internal kink

[1]Trapped compared to passing particles in a tokamak are due to the $1/R$ varying toroidal magnetic field and the adiabatically conserved magnetic moment of charged particles arising from their Larmor motion. The magnetic moment is given by the ratio of the perpendicular (to the field) kinetic energy of the particle to the local magnetic field strength. As a particle moves along a magnetic field line from the outboard side towards the inboard side of the tokamak, where the local magnetic field increases, in order to keep the particle's total kinetic energy and magnetic moment constant, the particle's parallel kinetic energy (along the field) decreases. Depending on their initial parallel kinetic energy, trapped particles have their parallel velocity decreased to zero, trapping them on the outboard side, while passing particles are able complete a transit around the tokamak.

mode is unstable for $q_0 < 1$, and this mode shifts the plasma column and compresses nearby magnetic surfaces. This causes the gyro-orbits of trapped energetic ions bound to these surfaces to fight against the compression to maintain the radius of their orbits, which has a stabilizing effect on the kink mode. While this gives a mechanism by which sawteeth are prevented, for incomplete reconnection to occur in sawteeth, a sufficient population of trapped energetic particles would need to be produced during the reconnection phase to stabilize the mode prematurely.

A flattening of the safety factor at the rational surface has also led to the suppression of sawteeth (*Holmes et al.*, 1989). As the tearing and reconnection mode grows, a current sheet forms that affects the magnetic field profile and the local shear available to drive the mode. By using non-inductive current drive techniques discussed in Sec. 1.1.4.1 to locally couple energy into ion or electron populations through cyclotron resonance, the local current and associated magnetic shear profiles can be altered to change the sawtooth period by controlling when reconnection of the crash phase is triggered (*Chapman*, 2011a; *Chapman et al.*, 2012, 2013).

There is also evidence that sheared poloidal (*Kleva*, 1992) or toroidal (*Kleva and Guzdar*, 2002) flows stabilize tearing. For poloidal flow shear, the internal kink mode is found to be stabilized when the local gradient in the poloidal flow eclipses the local gradient in the Alfvén speed based off the poloidal magnetic field at the $q = 1$ rational surface. This is suggested by simulation data shown in Fig. 3.2, where the width of the magnetic island resulting from reconnection decreased after the mode migrated to a region of increased poloidal shear. The fundamental physics of this observation was quantified in *Cassak* (2011), where reconnection was stabilized by flow shear on the order of the reconnection outflow that scales with the Alfvén speed. For toroidal flow shear, sawteeth are stabilized when the toroidal flow is on

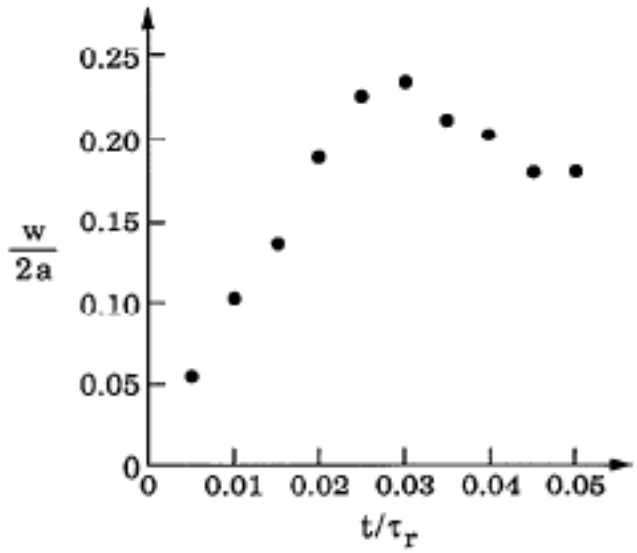

Figure 3.2: Figure 7 of *Kleva* (1992) showing initial growth in the simulated island width, which changes to island reduction as the rational surface migrates to a region of increased poloidal flow shear.

the order of the sound speed. This is because the centrifugal force arising due to toroidal curvature leads to compression, which is stabilizing.

The last models we summarize involve fast reconnection leading to configurations that are out of force balance. In the first, fast reconnection simulations including electron inertia and parallel electron pressure gradient lead to rapid island growth that broadens the current sheet, which weakens its ability to sustain pressure gradients, and begins the dissolution of the reconnection mode (*Wang and Bhattacharjee*, 1995). In another model, it is shown that when the pressure in the island formed by reconnection is larger than the pressure in the core, the nonlinear growth of the $m = 1$ mode is stabilized, stopping reconnection (*Park et al.*, 1987). Determining which, if any, of these models explain incomplete reconnection remains an open question.

3.2 Diamagnetic Suppression and Sawteeth

Diamagnetic effects were first seen to quasi-linearly stabilize the $m = 1$ mode at small island amplitudes for a tokamak-like geometry in *Biskamp* (1981). While these simulations used a simplified cylindrical geometry with helical perturbations, extended-MHD two-fluid terms were kept in the model equations, including electron diamagnetic drift physics. With this reduced set of equations, there was nonlinear evolution of a localized flow the order of the electron diamagnetic velocity v_{*e} around the $q = 1$ rational surface. *Zakharov et al.* (1993, 1994) expanded on this quasi-linear analysis to quantify the diamagnetic stabilization condition as

$$r_1 q'_{cr} > r_1 q'_1, \tag{3.1}$$

where $r_1 = r(q = 1)$ is the minor radius at the $q = 1$ surface, $q'_1 = dq(r)/dr|_{r_1}$, and

$$r_1 q'_{cr} \simeq 1.4\,(m_i/2m_p Z_{eff})^{1/6}\,\beta^{2/3} |n'_e R/n_e|^{2/3} |p'_e R/p_e|^{1/3} \tag{3.2}$$

is evaluated at r_1, where m_p is the proton mass. Sawteeth are suppressed when Eq. 3.1 is met. From this relation, the local electron density/pressure gradients are the main stabilizing forces on the $m = 1$ mode. When this condition was tested against data from the Tokamak Fusion Test Reactor (TFTR) in *Levinton et al.* (1994), good agreement was found as can be seen in Fig. 3.3. In this plot, data from separate discharges on TFTR are displayed according to Eq. 3.1; sawteeth did not occur (black points) when the threshold relation was met, and sawteeth occurred (white points) otherwise, with few exceptions. This agreed with previous numerical results on the diamagnetic stabilization of linear $m = 1$ internal kink modes (*Basu and Coppi*, 1981; *Pegoraro et al.*, 1989).

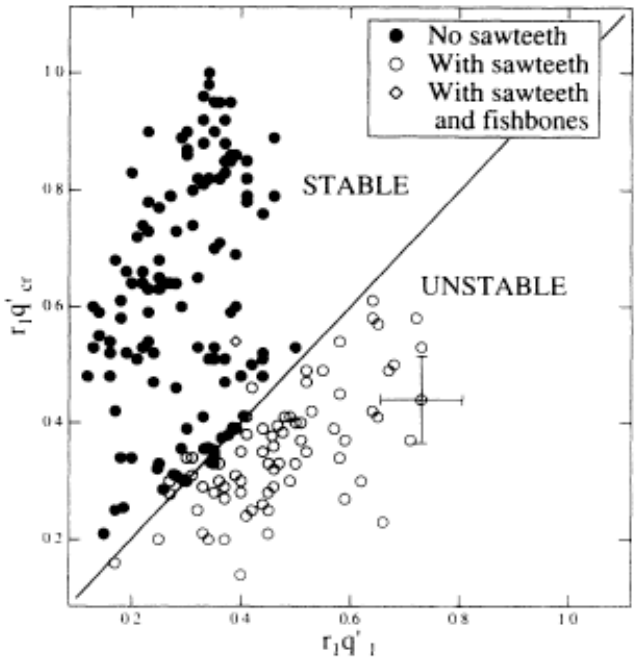

Figure 3.3: Figure 3 from *Levinton et al.* (1994) showing a correlation of sawtooth data from TFTR to the quasi-linear sawtooth suppression condition Eq. 3.1 derived in *Zakharov et al.* (1994). Sawteeth are stable for sufficiently high values of diamagnetic effects.

However, the quasi-linear diamagnetic stabilization condition discussed in *Zakharov et al.* (1994) and *Levinton et al.* (1994) failed to account for sawtooth-free periods in higher β discharges in TFTR. In *Rogers and Zakharov* (1995), nonlinear, two-fluid simulations in a simplified toroidal geometry were performed that showed the $m = 1$ reconnection mode was stabilized early in the nonlinear phase of the evolution for sufficiently large values of the ion and electron diamagnetic frequencies

$$\omega_{*i,e} = - \left. \frac{cp'_{i,e}}{nq_{i,e}Br} \right|_{r_1} \tag{3.3}$$

compared to the growth rate of the ideal $m = 1$ kink mode. *Rogers and Zakharov* (1995) found that the early nonlinear evolution of the reconnection mode works to weaken the ideal MHD drive of the kink mode, and also enhance the effective values of $\omega_{*i,e}$. While this

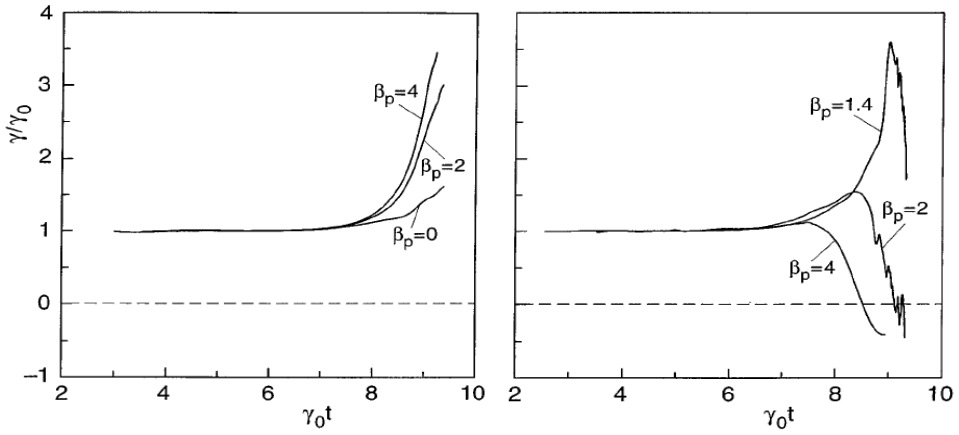

Figure 3.4: Figure 1 adapted from *Biskamp and Sato* (1997) showing normalized growth rates as a function of normalized time for different values of poloidal beta β_p for a density gradient length scale $r_n = n/n'$ (a) $r_n = 10$ and (b) $r_n = 0.7$. While all simulations exhibit a nonlinear acceleration of the growth rate of the mode, only for larger density gradients with $r_n = 0.7$ do the modes abruptly slow their growth, and even change to negative growth.

model was effective in describing the suppression of sawteeth, there was no discussion about whether the nonlinear evolution could lead to incomplete reconnection in sawteeth.

Where *Rogers and Zakharov* (1995) discusses the importance of ω_* effects for the suppression of sawteeth in the early nonlinear phase of reconnection, *Biskamp and Sato* (1997) discusses the importance of ω_* effects during the late nonlinear phase to explain incomplete reconnection. In Fig. 3.4, the evolution of the kinetic energy growth rates of a series of simulations employing reduced two-fluid equations are shown, which cover the parameter space of beta based on the poloidal magnetic field β_p and the length scale of the density gradient $r_n = n/n'$, where (a) $r_n = 10$ and (b) $r_n = 0.7$ in dimensionless units based on the minor radius at the $q = 1$ surface. The growth rates are normalized to the linear growth rate of each simulation, and while each displays an acceleration in the late nonlinear phase, only for the simulations with $r_n = 0.7$ does the normalized growth rate rapidly transition to a phase of deceleration and even negative growth for several simulations.

Thus for larger density gradients, the late nonlinear dynamics are dominated by diamag-

netic drift physics as compared to magnetic reconnection physics. From the series of runs performed they stated a semi-quantitative condition for suppressing reconnection

$$\omega_* > \gamma_{max}, \tag{3.4}$$

where ω_* is either diamagnetic frequency given by Eq. 3.3 and γ_{max} is the maximum nonlinear growth rate. However, they stress that this is not a particularly useful criterion since the nonlinear enhancement of γ is only known "a posteriori". An additional interesting feature of the simulations where reconnection was suppressed is the appearance of turbulence in the reconnection outflows, caused by the Kelvin-Helmholtz instability due to the strong collimated flow from the reconnection region.

3.3 New Model of Incomplete Reconnection

In this section, we propose a model for incomplete reconnection in sawteeth due to the self-consistent dynamics of magnetic reconnection, building on established properties of diamagnetic effects (*Rogers and Zakharov*, 1995; *Biskamp and Sato*, 1997; *Swisdak et al.*, 2003). To understand incomplete reconnection, we first examine why reconnection is complete in Kadomtsev's model.

Begin by observing the $(m, n) = (1, 1)$ reconnection plane sketched in Fig. 3.5. The reversed magnetic field B_* is in red, the high pressure core is in grey, and the reconnection site is the black X. When reconnection begins, outflow jets (in blue) are driven by tension in newly reconnected field lines. Mass continuity induces plasma inflow from upstream (also in blue). This flow convects more magnetic flux (if available) towards the reconnection site, which reconnects. Thus, reconnection is self-sustaining.

We argue that the key to explaining incomplete reconnection is the effect of reconnection dynamics on the pressure gradient at the reconnection site. Suppose the core is initially centered at the yellow X. The pressure gradient at the reconnection site (the green arrow) is radially inward and relatively weak. As the reconnection inflow self-consistently convects the core outward, the pressure gradient at the reconnection site increases. The outward motion of the core has long been seen in observations [e.g. *Yamada et al.* (1994)].

In the presence of a strong out-of-plane (guide) magnetic field B_h, in-plane pressure gradients lead to in-plane diamagnetic drifts, sketched in Fig. 3.5. Recalling Fig. 2.10, diamagnetic drifts $\mathbf{v_{*i,e}}$ are perpendicular to the local magnetic field and pressure gradient, so they are parallel to the reconnection outflows for pressure gradients across the reconnection site in the inflow direction as seen in Fig. 3.5. Recalling Eq. 2.22, it was argued (*Swisdak et al.*, 2003) that reconnection does not occur if

$$|\mathbf{v_{*e}}|_{out} > v_{out}, \tag{3.5}$$

where v_{out} is the reconnection outflow speed, $\mathbf{v}_{*e} = \nabla p_e \times \mathbf{B}/(en_eB^2)$ is the electron diamagnetic drift velocity measured at the reconnection site, and the "out" subscript refers to the outflow direction.

We propose that the increase in v_{*e} as the pressure gradient self-consistently increases due to reconnection causes the left-hand side of Eq. 3.5 to increase. If Eq. 3.5 is never satisfied, reconnection is complete, but if the pressure gradient becomes large enough, reconnection ceases. Since Eq. 3.5 can be satisfied even when free magnetic energy remains, this provides a possible mechanism for incomplete reconnection. This model departs from previous ones (*Biskamp*, 1981; *Biskamp and Sato*, 1997; *Park et al.*, 1987) as it concerns the evolution of

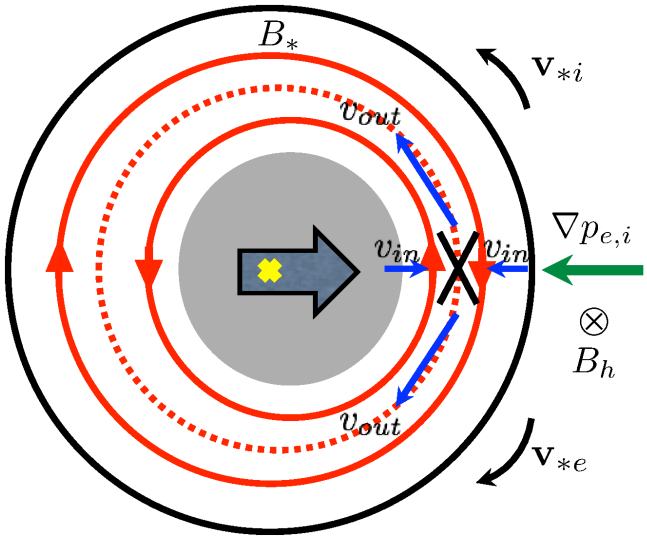

Figure 3.5: Sketch of the $(m, n) = (1, 1)$ reconnection plane. Reconnecting magnetic fields B_* are in red with the rational surface r_s indicated by the dotted red line. Plasma inflows v_{in} and outflows v_{out} are in blue with the reconnection site at the black X. The grey core moves from its initial position centered at the yellow X. The pressure gradient is the green arrow. The helical guide field B_h and the diamagnetic drift velocities $\mathbf{v}_{*i}$ and $\mathbf{v}_{*e}$ are shown.

pressure gradients local to the reconnection site rather than those set by the equilibrium or at the magnetic islands.

3.3.1 Self-Consistent Electron Pressure Gradient Increase

While *Rogers and Zakharov* (1995) and *Biskamp and Sato* (1997) both emphasized the importance of the pressure (density) gradients, and *Rogers and Zakharov* (1995) even observed that the reconnection mode nonlinearly increased the diamagnetic frequencies $\omega_{*i,e}$, there was no explanation of how reconnection brings this about. In Fig. 3.6 we qualitatively show how reconnection self-consistently increases gradients locally at the reconnection site. The horizontal direction is the inflow direction. The red bar shows the electron layer width, which is set by the electron inertial length d_e for antiparallel reconnection and the electron Larmor radius ρ_e for component reconnection (*Horiuchi and Sato*, 1997). These lengths are seen to be approximately constant throughout the reconnection phase, effectively setting the

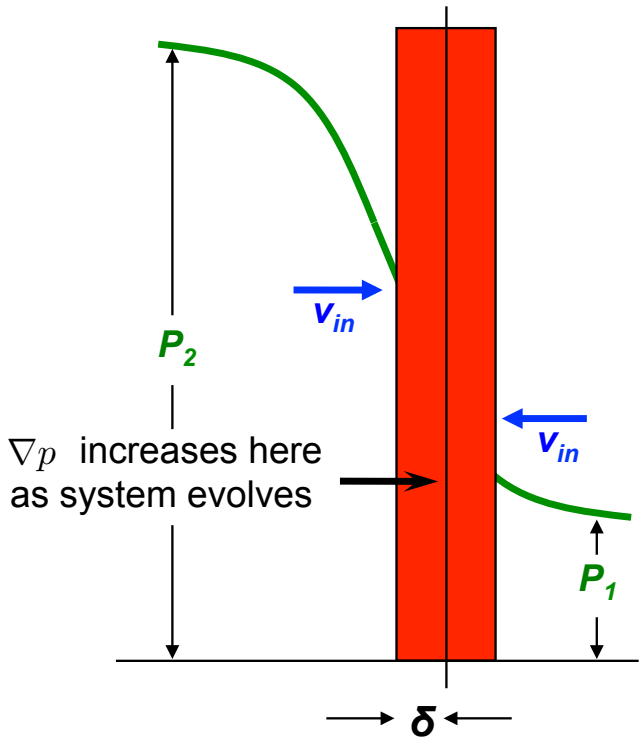

Figure 3.6: The electron pressure gradient increases self-consistently at the X-line due to the reconnection inflows. Since the electrons do not decouple from the magnetic field until electron Larmor scales δ, this length scale is set by reconnection, and additional hot (dense) and cold (less dense) plasma, P_2 and P_1 respectively, brought into the X-line increases the local pressure gradient.

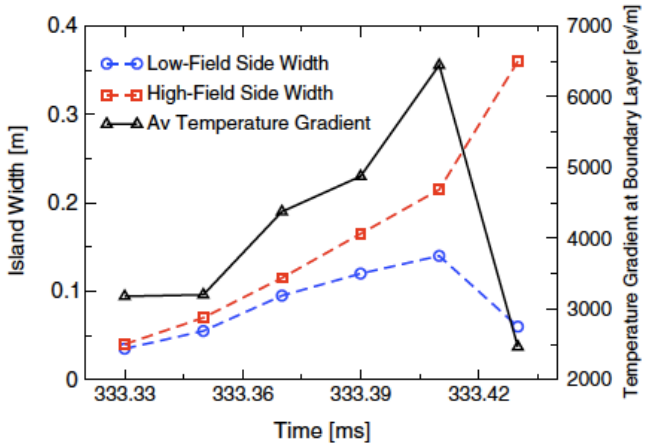

Figure 3.7: Evolution of the electron temperature gradient (black), and the island widths on the low and high field side (blue and red, respectively) for the experimental data presented in *Chapman et al.* (2010).

gradient length scale [r_n in *Biskamp and Sato* (1997)]. As reconnection proceeds, plasma is convected towards the X-line from the hot core and cold edge, increasing the pressure difference on either side of the electron layer, and accordingly the electron pressure gradient.

3.3.2 Qualitative Consistency with MAST

This model complements, and may explain key global features of, recent observations at MAST (*Chapman et al.*, 2010). They observe that $|\nabla T_e|$ increases during a sawtooth period, peaking at the end of the crash as seen in Fig. 3.7, qualitatively consistent with the model. They also show that secondary ideal-MHD instabilities are destabilized at the end of the crash cycle. Reconnection would also play an important role in this process. When reconnection ceases, the electron-scale current sheet broadens, reducing the magnetic shear in a region where $|\nabla p|$ is large. Decreased shear is known to destabilize interchange instabilities between regions with disparate pressures [e.g. *Freidberg* (1987)].

3.4 Two-fluid Simulations in a 2D Slab Geometry

3.4.1 The F3D Code

To test the model for incomplete reconnection given in the previous section, here we explore proof-of-principle numerical simulations. They are performed using the two-fluid code F3D (*Shay et al.*, 2004), which evolves the following set of model equations:

$$\frac{\partial n}{\partial t} = -\nabla \cdot \mathbf{J_i}, \tag{3.6}$$

$$\frac{\partial \mathbf{J_i}}{\partial t} = -\nabla \cdot (\mathbf{J_i J_i}/n) + \mathbf{J} \times \mathbf{B} - \frac{1}{n}\nabla p_e, \tag{3.7}$$

$$\frac{\partial p_e}{\partial t} = -\mathbf{u_e} \cdot \nabla p_e - \gamma_e p_e \nabla \cdot \mathbf{u_e}, \tag{3.8}$$

$$\frac{\partial \mathbf{B}'}{\partial t} = -\nabla \times \mathbf{E}', \tag{3.9}$$

$$\mathbf{E}' = \frac{\mathbf{J}}{n} \times \mathbf{B}' - \frac{\mathbf{J_i}}{n} \times \mathbf{B} - \frac{1}{n}\nabla p_e, \tag{3.10}$$

$$\mathbf{B}' = \left(1 - d_e^2 \nabla^2\right) \mathbf{B}, \tag{3.11}$$

$$\mathbf{J} = \nabla \times \mathbf{B}, \tag{3.12}$$

where the ion current is given by $\mathbf{J_i} = n\mathbf{u_i}$ and the ratio of electron specific heats is $\gamma_e = 5/3$. The first two equations evolve the density and the momentum in the system, which are the same as the MHD Eqs. 2.2 and 2.3, except Eq. 3.7 assumes ions are cold. Electron pressure is evolved assuming an adiabatic ideal gas, analogous to Eq. 2.4. Since ions are assumed cold, there is no evolution equation for the ion pressure; this is compatible with testing the threshold condition Eq. 3.5, where the electron diamagnetic speed is the key parameter. Primed quantities in Faraday's law [Eq. 3.9] are defined in Eqs. 3.10 and 3.11. This form of Faraday's law is equivalent to Eq. 2.5 with $\mathbf{E}$ given by the generalized Ohm's

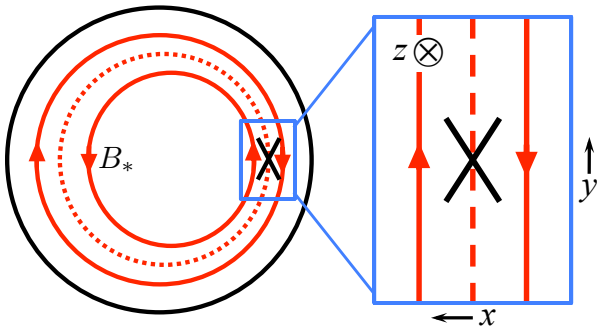

Figure 3.8: Diagram showing one of the reconnection sites simulated in the F3D simulation domain as a local simulation of reconnection at the $q = 1$ rational surface. The reconnecting magnetic field B_* is antiparallel in the x, y (radial, poloidal) plane, with a strong guide-magnetic field in the out-of-plane (helical) $\hat{z}$ direction.

law in Eq. 2.11. The form of Eqs. 3.10 and 3.11 use a technique to fold the electron inertia term into the equations that is expedient for performing numerical simulations. While the condition $\nabla \cdot \mathbf{B} = 0$ is not explicitly enforced by the code, we note that test simulations employing a "cleaner" to enforce the divergence free property of the magnetic field have shown no qualitative difference.

F3D evolves the model equations in time utilizing an explicit, trapezoidal leap-frog numerical method (a predictor-corrector scheme) for approximating temporal derivatives; explicit means that spatial derivatives are evaluated using known data at the timestep being advanced. The spatial representation is a rectangular mesh with a regular grid; a fourth-order finite difference numerical method is used for approximating spatial derivatives. Magnetic fields and densities are normalized to arbitrary values B_0 and n_0, velocities to the Alfvén speed $c_{A0} = B_0/(4\pi m_i n_0)^{1/2}$, lengths to the ion inertial length $d_{i0} = c/\omega_{pi} = (m_i^2 c^2/4\pi n_0 Z_{\rm eff}^2 e^2)^{1/2}$, times to the ion cyclotron time $\Omega_{ci0}^{-1} = (Z_{\rm eff} e B_0/m_i c)^{-1}$, electric fields to $E_0 = c_{A0} B_0/c$, and pressures to $p_0 = B_0^2/4\pi$.

For the proof-of-principle simulations in this chapter, we employ a two-dimensional slab geometry with periodic boundary conditions that feature two reconnection sites being evolved

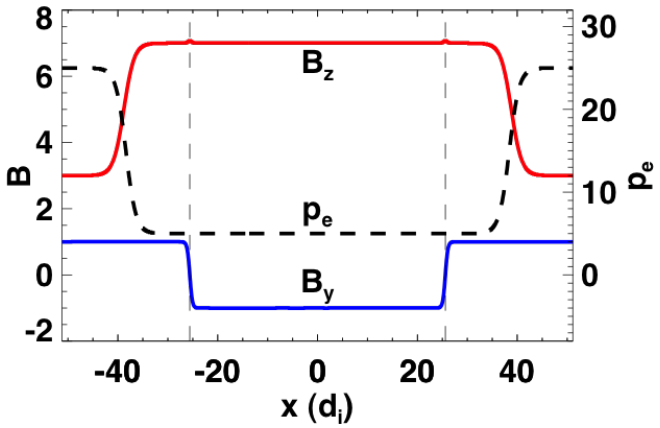

Figure 3.9: Equilibrium profiles of reconnecting magnetic field B_y, magnetic guide-field B_z, and electron pressure p_e. B_y has the form of a double Harris sheet, giving two rational surfaces per simulation. p_e has a gradient upstream from the rational surfaces, which convects inward due to the reconnection inflows. B_z has a profile that ensures total pressure balance and also $B_z^2 \gg B_y^2$ at the reconnection site.

simultaneously. This geometry is appropriate for a proof-of-principle study because motion in the plane normal to the guide magnetic field is well-described in two dimensions. In effect, we are choosing to simulate the region local to the reconnection site of the $q = 1$ rational surface as depicted in Fig. 3.8, where we show a poloidal plane with the reconnection site expanded onto a 2D slab geometry. While we save the discussion of the reconnection plane geometry in the toroidal system for the next chapter, here we note that the magnetic field in the reconnection plane has an antiparallel reconnecting field B_* as shown in Fig. 3.8.

3.4.2 Simulation Setup

As shown in Fig. 3.8, the simulation coordinate system has x parallel to the inflow (radial), y parallel to the outflow (poloidal), and z in the out-of-plane (helical) direction, invariant in the present two-dimensional simulations. The equilibrium for the principal simulation is

shown in Fig. 3.9, and has an in-plane magnetic field profile of a double Harris sheet,

$$B_y(x) = \tanh\left(\frac{x - L_x/4}{w_0}\right) - \tanh\left(\frac{x + L_x/4}{w_0}\right) + 1, \tag{3.13}$$

where $L_x \times L_y = 102.4 \times 204.8$ is the system size and $w_0 = 0.5$ is the initial thickness of the current sheet. For this equilibrium, the toroidal mode number is $n = 0$ manifestly (not to be confused with the density), so the rational surfaces are at $x_s = \pm L_x/4 = \pm 25.6$. We focus on a single mode because there is typically a dominant mode in sawteeth $[(m, n) = (1, 1)]$; the $n = 0$ mode is chosen for simplicity, but is not expected to alter the conclusions.

The density for the principal simulation is initially $n = 1$. The initial electron pressure profile shown in Fig. 3.9 is given by

$$p_e(x) = \frac{1}{2}(p_1 + p_2) + \frac{1}{2}(p_1 - p_2) \times \left[\tanh\left(\frac{x + 3L_x/8}{w_p}\right) - \tanh\left(\frac{x - 3L_x/8}{w_p}\right) - 1\right]. \tag{3.14}$$

The pressure gradient is localized near $x = \pm 3L_x/8 = \pm 38.4$ rather than at the rational surfaces x_s. Thus, p_e at the reconnection site is initially uniform. The length scale of the pressure gradient is $w_p = 2$. The guide magnetic field $B_z(x)$ has a mean value of 5 with a profile that ensures total pressure balance, $p + B^2/2 = \text{constant}$.

The principal simulation employs $p_1 = 5, p_2 = 25$ so v_{*e} is large enough to exceed v_{out} when the high pressure plasma convects in. Other simulation parameters are carefully chosen: $B_z \gg B_y$ as is relevant to sawteeth and p_e is large enough so the ion Larmor radius $\rho_s = c_s/\Omega_{ci}$ exceeds the electron skin depth $d_e = c/\omega_{pe}$ at the reconnection layer, allowing fast reconnection to proceed (*Aydemir*, 1992; *Rogers et al.*, 2001).

The principal simulation employs a grid scale of $\Delta = 0.05$, where a test simulation with $\Delta = 0.025$ confirms the resolution is sufficient. Equations 3.6-3.9 include fourth-order numerical diffusion with a coefficient $D_4 = 2 \times 10^{-5}$ to damp noise at the grid scale; D_4 has been varied to ensure the key physics is not sensitive to it. The explicit numerical diffusion smoothes out noise at the grid scale, but is not responsible for balancing the out-of-plane reconnection field at the X-line. The electron to ion mass ratio is 1/25. Simulations include no resistivity because experimental crash times are faster than collisional reconnection times, and it has been seen that fast reconnection in a 2D slab geometry is insensitive to the dissipative mechanism breaking magnetic fields at the X-line (*Birn et al.*, 2001). The presented simulations do not employ a parallel thermal conductivity $\chi_\parallel$, but test simulations with $\chi_\parallel = 0.08$ reveal no significant changes. Tearing is initiated by a small coherent perturbation to the in-plane magnetic field of amplitude 0.01. It is known that secondary islands can spontaneously arise in reconnection simulations; due to symmetry, such islands would stay at the original X-line (*Loureiro et al.*, 2005). To prevent this, initial random magnetic perturbations of magnitude 2.0×10^{-5} (different from D_4) break symmetry so secondary islands are ejected.

3.4.3 Cessation of Reconnection

Upon evolving the system, Hall reconnection occurs initially and the high pressure plasma convects towards the reconnection site as expected. The reconnection rate E, measured as the time rate of change of the difference between the magnetic flux between the X-line and O-line, is plotted as the solid (red) line in Fig. 3.10(a). It increases from zero to its expected value near 0.1 (*Shay et al.*, 1999) by $t \sim 90$, where it reaches a steady-state with a single X-line. (The variation between $t = 40$ and 90 is due to transient secondary island formation

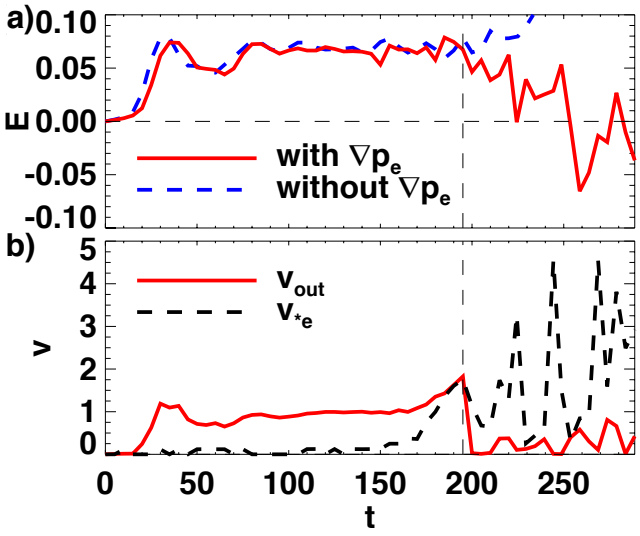

Figure 3.10: (a) Reconnection rate E as a function of time t with and without an upstream pressure gradient. (b) Diamagnetic drift speed v_{*e} at the reconnection site and average outflow speed v_{out} vs. t for the simulation with an upstream pressure gradient that convects into the reconnection site, causing the self-consistent increase in v_{*e}.

and coalescence.) At $t \simeq 195$, E begins decreasing. It decreases to below zero, where it fluctuates for a number of Alfvén crossing times. Thus, reconnection has shut off.

To determine the cause, the electron diamagnetic speed v_{*e} at the reconnection site is plotted as a function of time in Fig. 3.10(b) as the dashed (black) line. For comparison, the average reconnection outflow speed v_{out} is plotted as the solid (red) line. Asymmetric outflows occur when there is a pressure gradient in the outflow direction (*Murphy et al.*, 2010), and since such gradients self-consistently generate here, v_{out} is calculated as the average of the maximum electron outflow speeds from either side of the reconnection site, averaged over $5d_e$ when turbulent. We revisit the asymmetric outflows in the next section.

Figure 3.10(b) reveals that v_{*e} is small initially, but increases in time once the pressure gradient reaches the reconnection site at $t \simeq 140$. It increases until it becomes comparable to v_{out} at $t \simeq 195$ (the vertical dashed line), the same time E begins to decrease. Therefore, reconnection is throttled when Eq. 3.5 is first satisfied.

Table 3.1: Parametric simulations where the equilibrium magnetic guide-field, density, and electron pressure are varied to explore how the system evolution depends on electron diamagnetic effects.

Run	$n_{0.5,5}$	$n_{1,5}$	$n_{2,5}$	$n_{2,5^*}$	$n_{4,5}$	$B_{1,3.75}$	$B_{1,5}$	$B_{1,7.5}$	$B_{1,10}$
$B_{z,0}$	5	5	5	5	5	3.75	5	7.5	10
n_0	0.5	1	2	2	4	1	1	1	1
$p_{e,min}$	5	5	5	20	20	5	20	20	20
$p_{e,max}$	12.5	15	15	30	30	15	40	40	40

To ensure the observed effect is caused by the pressure gradient, simulations with other pressure profiles are performed. When there is no gradient with $p_1 = p_2 = 5$, there is no decrease in E, plotted as the dashed (blue) line in Fig. 3.10(a). The same is true for $p_1 = p_2 = 25$ (not plotted). When $p_1 = 5, p_2 = 7$, no drop in reconnection rate is observed because the maximum v_{*e} only reaches ~ 1, but $v_{out} \sim 2$ so Eq. 3.5 is never satisfied. In summary, the simulations confirm the basic prediction of the model: reconnection ceases when large enough pressure gradients self-consistently convect into the reconnection site despite the presence of free magnetic energy.

3.4.4 Evolution of Reconnection Due to Diamagnetic Effects

From Fig. 3.10, we see that the self-consistent growth of electron diamagnetic effects at the X-line can cause magnetic reconnection to cease; essentially, reconnection shuts itself off. With this proof-of-principle simulation being consistent with the model presented in Sec. 3.3, we next perform a series of parametric simulations to test the dependence of the cessation process on different parameters contributing to electron diamagnetic effects.

3.4.4.1 Parametric Scalings

In order to probe the interaction between diamagnetic and reconnection physics, we perform a series of simulations with various densities and guide-field strengths as given in Table

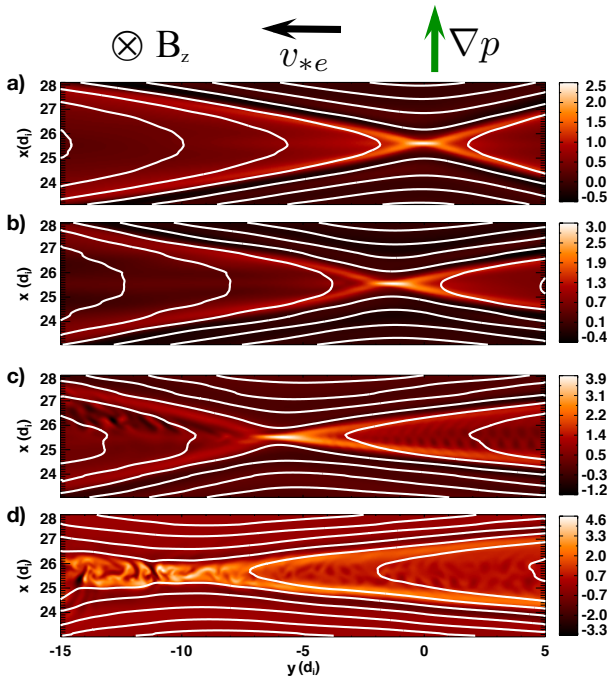

Figure 3.11: Out-of-plane current density J_z zoomed in near the X-line with magnetic field lines superimposed for run $n_{1,5}$ (a) before ($t = 145$) and (b) after ($t = 185$) the pressure gradient reaches the X-line, (c) after the threshold condition is reached ($t = 210$), and (d) after the X-line becomes turbulent ($t = 225$). The x and y axes correspond to the radial and poloidal directions, respectively.

3.1, where runs denoted by $n_{a,b}$ varied the density and $B_{a,b}$ varied the magnetic guide-field, where a, b refers to the value of density and guide-field. The equilibrium parameters for all simulations were chosen to maintain proper ordering to obtain fast tearing/reconnection (*Rogers et al.*, 2001), given by $d_e < \rho_s < d_i$, as discussed earlier. The maximum and minimum pressures setting the external pressure gradient were set to ensure that the diamagnetic drift speed can exceed the outflow speed as the system evolves.

This set of simulations shows that reconnection with an equilibrium upstream pressure gradient has four relatively distinct phases as can be seen in Fig. 3.11, which shows plots of the out-of-plane current density J_z near the X-line for run $n_{1,5}$ with in-plane magnetic field lines superimposed. First in (a), as the system begins to evolve, reconnection proceeds as

normal with the external pressure convecting towards the X-line. Second in (b), the pressure gradient impinges upon and interacts with the X-line. Next in (c), as additional high pressure continues to convect inwards, the diamagnetic effects increase locally at the X-line, and an instability arises in the exhausts. Finally in (d), the instability is seen to grow and the entire region near the X-line becomes turbulent. Viewed across the parametric simulation set, each of the simulations have this general behavior. The timescales associated with the phases (a)-(c) exhibit a linear relationship according to the square root of the density (not shown), consistent with the reconnection inflow scaling with the Alfvén speed. However, we did not find a significant scaling with the guide-field, suggesting that the characteristic timescales were independent of the magnitude of $v_{*e} \sim B_g^{-1}$.

3.4.4.2 X-line Convection

To study diamagnetic effects, we again look at Fig. 3.11. As indicated, the guide field is in the z-direction and ∇p_e is in the x-direction. The reconnection site drifts in the $-y$-direction, the direction of $\mathbf{v}_{*e}$ (*Rogers and Zakharov*, 1995; *Swisdak et al.*, 2003). Note the appearance in panel (c) of secondary instabilities in the exhausts. We suspect the instability in the left exhaust is Kelvin-Helmholtz, and the instability in the right exhaust is a drift instability. The appearance of these instabilities have also been observed in gyrokinetic simulations (*Kobayashi et al.*, 2014). The instabilities result in widespread turbulence through the reconnection site in panel (d). The increased variability of v_{*e} and E after $t \simeq 205$ in Fig. 3.10 are attributed to these instabilities. Additionally, as v_{*e} at the X-line increases from its initial value of zero, the distance the X-line convects increases. From Fig. 3.11(a) to (b), the X-line convects very little, but from (c) to (d) convects much further.

To observe how the reconnection site convects throughout the series of parametric sim-

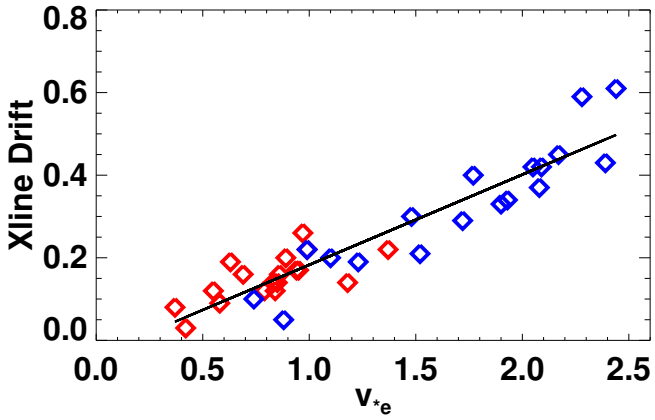

Figure 3.12: Scatter plot of the calculated electron diamagnetic drift v_{*e} and the measured X-line drift at the beginning (red) and end (blue) of the third phase shown in Fig. 3.11(c) for the simulations in Table 3.1.

ulations, Fig. 3.12 shows a scatter plot of the calculated electron diamagnetic drift at the X-line and the measured X-line drift at the beginning (red) and end (blue) of the third reconnection phase in Fig. 3.11(c). As expected, we see a definite correlation between the diamagnetic and X-line drifts. Furthermore, as we commented on at the end of the last paragraph, as the simulation evolves, v_{*e} and the X-line drift both increase (blue is larger in magnitude than red), consistent with the observations in Fig. 3.11.

Interestingly, *Swisdak et al.* (2003) revealed a $1:1$ correspondence between v_{*e} and the X-line drift, while we find a $5:1$ correspondence. However, that study differed in their use of particle-in-cell (PIC) simulations, and their initial pressure gradient was located at the rational surface. A possible future study would use PIC simulations with the equilibrium used for runs included in this chapter.

3.4.4.3 Asymmetric Outflows

As was mentioned in Sec. 3.4.3, the reconnection outflows evolve asymmetrically. This can be seen in Fig. 3.13(a), which plots the maximum downstream electron outflow speeds in the

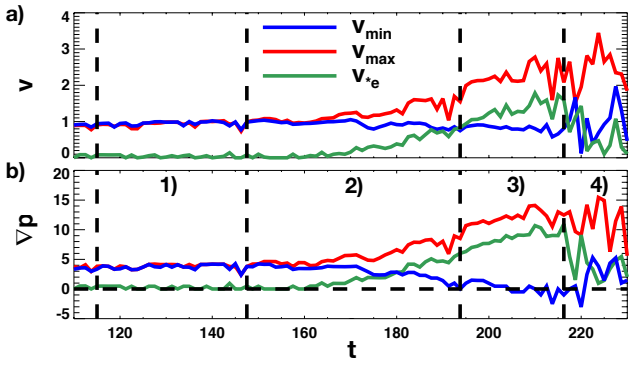

Figure 3.13: Evolution of (a) the maximum downstream electron flow speeds $v_{min,max}$ (blue and red traces) and v_{*e} (green trace) at the reconnection site, and (b) the electron pressure gradient at the location of the maximum v_e (blue corresponding to the outflow with v_{min} and red for the outflow with v_{max}) and the X-line (green). The vertical dashed black lines separate the four phases of reconnection displayed in Fig. 3.11. In phase 1) the outflow speeds and outflow pressure gradients are identical, while in phase 2) when the external pressure gradient impinges on the X-line they diverge while the pressure gradient at the X-line increases along with v_{*e} through phase 3) and 4) where instability leads to turbulence.

two reconnection exhausts denoted as $v_{min,max}$ (blue, red trace) and the electron diamagnetic speed v_{*e} at the reconnection site (green trace). The vertical dashed black lines separate the reconnection phases shown in Fig. 3.11. In phase (1) the external pressure gradient is upstream of the reconnection site, and the outflow velocities are symmetric with $v_{*e} = 0$. In phase (2) the external pressure gradient impinges on the X-line, and as v_{*e} increases from its initial value, the outflows become distinctly asymmetric. During this phase, the X-line also begins to move, contribuing to the outflow asymmetry. In phase (3) as the outflow asymmetry and v_{*e} continue to increase, an instability arises in the exhaust, which throughout the series of parametric simulations is coincident with the time that v_{*e} exceeds the smaller electron outflow speed

$$v_{*e} \geq v_{out,min}. \tag{3.15}$$

The external pressure gradient continues to convect into the reconnection site, exacerbating the asymmetry and feeding the instability until the site becomes turbulent in phase (4).

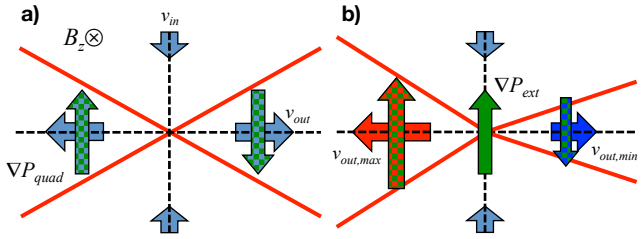

Figure 3.14: Representation of the reconnection outflows and quadrupole pressure gradients (a) before and (b) after the external pressure gradient impinges on the reconnection site. The opening angle of the X-line is shown in red, the reconnection inflows by the small blue arrows and the outflows by the large blue arrows [red and blue for the asymmetry in (b)], the pressure gradient at the X-line by the green arrow, and the quadrupole pressure gradients by the blue(red)/green checkered arrows. Due to the polarity of the outflow pressure gradients, the external pressure gradient asymmetrically affects the outflows, leading to asymmetric outflow speeds. Additionally, the width of the outflows are also observed to be altered asymmetrically by the external pressure gradient as shown.

While the convection of the X-line due to the local electron diamagnetic drift contributes to the development of the asymmetry in the reconnection outflows, the external pressure gradient also affects the reconnection process in another way. Looking at Fig. 3.13(b), the electron pressure gradients at the locations of both maximum downstream electron flows (blue and red traces) and at the X-line (green trace) are plotted. As expected, the pressure gradient at the X-line evolves similarly to v_{*e} (it would be more correct to say that v_{*e} increases with the electron pressure gradient). However, the downstream pressure gradients begin to evolve asymmetrically as the external pressure gradient impinges upon the reconnection site in phase (2), similar to the outflow speeds.

Physically, this observation can be understood by recalling our discussion at the end of Sec. 2.4.2 on electron diamagnetic effects local to the reconnection site. For two-fluid, guide-field reconnection, there is a gas pressure quadrupole needed to maintain total pressure balance with the out-of-plane magnetic field quadrupole consistent with the Hall currents. The pressure quadrupole sets up pressure gradients in outflows of the ion dissipation layer, which, with a guide-field present, are consistent with v_{*e} flows. In Fig. 3.14(a), the recon-

nection site is illustrated prior to the inward convection of the external pressure gradient, where the reconnection flows and outflow pressure gradients are symmetric, similar to that seen in the bottom panel of Fig. 2.7. When the external pressure gradient impinges on the reconnection site, as depicted in Fig. 3.14(b), the polarity of the gas pressure quadrupole is such that the external gradient affects the outflow pressure gradients asymmetrically, leading to asymmetric v_{*e} components of the reconnection outflows.

Together, the motion of the X-line and the asymmetry of the outflows lead to the asymmetry of the opening angle of the X-line as depicted in Fig. 3.14(b) and seen in Fig. 3.11(c). A full analysis of the evolution of the gas pressure quadrupole and its effect on reconnection with asymmetric outflows is saved for a future study.

3.5 Quantitative Comparison with MAST

The simulations shown in the Sec. 3.4 support the efficacy of the new model for incomplete reconnection presented in Sec. 3.3. When the threshold in Eq. 3.5 was satisfied, reconnection stabilized due to the increased presence of electron diamagnetic effect. In this section, we assess the threshold condition with experimental data from MAST (*Chapman et al.*, 2010). MAST is a spherical tokamak located at the Culham Centre for Fusion Energy in the UK. The aspect ratio R/r is near unity, where poloidal field coils are used to create a highly-shaped plasma cross-section. The smaller aspect ratio is beneficial because a similar Lawson criterion to that of conventional tokamaks can be achieved with approximately a tenth of the magnetic field. Interestingly, the increased plasma shaping lowers the instability threshold for the internal kink mode, making spherical tokamaks prime experiments for studying sawteeth.

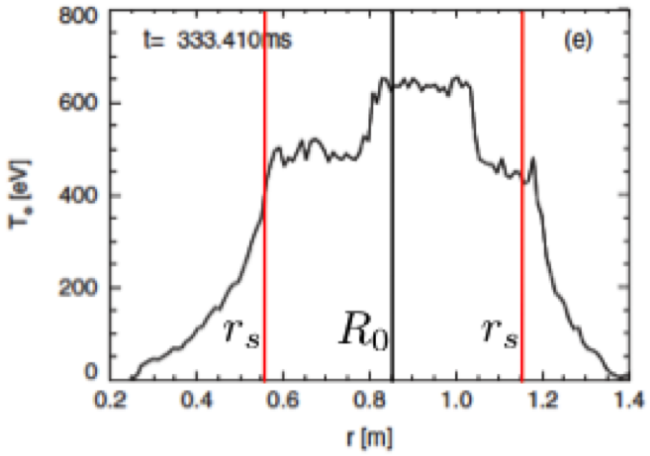

Figure 3.15: Figure 1(e) reproduced from *Chapman et al.* (2010) showing the electron temperature profile towards the end of the reconnection phase of the sawtooth crash. The overlaid vertical lines correspond to the center of the plasma (black) and the calculated $q = 1$ rational surface (red).

3.5.1 Diamagnetic Cessation Threshold

To test the prediction quantitatively, we need to transform into the plane of reconnection perpendicular to the $(m, n) = (1, 1)$ helical direction. The reconnecting field B_* is related by Eq. 1.8 to the toroidal B_ϕ and poloidal B_θ fields as $B_*(r) = B_\theta - (r/R_0)B_\phi$. At MAST, $R_0 = 0.85$ m (*Appel et al.*, 2008) while $B_\phi \simeq 0.4$ T and $B_\theta \simeq 0.15$ T (*Chapman*, 2011b). The minor radial location of the rational surface r_s is where $B_* = 0$ in Eq. 1.8, which gives $r_s \simeq 0.32$ m. This result agrees well with Fig. 1(e) of *Chapman et al.* (2010) towards the end of the reconnection phase of the sawtooth crash, reproduced in Fig. 3.15, which has $r_s = 0.85\text{ m} - 0.56\text{ m} = 0.29$ m. The helical guide field at r_s is $B_h = B_\phi(1 + r_s/R_0) \simeq 0.55$ T.

To test the model, Eq. 3.5 must be evaluated at the end of the sawtooth crash. The outflow speed scales with c_{Ae}, the electron Alfvén speed based on the field B_{*e} upstream of the electron current layer. Assuming the large guide field limit with $B_h \gg B_*$ in the vicinity of r_s, the thickness of the electron current layer scales as the electron Larmor radius $\rho_e = v_{th,e}/\Omega_{ce}$ (*Horiuchi and Sato*, 1997), where $v_{th,e} = (\gamma_e k_B T_e/m_e)^{1/2}$ is the electron

thermal speed and $\Omega_{ce} = eB/m_e c$ is the electron cyclotron frequency. Using $T_e \simeq 500$ eV at r_s (*Chapman et al.*, 2010) and $\gamma_e = 5/3$, we find $\rho_e \simeq 0.013$ cm. To find B_{*e}, we evaluate Eq. 1.8, at $r_s \pm 2\rho_e$ (*Jemella et al.*, 2003), which gives $B_{*e} \simeq 5.9 \times 10^{-5}$ T, justifying the strong guide field assumption. Using this value, with $n_e \simeq 6 \times 10^{19}$ m^{-3} estimated from Fig. 2 in *Chapman et al.* (2010), gives $v_{out} \approx 14.2$ km/s.

To estimate v_{*e}, note $|\nabla p_e|/n_e = |\nabla T_e| + T_e(|\nabla n_e|/n_e)$. The right-hand side is estimated at the end of the crash from Figs. 1(e), 2 and 3 of *Chapman et al.* (2010) to be $|\nabla p_e|/n_e \simeq 7400$ eV/m. Then, the electron diamagnetic speed is $v_{*e} = |\nabla p_e|/(q n_e B_h) \approx$ 13.5 km/s. Thus, the two speeds agree rather well, showing the agreement of the model with the experimental data is also quantitative.

As a further consistency check, we compare the speed of the core to the inflow speed. The the core's speed is estimated from Figs. 1(d-f) of *Chapman et al.* (2010) by dividing its displacement ($\simeq 0.08$ m) by the elapsed time ($\simeq 0.04$ ms), giving a speed of ~ 2 km/s. The reconnection inflow speed scales like $0.1 c_{Ai}$ (*Shay et al.*, 2004), where c_{Ai} is the ion Alfvén speed based on the field B_{*i} upstream of the ion current layer. The ion layer thickness with a large guide field scales like the ion Larmor radius ρ_s (*Zakharov et al.*, 1993). Using $Z_{\text{eff}} \sim 1$ (*Tournianski et al.*, 2005) and $m_i = 2m_p$ for a deuterium plasma (*Appel et al.*, 2008), we find $\rho_s \sim 0.77$ cm. As in the calculation of B_{*e}, we evaluate Eq. 1.8, at $r_s \pm 2\rho_s$, giving $B_{*i} = 6.7 \times 10^{-3}$ T. Then, $c_{Ai} \approx 13$ km/s, so the inflow speed is $\simeq 1.3$ km/s. Thus, the inflow speed is comparable to the speed of the core, as predicted.

3.5.2 Secondary Instabilities

Post-cessation features are important for the subsequent dynamics. Figure 3.11(d) shows J_z significantly after the pressure gradient reaches the reconnection site. The current layer

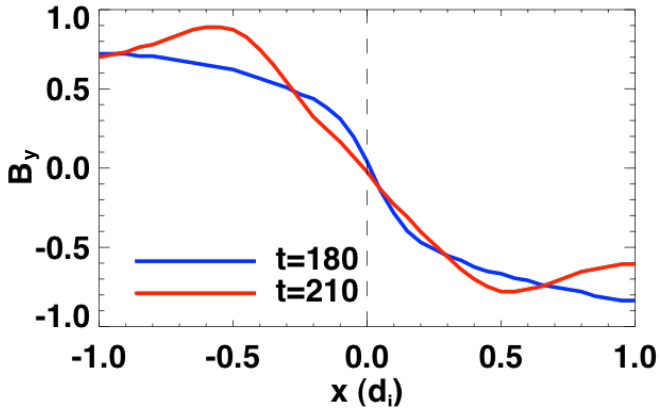

Figure 3.16: Profiles of the reconnecting magnetic field B_y taken through the reconnection site in the inflow direction (a) before and (b) after the reconnection site becomes turbulent in the principal simulation. It is observed that the local magnetic shear significantly decreases due to the turbulence that widens the current sheet.

broadens as reconnection stops, reducing the magnetic shear at the reconnection site. This can also be seen in Fig. 3.16, where profiles of the reconnecting field B_y taken through the reconnection site in the inflow direction are plotted before (blue) and after (red) the reconnection site becomes turbulent for the principal simulation. In addition to the turbulence that broadens the current sheet, when reconnection shuts off, magnetic flux ceases to convect toward the X-line, further decreasing the stabilizing magnetic shear there. The reduced shear would make the system more prone to interchange instabilities [e.g. *Freidberg* (1987)], which were argued to occur in *Chapman et al.* (2010). In tokamaks, it is the curvature of the magnetic fields that supplies the free energy to drive the interchange instability. Unfortunately, the slab geometry simulations here lack that energy source. Thus, while our model appears consistent with experimental observations, toroidal simulations are necessary for a direct comparison.

3.6 Threshold Condition for Toroidal Geometry

For tokamak applications, Eq. 3.5 may be recast in terms of more familiar quantities. First, we assume $v_{out} \sim c_{Ae} = B_{*e}/\sqrt{4\pi m_e n_e}$ is the speed of the reconnection exhaust. Next, we rewrite Eq. 1.8 in terms of safety factor $q = rB_\phi(r)/R_0 B_\theta(r)$ to give $B_*(r) = B_\theta(r)[1 - q(r)]$. Finally, we expand $q(r)$ to lowest order in r for a small displacement ($2\rho_e$) from r_s, to approximate the reconnecting magnetic field at the electron dissipation layer as $B_{*e} \simeq B_\theta q' 2\rho_e$, where the prime denotes a radial derivative. With these substitutions, Eq. 3.5 becomes

$$\frac{|p_e'|}{e n_e B_h} > \frac{2\rho_e B_\theta}{\sqrt{4\pi m_e n_e}} |q'| , \tag{3.16}$$

where all quantities are evaluated at r_s. This expression is reminiscent of the condition on p' and q' for the suppression of sawteeth derived from quasi-linear tearing theory (*Zakharov et al.*, 1993, 1994; *Levinton et al.*, 1994), and can be directly tested with experimental observations.

3.7 Conclusions

To summarize this chapter, we have proposed a new model of incomplete reconnection in sawteeth, whereby collisionless reconnection self-consistently increases the electron pressure gradient at the reconnection site, leading to the suppression of reconnection if the pressure gradient reaches a threshold. We tested the basic physics of the proposed model with two-fluid numerical simulations in a slab geometry, and showed that the model is consistent with simulations and with data from MAST. Equation 3.5 may be useful for low-dimensional transport modeling, which currently use ad hoc models to achieve incomplete reconnection

(*Bateman et al.*, 2006). The present results are machine independent, so they should apply both to existing tokamaks and future ones such as ITER.

However, while these proof-of-principle simulations have supported our new incomplete reconnection model, additional simulations must be performed to directly connect to experimental results. In a slab geometry, the model should be tested with other extended-MHD effects such as ion diamagnetic effects and higher thermal conductivity $\chi_{||}$. The restriction on toroidal mode number n should be relaxed as well. The effect of the electron pressure profile on reconnection dynamics and the secondary (KH-drift) instability should be addressed; this may need to utilize gyro-kinetic or particle-in-cell simulations.

Including 3D toroidal geometry is critical for exploring how reconnection self-consistently evolves the stabilizing diamagnetic effects during the sawtooth crash phase in tokamaks and the subsequent secondary ideal-MHD instabilities. In the following chapter, we will explore sawtooth simulations employing the extended-MHD, 3D toroidal geometry code, M3D-C^1.

Chapter 4

3D Toroidal Sawtooth Simulations

To investigate reconnection in sawteeth in a 3D toroidal geometry, in this chapter we analyze simulations employing this geometry for simulations using resistive-MHD and two-fluid physics models. We will examine these simulations from both a holistic perspective and, unlike all previous studies, also study the reconnection local to the reconnection site. To view data local to the reconnection site, we employ a novel method that samples data in the plane perpendicular to the local magnetic field, rather than at a constant toroidal angle, as is customary. By viewing data in the plane of reconnection, we find that collisionless reconnection is crucial, and that the pressure gradient at the X-line self-consistently increases, as predicted in Ch. 3. Because the model for incomplete reconnection in Ch. 3 relies on local diamagnetic and reconnection physics, we also concentrate on how these processes vary at different toroidal locations.

4.1 The M3D-C1 Code

In order to properly diagnose the magnetic reconnection phase of the sawtooth crash, it is necessary to run simulations in a toroidal geometry compared to the slab geometry of the last chapter, which undoubtedly affects the evolution due to the plasma shaping and curved geometry. For this task we employ the extended-MHD code M3D-C^1 (*Ferraro and Jardin*, 2009). Compared to the F3D code discussed in the last chapter, M3D-C^1 uses vastly different numerical methods. For the spatial representation, M3D-C^1 has 3D finite elements with continuous first derivatives between elements (C^1 means continuous first derivatives), effectively approximating the form of solution by expanding it in a series of basis functions and evolving their weights rather than approximating the spatial derivatives in the numerical method, as is the case for a finite difference code like F3D. In the poloidal plane M3D-C^1 uses a reduced-quintic (fourth order polynomial with additional constrained coefficients) representation for the solution on an irregular triangular grid, and a cubic (third order polynomial) representation toroidally; this gives the elements a triangular prism shape. If the average length of an element edge in the poloidal plane is Δx, the reduced-quintic representation has an error on the order of $(\Delta x)^5$ (*Jardin*, 2004). M3D-C^1 also uses an unconditionally stable, fully-implicit time stepping method to evolve the model equations in time; implicit schemes evaluate spatial derivatives at the time step being solved for, allowing for timesteps much larger than the Courant-Friedrichs-Lewy condition constraining the timestep in explicit methods requires.

Adapted from *Ferraro and Jardin* (2009), the system of extended-MHD equations that M3D-C^1 steps forward for the density n, velocity $\mathbf{v}$, ion and electron pressure p_i and p_e, and

magnetic field $\mathbf{B}$ is:

$$\frac{\partial n}{\partial t} + \nabla \cdot (n\mathbf{v}) = 0, \tag{4.1}$$

$$nM_i \left(\frac{\partial \mathbf{v}}{\partial t} + \mathbf{v} \cdot \nabla \mathbf{v} \right) + \nabla p = \mathbf{J} \times \mathbf{B} - \nabla \cdot \mathbf{\Pi_{GV}} - \nabla \cdot \mathbf{\Pi}_\mu, \tag{4.2}$$

$$\mathbf{E} + \mathbf{v} \times \mathbf{B} = \eta \mathbf{J} + \frac{1}{ne} (\mathbf{J} \times \mathbf{B} - \nabla p_e), \tag{4.3}$$

$$\frac{3}{2} \left[\frac{\partial p_e}{\partial t} + \nabla \cdot (p_e \mathbf{v}) \right] = -p_e \nabla \cdot \mathbf{v} + \eta J^2 - \nabla \cdot \mathbf{q_e}, \tag{4.4}$$

$$\frac{3}{2} \left[\frac{\partial p_i}{\partial t} + \nabla \cdot (p_i \mathbf{v}) \right] = -p_i \nabla \cdot \mathbf{v} + \mathbf{\Pi}_\mu \cdot \nabla \mathbf{v} - \nabla \cdot \mathbf{q_i}, \tag{4.5}$$

$$\frac{\partial \mathbf{B}}{\partial t} = -\nabla \times \mathbf{E}, \tag{4.6}$$

$$\nabla \cdot \mathbf{B} = 0, \tag{4.7}$$

$$\mu_0 \mathbf{J} = \nabla \times \mathbf{B}. \tag{4.8}$$

Eqs. 4.1, 4.6, 4.7, and 4.8 are the same as in previous chapters for the density evolution and electromagnetic equations. Eq. 4.2 for momentum evolution is similar to that seen in previous chapters with the addition of $\mathbf{\Pi}_{GV}$, the Braginskii gyroviscosity pressure tensor (*Braginskii*, 1965), and $\mathbf{\Pi}_\mu$, a generic isotropic viscosity given by $\mathbf{\Pi}_\mu = -\mu \left(\nabla \mathbf{v} + \nabla \mathbf{v}^T \right)$, where μ is an arbitrary scalar field set to 3.058×10^{-5} in the following simulations and $\nabla \mathbf{v}^T$ is the matrix transpose of $\nabla \mathbf{v}$. Eq. 4.3 is the generalized Ohm's law recognized from previous chapters, where the resistivity η has a Spitzer form given by $\eta = \eta_r + \eta_0 / T_e^{3/2}$ (we discuss the values used in the next section). The electron and ion pressure evolutions equations, Eqs. 4.4 and 4.5, are similar to those seen in previous chapters with the ratio of specific heats for both species set to 5/3, and $\mathbf{q}_{e,i}$ are the electron and ion heat fluxes given by $\mathbf{q}_{e,i} = -\kappa_0 \nabla T_{e,i} - \kappa_\parallel \mathbf{bb} \cdot \nabla T_{e,i}$, where $\kappa_0 = 4.0 \times 10^{-6} p / T_e^{3/2}$ controls the isotropic conduction and $\kappa_\parallel = 10$ the parallel conduction. The code can simulate different physical

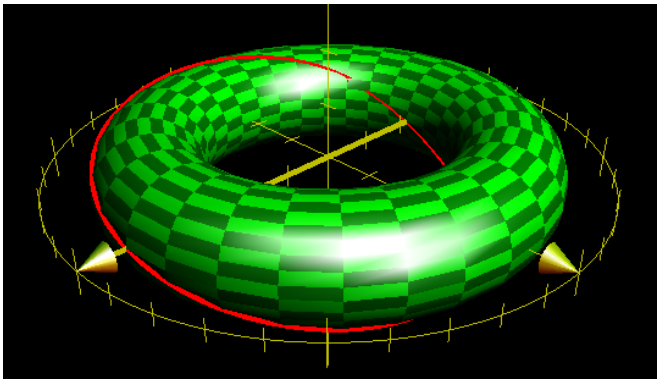

Figure 4.1: A checkered-green circular cross-section torus overlaid with a red clockwise-helical $(m, n) = (1, 1)$ field line.

models: ideal-MHD for the terms in black, resistive-MHD where the red terms are used as well, and full two-fluid including all the terms. Additionally, the electrons are assumed to be massless for simplicity.

The system of units for all quantities appearing hereafter is derived from a characteristic length, density, and magnetic field. These normalizations are $L_0 = 1$ m, $n_0 = 10^{20}$ particles/m^3, and $B_0 = 1$ T. This sets the normalization for velocity to $v_0 = B_0/(\mu_0 n_0 M_i)^{1/2} = 2.2 \times 10^6$ m/s, the Alfvén speed based off the characteristic magnetic field and density, the time to $\tau_{A0} = L_0/v_0 = 0.46$ μs, the pressure to $p_0 = B_0^2/2\mu_0 = 3.9$ atm, the electric field to $E_0 = v_0 B_0 = 2.2 \times 10^6$ V/m, and the current to $J_0 = B_0/\mu_0 L_0 = 0.80$ MA/m^2. The blue terms in Eqs. 4.2 and 4.3 are also normalized by $d_b = d_i/L_0$, allowing the user to specify the strength of the two-fluid effects. In the main two-fluid simulation presented later $d_b = 0.1$, giving $d_i = 10$ cm as compared to the value calculated from n_0 of 2.28 cm.

4.1.1 Toroidal Representation

It is useful to reintroduce the toroidal geometry, and in the process investigate how the magnetic and velocity fields are represented. In Fig. 4.1 a green checkered, circular cross-section torus is shown, and an $(m, n) = (1, 1)$ helical field line is overlaid in red. We can either use the cartesian (x, y, z) or cylindrical (R, ϕ, Z) coordinate system to keep track of the system variables; M3D-C^1 uses cylindrical coordinates. In this representation, the positive direction of ϕ is counter-clockwise looking down from the top of the torus in Fig. 4.1. The helical field line shown has a clockwise helicity relative to the ϕ-direction. R is the major radial direction from the azimuthal axis, and Z is the vertical direction, as introduced in Sec. 1.1.4.

Using the cylindrical coordinate system, M3D-C^1 represents the velocity field, magnetic vector potential, and magnetic field in terms of the (red) scalar variables $\Phi, \omega, \chi, \psi, f$ as adapted from *Breslau et al.* (2009):

$$\mathbf{v} = R\nabla\Phi \times \hat{\phi} + R\omega\hat{\phi} + \frac{1}{R^2}\nabla_\perp\chi, \tag{4.9}$$

$$\mathbf{A} = R\hat{\phi} \times \nabla f + \frac{\psi}{R}\hat{\phi} - F_0 \ln R\hat{Z}, \tag{4.10}$$

$$\mathbf{B} \equiv \nabla \times \mathbf{A} = \frac{1}{R}\nabla\psi \times \hat{\phi} - \nabla_\perp\frac{\partial f}{\partial\phi} + \frac{F}{R}\hat{\phi}, \tag{4.11}$$

where F is an auxiliary variable, given by $F = F_0 + R^2\nabla\cdot\nabla_\perp f$, where $\nabla_\perp\cdot\mathbf{V} = R^{-1}\left(R\mathbf{V}\cdot\hat{R}\right)_R + \left(\mathbf{V}\cdot\hat{Z}\right)_Z$ for any vector $\mathbf{V}$, where subscripts denote partial differentiations. Note that the gauge condition implied by this representation is $\nabla_\perp \cdot R^{-2}\mathbf{A} = 0$. Φ is the usual stream-function describing incompressible flow in the poloidal plane, ω is the toroidal angular frequency, and χ captures the effect of compressible flow in the poloidal plane. The form of the velocity field allows the numerical method evolving the scalar variables to separate the

physics of the Alfvén and fast and slow magnetosonic waves for the toroidal system with a strong B_ϕ field (*Jardin*, 2012). ψ is the usual magnetic flux function describing the magnetic field in the poloidal plane, F_0 is a constant proportional to the current in the (modelled) toroidal field magnets, and f is a poloidal field component keeping $\nabla \cdot \mathbf{B} = 0$ when the toroidal magnetic field varies in strength with the toroidal angle. Aside from ensuring the divergenceless of the magnetic field, the form of the magnetic vector potential conveniently allows for the first derivative of the current density to be continuous with the chosen finite element representation.

Compared to the 2D slab simulations using F3D in Ch. 3 that employed periodic boundary conditions, the 3D toroidal simulations using M3D-C[1] require more involved boundary conditions. The flow $\mathbf{v}$ has "no-slip" boundary conditions, where the flow tangential to the boundaries is held constant. There is no flow into the boundary, satisfying $\hat{n} \cdot \mathbf{v} = 0$, where $\hat{n}$ is the direction normal to the boundary. The normal and toroidal magnetic fields have Dirichlet boundary conditions $\hat{n} \cdot \mathbf{B} = \hat{\phi} \cdot \mathbf{B} =$ constant, and the poloidal magnetic field B_θ satisfies Neumann boundary conditions $\hat{n} \cdot \nabla B_\theta =$ constant. Additionally, the plasma parameters n, p, and T are all held constant on the boundary.

4.1.2 Simulation Setup

The evolved solution to the set of equations 4.1-4.6 for the main simulations are computed on the elements defined by the grid shown in Fig. 4.2, where the average edge of an element is equal to 0.04 m, as seen in the zoomed-in panel (b). This grid is used on 16 toroidal slices, with a total of 123936 elements solved simultaneously each timestep[1]. This resolution is

[1]Each finite element contains 60 integration points for solving the assumed form of the solution, which leads to approximately 80 extra sub-elements. In total, the code solves approximately 10 million sub-elements simultaneously each timestep.

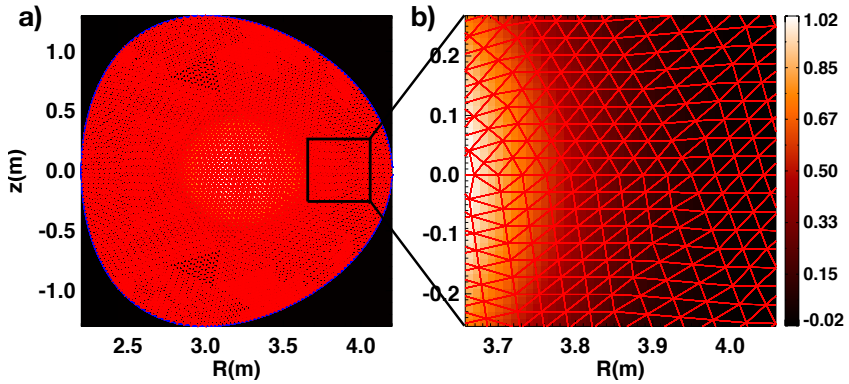

Figure 4.2: (a) View of the toroidal current at a constant toroidal angle over-plotted with the triangular finite element mesh. (b) Zoomed in portion of the domain in (a) to show the resolution of the mesh, which was chosen to have an average edge length of 0.04 m.

chosen by running multiple toroidal, nonlinear resistive-MHD simulations where we vary the resolution while keeping all other parameters constant. We check that there is no qualitative change in the solution. In the nonlinear two-fluid model, the system of equations to be solved through the implicit numerical method is much more complex than that of the resistive-MHD case. Because the iterative solver employed has a limit on the number of iterative loops for solving each timeslice, the maximum timestep that could be used was limited by a factor of ~ 10 smaller than for the resistive-MHD simulations. This restricted our ability to parametrically scan the resolution for the nonlinear two-fluid simulations, and will be a part of future studies.

The simulations start from an axisymmetric equilibrium determined from solving the Grad-Shafranov (G-S) equation (*Grad and Rubin*, 1958; *Shafranov*, 1966), using a module included in M3D-C^1. The G-S equation prescribes an equilibrium by finding the toroidally-axisymmetric solution to $\nabla p = \mathbf{J} \times \mathbf{B}$, which is the non-dissipative, steady-state force balance equation from Eq. 4.2. The solver assumes the magnetic field and gas pressure profiles have a polynomial form, and a relaxation technique is employed to approach the exact solution. Input parameters include the toroidal plasma current I_p, the central safety factor q_0 and

Table 4.1: Parameters used to solve the G-S equation, which determine the equilibrium used to initialize the main simulations in the M3D-C^1 code.

Parameter	I_p	q_0	B_0	p	p_i	p_{edge}	n_0	$expn$
Value	0.8	0.6	1.0	0.006	0.003	0.0003	1.0	0.2

toroidal magnetic field B_0, the central total and ion pressures p and p_i, the total edge pressure p_{edge}, central density n_0, and a variable named 'expn' to set the density profile off of the pressure profile as $n = p^{expn}$. Values used to generate the equilibrium for the main simulations are given in Table 4.1. The equilibrium generated for this set of inputs has a plasma column with a minor radius of approximately 0.9 m about a central major radius of $R_0 = 3.28$ m, where the $q = 1$ rational surface is located at a minor radius of $r_1 = 0.59$ m. The magnetic surfaces in the core and around the $q = 1$ surface have a predominantly circular cross-section with a small elongation (stretching in the Z direction), while those towards the edge have a modest elongation and triangulation (peaking toward the outboard edge). We note here that this equilibrium does not correspond to a particular tokamak, but is instead chosen to study the basic physics of reconnection in sawteeth.

After setting the equilibrium, simulations are perturbed by a small random perturbation in the poloidal flow on the order of $0.1c_{A\theta}$, where $c_{A\theta}$ is the Alfvén speed based off the poloidal magnetic field. The magnitude of the initial perturbation has been varied to ensure the resulting evolution is not sensitive to it.

4.1.3 Numerical Convergence

In preparation to simulate the nonlinear set of resistive-MHD or two-fluid model equations in the full 3D toroidal geometry, we perform M3D-C^1 simulations in its 2D axisymmetric nonlinear and 3D linear forms. This allows us to run a series of computationally inexpensive

simulations to probe the equilibrium parameter space, spatial and time resolution, and also the simulated plasma controllers. By running a current through the metallic vacuum vessel wall and controlling the associated "loop voltage", current controllers on tokamaks inductively keep the plasma current I_p constant. Another tokamak controller for the density, either puffing gas or shooting pellets into the plasma from the edge of the device, keeps the density constant. After setting the density controller to hold the number of particles at 8.8×10^{20} and the current controller to hold I_p at 0.8, we find where the perpendicular and parallel thermal conductivities do not qualitatively alter the evolution by running simulations with the 2D nonlinear version of the code. The values of conductivity we selected for the principal simulations were listed in Sec. 4.1.2.

There is also a 3D linear version of the code. The system of equations is expanded by making the fields complex and setting $\mathbf{A} = \mathbf{A_0} + \mathbf{A_1}$, where $\mathbf{A_0}$ is the equilibrium field and $\mathbf{A_1}$ the perturbation for all fields, then keeping only the linear terms in Eqs. 4.1-4.8. With the fields complex, the toroidal derivatives are replaced by a multiplier of in, with n being the chosen number of the toroidal mode. Employing these simplified simulations for a single n mode at a time, by holding the two-fluid parameter d_b constant and changing the resistivity, and vice-versa, we find a value of the resistivity, $\eta \sim 1.5 \times 10^{-6}$ at the $q = 1$ surface, where the two-fluid effects dominate at $d_b = 0.1$, and are well-resolved when $d_b = 0$ for $n = 0, 1, 2$.

4.2 Macroscopic Observations

To begin our analysis of sawteeth in extended-MHD toroidal simulations, we study the evolution of various modes in the linear and non-linear phase and look at data in the poloidal

plane, to make contact with the approach used in previous studies. We begin by comparing between simulations with resistive-MHD physics and two-fluid physics by looking at the kinetic energy contained in the lowest order toroidal modes and comparing poloidal cross-sections of the electron temperature. We then compare the diamagnetic physics at the $q = 1$ surface to the growth of the kinetic energy in the $n = 1$ toroidal mode associated with the tearing/reconnection mode. We end the section by exploring signatures of the reconnection and diamagnetic physics in the poloidal plane.

4.2.1 Resistive Vs. Two-Fluid Simulations

Recall our discussion from Ch. 2, where we explored studies in simple geometries that showed two-fluid effects solve the timescale problem of Kadomtsev's model. There are only limited direct comparisons between sawteeth in 3D toroidal simulations with resistive-MHD and two-fluid models (*Breslau et al.*, 2007). We show that the inclusion of two-fluid physics in the model equations is essential for recovering timescales more closely in line with experimental results compared to resistive-MHD and contrast the dynamics in the two models. In Fig. 4.3, the evolution of the kinetic energy in different toroidal modes is shown for the (a) resistive-MHD and (b) two-fluid models. The only difference between the simulations is $d_b = 0$ for (a) and $d_b = 0.1$ for (b). Repeated again for reference, with the chosen normalizations the time unit corresponds to $\tau_{A0} = 0.46$ μs. The first striking difference between the two simulations is the disparity in the timescales, where the two-fluid simulation evolves from $t = 0$ to its maximum kinetic energy in roughly a quarter of the time it takes for the resistive-MHD simulation. To reinforce this point because the panels in Fig. 4.3 use different time scales, the calculated growth rate of the kinetic energy in the $n = 1$ toroidal mode is ~ 0.005 for the resistive case and ~ 0.015 for the two-fluid case.

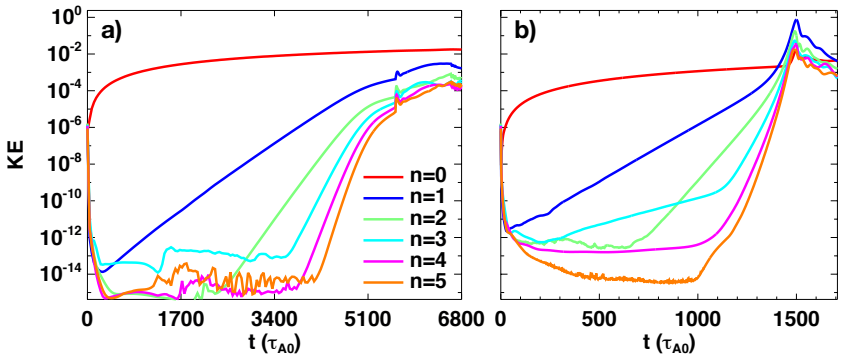

Figure 4.3: Kinetic energy in toroidal modes $n = 0 - 5$ in (a) resistive-MHD and (b) two-fluid simulations. Note the much faster timescales associated with the growth of the modes in the two-fluid simulations, and also the late nonlinear acceleration of the growth for the two-fluid case as compared to the deceleration of the mode growth in the resistive case.

A second important observation in Fig. 4.3 is the nonlinear acceleration of the kinetic energy growth rates for the two-fluid simulation from $t \sim 1400 - 1500$ and a deceleration of the mode growth for the resistive simulation after $t \sim 5000$. This implies that reconnection is not only faster for the two-fluid simulation, but also increases in rate as the reconnection phase proceeds, while the resistive simulation has slower reconnection that slows even further during the reconnection phase. The acceleration of the mode growth rate is similar to results from *Biskamp et al.* (1997), where reduced, two-fluid simulations showed an accelerating growth rate during the reconnection phase across a parameter space of poloidal beta and density gradient widths.

A third important difference between the resistive-MHD and two-fluid simulations is the time it takes for reconnection to process the magnetic fields and expel the hot plasma in the core, the timescale of the sawtooth crash phase. Shown in Figs. 4.4 and 4.5 for the resistive and two-fluid simulations, respectively, is the electron temperature in the poloidal plane at a constant toroidal angle for different times throughout the reconnection phase, where the white x's mark the location of the reconnection site as determined from Poincaré plots and poloidal plane velocity data. More closely in line with experimental observations,

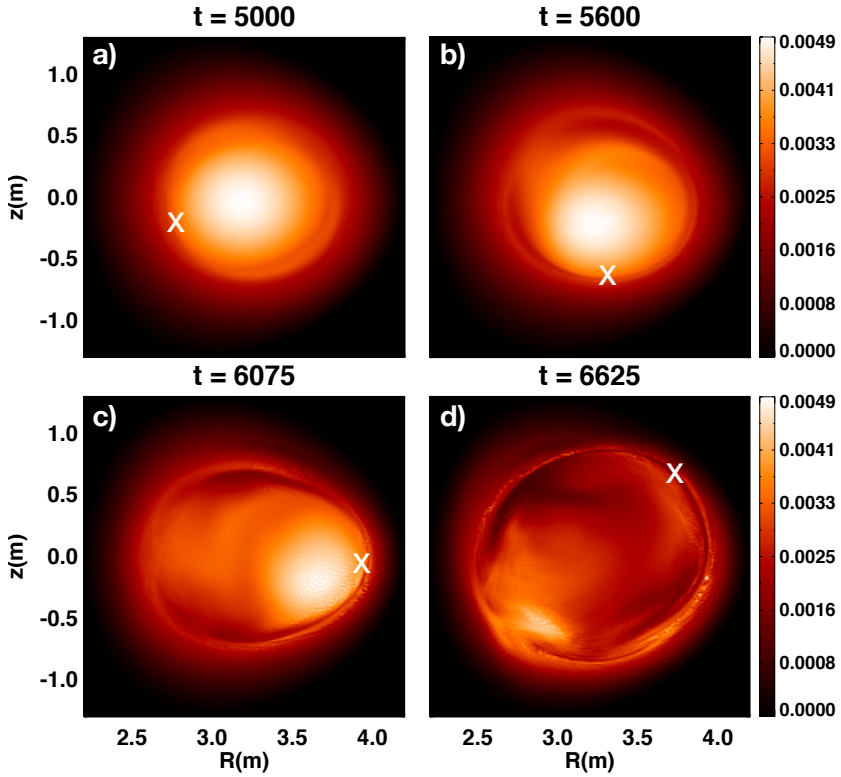

Figure 4.4: Poloidal cross-sections of the electron temperature during the reconnection phase of the sawtooth crash for the resistive-MHD simulation. The white x's show the location of the reconnection site as determined from Poincaré sections, where the counter-clockwise poloidal drift is due to the external neutral beam adding torque to the system and causing the helical mode to rotate toroidally.

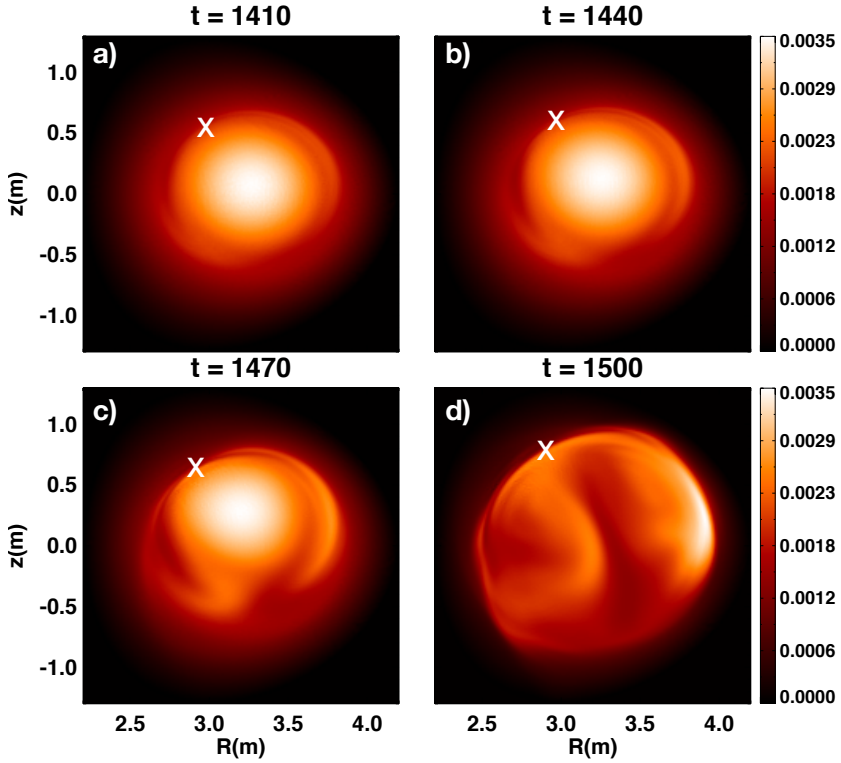

Figure 4.5: Poloidal cross-sections of the electron temperature throughout the reconnection phase of the sawtooth crash for the two-fluid simulation. The white x's show the location of the reconnection site as determined from Poincaré sections. Note that the timescale of the core expulsion is over a factor of 15 shorter than for the resistive simulation.

reconnection processes the hot core in the two-fluid simulation in ~ 50 μs, approximately 15 times more rapidly than in the resistive-MHD simulation, which processes the core in ~ 750 μs.

Another difference between Fig. 4.4 and Fig. 4.5 is the poloidal drift of the reconnection site in the counter-clockwise poloidal direction for the resistive case, while it is not prominent for the two-fluid case. Torque imparted by the simulated neutral beam causes the helical mode to rotate in the positive toroidal direction, which appears as a counter-clockwise poloidal drift of the reconnection site. This is consistent with the experimental results of *Yamaguchi et al.* (2004) discussed in Ch. 1. However since their plasma current I_p was directed opposite to the toroidal field and neutral beam, they observed rotation in the

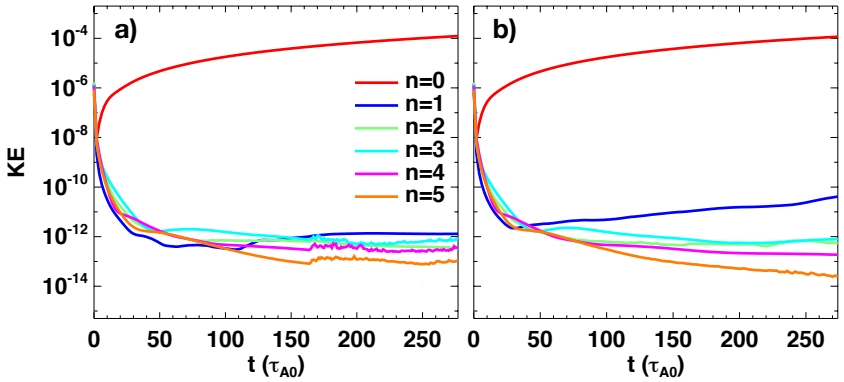

Figure 4.6: Early time evolution of the kinetic energy in different toroidal modes for two-fluid simulations with central pressure (a) $p_0 = 0.007$ and (b) $p_0 = 0.006$. The $n = 1$ mode is stabilized for the higher central pressure in (a) corresponding to increased electron diamagnetic effects at the $q = 1$ rational surface that stabilize magnetic tearing, while the mode grows in (b).

clockwise poloidal direction as seen in Fig. 1.11. Since the reconnection phase starts much later in the resistive simulation and also evolves over a longer timescale, the toroidal rotation is apparent for this simulation. However there is much less time for torque to be imparted in the two-fluid simulation, and because of this, the poloidal drift of the reconnection site due to the neutral beam is not observed in Fig. 4.5.

4.2.2 Diamagnetic Suppression

A main subject discussed in the proceeding chapters has been how electron diamagnetic physics affects magnetic reconnection, and in this section we discuss how diamagnetic effects appear in toroidal simulations. The origin of diamagnetic physics in tokamaks begins with the equilibrium pressure profile consistent with the solution to the G-S equation for a given magnetic field and current profile and the toroidal geometry of the system. To change the pressure profile in our simulations, we change the central total and ion pressures p and p_i used to find an equilibrium. By changing the central pressures while keeping their edge values constant, we are able to vary the value of the electron pressure gradient at the $q = 1$

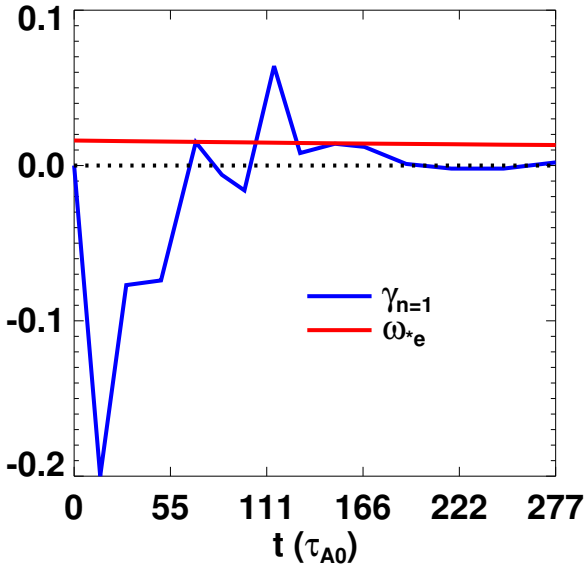

Figure 4.7: Evolution of the two terms in Eq. 4.12, the $n = 1$ toroidal mode growth rate $\gamma_{n=1}$ (blue) compared to the electron diamagnetic frequency $\omega_{*e} = -c\nabla p_e/enBr|_{r_1}$ (red), for the two-fluid simulation with $p_0 = 0.007$. While $\gamma_{n=1}$ eclipses ω_{*e} for a short time, it drops back down and becomes negative, showing that tearing is diamagnetically suppressed for this value of p_0.

rational surface. For higher central pressures, tearing is stabilized by diamagnetic effects. This is seen in Fig. 4.6, showing the time evolution of the kinetic energy associated with the first six toroidal modes $n = 0 - 5$. In (a) the central total pressure is set at $p_0 = 0.007$; the $n = 1$ tearing mode (the blue trace) remains relatively flat. Conversely in (b) where $p_0 = 0.006$ is only slightly lower (and all other parameters are identical), the $n = 1$ mode grows continually. This suggests diamagnetic effects are playing a key role.

To make the observation of the stabilized $n = 1$ mode in Fig. 4.6(a) more quantitative, we recall that *Rogers and Zakharov* (1995) discussed the importance of the linear $m = 1$ mode growth rate $\gamma_{m=1}$ compared to the diamagnetic frequency $\omega_* = -c\nabla p/qnBr|_{r_1}$, and *Biskamp et al.* (1997) emphasized that the maximum nonlinear growth rate as the system evolves is the important growth rate to compare to ω_{*e}. Coupling these results give a quantitative

threshold condition that predicts the stabilization of reconnection as

$$\omega_{*e} > \gamma_{m=1}. \tag{4.12}$$

Since M3D-C^1 outputs data for the toroidal modes n that contain information on all poloidal modes m, and also since our previous discussion suggests the $(m, n) = (1, 1)$ mode is dominant, we expect $\gamma_{m=1} \sim \gamma_{n=1}$. Thus, Fig. 4.7 shows $\gamma_{n=1}$ compared to ω_{*e} for the simulation with $p_0 = 0.007$ during the early nonlinear evolution. We evaluate ω_{*e} by finding the radial electron pressure gradient, density, and toroidal magnetic field at the $q = 1$ surface along the midplane ($z = 0$) at the toroidal angle where the reconnection site is on the inboard side. Fig. 4.7 shows that while $\gamma_{n=1}$ eclipses ω_{*e} for a short time, it quickly decreases to below zero, and stays small for the rest of the simulated time so Eq. 4.12 is satisfied and tearing is diamagnetically suppressed. It would be worth extending this simulation to later times to ensure the result does not change (future studies), but to our knowledge Figs. 4.6(a) and 4.7 show the first observed stabilization of the $(m, n) = (1, 1)$ tearing mode due to electron diamagnetic effects in nonlinear, non-reduced, toroidal simulations. *Rogers and Zakharov* (1995) employed a reduced set of the two-fluid equations and neglected toroidal curvature at the $q = 1$ surface.

For the two-fluid simulation in Fig. 4.6(b) with $p_0 = 0.006$, where the $n = 1$ toroidal mode continues to grow past the early nonlinear phase, we show the same two terms in the threshold relation Eq. 4.12 extended over a time range encompassing the full reconnection phase in Fig. 4.8. As we saw in the last section, the time range from $\sim 1400 - 1500$, where the $\gamma_{n=1}$ mode grows rapidly, corresponds to the sawtooth crash phase. Since $\gamma_{n=1}$ is greater than ω_{*e} throughout the late nonlinear evolution, reconnection is never stabilized. The

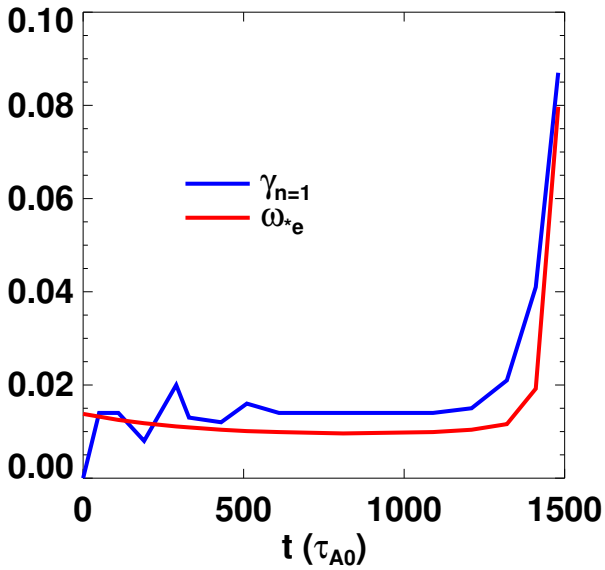

Figure 4.8: Time history of Eq. 4.12, the $n = 1$ toroidal mode growth rate $\gamma_{n=1}$ (blue) compared to the electron diamagnetic frequency ω_{*e} (red), throughout the full sawtooth cycle for the two-fluid simulation with $p_0 = 0.006$. Since $\gamma_{n=1}$ is always greater than ω_{*e}, the threshold is never met, so reconnection is complete.

core plasma is completely processed during the crash for the chosen simulation parameters; reconnection is complete.

Thus, these two simulations result in complete reconnection or complete suppression. We note that neither was incomplete, so we are unable to test the model in Ch. 3. Since the outflows due to reconnection scale with the Alfvén speed and therefore with the density as $\sim n^{-1/2}$, while the diamagnetic drift speed scales with density as $\sim n^{-1}$, in order to test the model of incomplete reconnection given in the last chapter, future work will employ simulations at an intermediate value of the central pressure or lower values of density where diamagnetic effects play a larger relative role during the reconnection phase.

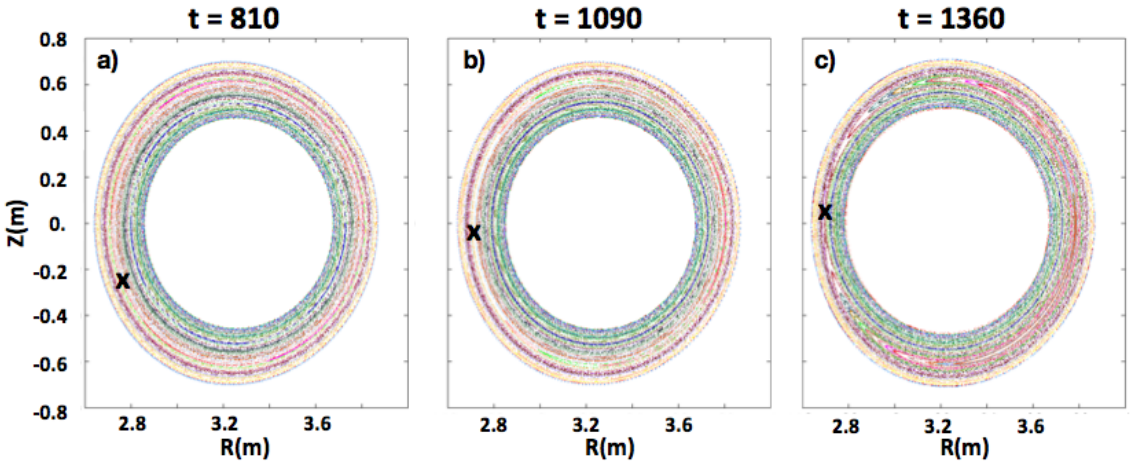

Figure 4.9: Poincaré sections for an annulus centered around the $q = 1$ surface spanning from the beginning of tearing of the $(m, n) = (1, 1)$ mode to the reconnection phase for the two-fluid simulation. With the toroidal field directed into the plane and an electron pressure directed towards the core, the black x's show the tearing/reconnection site drifting poloidally in the electron diamagnetic drift direction.

4.2.3 Reconnection and Diamagnetic Physics in the Poloidal Plane

Moving from the discussion of macroscopic signatures of reconnection compared between the resistive-MHD and two-fluid simulations, we now look at data in the poloidal plane to ascertain details of two-fluid reconnection in sawteeth. At the end of the last section, we saw that the reconnection site in the two-fluid simulation showed little to no drift in the poloidal plane. However, we expect electron diamagnetic physics to convect the magnetic field structure in the clockwise poloidal direction for B_ϕ in the positive toroidal direction and an electron pressure gradient directed towards the core, and the neutral beam to rotating the helical mode toroidally. In Fig. 4.9, we show Poincaré plots encompassing the early tearing/reconnection phase of the two-fluid simulation, where the tearing site is marked by black x's. At $t = 810$ and $t = 1090$ in Fig. 4.9(a) and (b), by measuring quantities along the midplane at the $q = 1$ surface for a toroidal angle where the tearing site intersects the inboard side, we calculate v_{*e} to be 0.0056 and 0.0058, consistent with a drift distance of

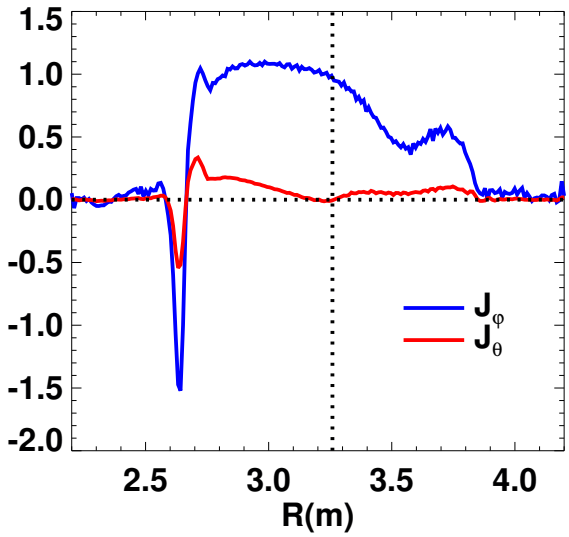

Figure 4.10: Profiles of the (blue) toroidal and (red) poloidal currents taken through the midplane of a poloidal cross-section, where the positive poloidal direction is taken to be clockwise. Since the helical mode is clockwise when moving in the positive toroidal direction, the current at the reconnection site located around $R = 2.63$ m is opposite to the helical direction.

~ 1.6 m in the clockwise direction during this time interval.

In the Poincaré plots a drift of only ~ 0.25 m is observed over the same time interval in the clockwise direction. However this is consistent with results from the two-fluid simulations in the last chapter, where the reconnection site drifted at a speed $\sim 1/5$ of that calculated for v_{*e}. This suggests there is physics in addition to diamagnetic effects that control the X-line drift. Future work should investigate this further.

Shown in Fig. 4.10 are profiles of the toroidal and poloidal (with positive in the clockwise direction) components of the current through the midplane for time unit $t = 1460$ at toroidal angle $\phi = 279^{\circ}$, where the reconnection site is directly on the inboard side. The $q = 1$ rational surface is located near $R = 2.63$ m, and both components of the current are directed opposite to their direction over the rest of the domain. Thus, while the current consistent with the confining magnetic configuration is in the positive toroidal and clockwise poloidal direction, the reconnection current sheet is opposite, in the negative helical direction. A consequence

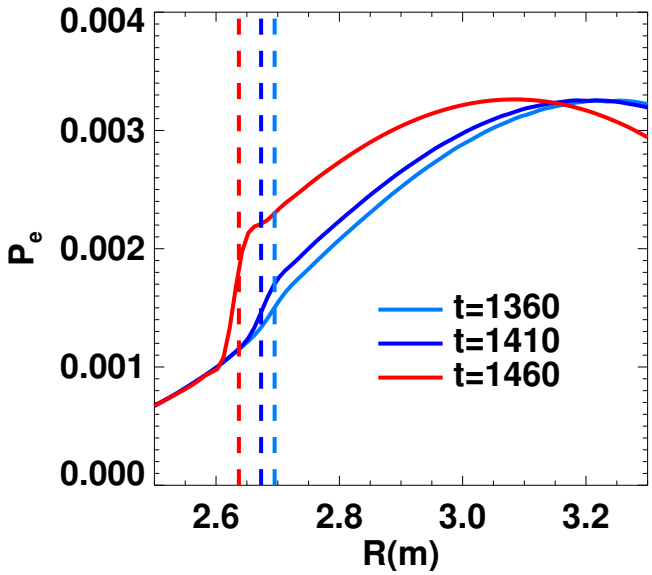

Figure 4.11: Self-consistent increase of the electron pressure profile through the reconnection site as reconnection progresses. Profiles are taken at the midplane of the poloidal cross-section where the reconnection site is directly on the inboard side of the helical mode. The vertical, dashed lines indicate the location of the $q = 1$ rational surface at the corresponding time.

of the reconnection current being directed opposite to current at the core is that there is a motion of the $q = 1$ rational surface towards the edge (since oppositely directed currents repel each other). This is consistent with the observations in Figs. 4.4 and 4.5. We expect that for a different value of central safety factor q_0 closer to unity, the reconnection current would be along the helical mode, in the same direction as the confining current. This is borne out in 3D linear simulations (not shown), and will be a focus of future work. The motion of the $q = 1$ surface during reconnection could play a role in the seeding of NTMs and disruptions. If the surface expands radially, the reconnection mode would be more likely to trigger disruptive activity, but if the surface contracts into the core, the mode would be sequestered.

A central part of the diamagnetic cessation model for incomplete sawteeth presented and investigated in Ch. 3 is that reconnection self-consistently increases the pressure gradient at the reconnection site, shutting off reconnection if the gradient becomes large enough. While

the two-fluid simulations presented in this chapter do not produce incomplete reconnection, we can test to see if the pressure at the X-line self-consistently increases as the model suggests. Fig. 4.11 shows that reconnection causes the pressure gradient to increase at the $q = 1$ rational surface, which are shown by the vertical, dashed lines for $t = 1360$, 1410, and 1460 during the evolution. This is qualitatively consistent with the model and with the experimental results of *Chapman et al.* (2010) which detailed a rise of ∇p_e in Fig. 3.7.

4.3 Local Properties of Reconnection in 3D Toroidal Geometry

To properly diagnose reconnection in a 3D toroidal geometry, it is necessary to find the plane perpendicular to the magnetic field located at the reconnection site; in this plane, the magnetic field is antiparallel about the rational surface. While looking at data in the poloidal plane as done in Sec. 4.2 is sufficient to gain a qualitative understanding of the reconnection physics, we must sample our data in the correct plane to quantitatively diagnose reconnection in a tokamak. Here, we present the first analysis of the reconnection plane in a 3D toroidal geometry.

4.3.1 Finding the Reconnection Plane

In Fig. 4.12 the reconnection geometry is shown at the location indicated by the red dot for a circular toroidal geometry. While reconnection takes place all along the $(m, n) = (1, 1)$ field line shown, in Fig. 4.12 the reconnection site is shown on the inboard side of the torus. We note here that the discussion in this section is limited to looking at the reconnection site on the inboard of the torus for simplicity, but an analysis of the toroidal dependence of

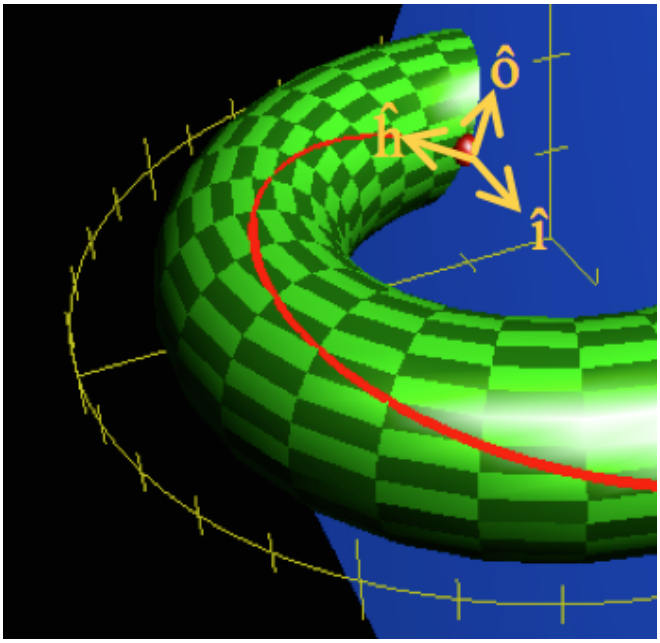

Figure 4.12: A checkered-green circular cross-section torus overlaid with a red clockwise-helical $(m, n) = (1, 1)$ magnetic field line. A location of the reconnection site is marked by the red dot, the direction of the local field is denoted by $\hat{h}$, the normal to the $q = 1$ surface is the direction of the reconnection inflow denoted by $\hat{i}$, and the reconnection outflow completes the orthogonal set denoted by $\hat{o}$. The reconnection (blue) plane is spanned by $\hat{i}$ and $\hat{o}$, perpendicular to $\hat{h}$.

reconnection will be explored in Sec. 4.4.

We find the reconnection site by using Poincaré plots and data sampled in the poloidal plane. First, Poincaré plots allow us to estimate the location of the reconnection site. Then, we expect the pressure gradient to be an extremum at the reconnection site, so we refine the minor radial location of the site to match this extremum. We note that while the field line tracing algorithm used to generate the Poincaré plots from M3D-C^1 data accurately finds the $q = 1$ surface, there also exists a separate IDL analysis code that estimates the $q = 1$ surface by averaging the magnetic field over the toroidal and poloidal angles. However, the latter method is not accurate enough for our purposes as the $(m, n) = (1, 1)$ reconnection mode evolves and varies in the toroidal and poloidal directions.

Having an approximate location of the reconnection site in the poloidal plane, we next

find the reconnection plane. The direction of the local magnetic field at the reconnection site is denoted by $\hat{h}$ (for "helical") in Fig. 4.12. This unit vector defines the blue plane shown in the figure, which we expect to be the reconnection plane. We then use the fact that we limited our analysis[2] to the reconnection site at the inboard side of the torus to set the tangent to the $q = 1$ rational surface $\hat{c} = \hat{Z}$ (not shown in Fig. 4.12). The cross product $\hat{c} \times \hat{h}$ is normal to both the magnetic field and the $q = 1$ rational surface, corresponding to the inflow direction; we normalize the result, and denote it as the inflow direction $\hat{i}$. Then by taking the cross product $\hat{h} \times \hat{i}$, we find the outflow direction $\hat{o}$, which completes the orthonormal reconnection frame. By sampling data[3] in the plane defined by $\hat{h}$ and spanned by $\hat{i}$ and $\hat{o}$, we can properly diagnose magnetic reconnection during the crash phase of sawteeth.

4.3.2 Quantifying Properties of Reconnection

4.3.2.1 Resistive Versus Two-Fluid Reconnection

In the reconnection plane, we continue our quantitative analysis of magnetic reconnection during the crash phase of sawteeth. We start by comparing reconnection between simulations with resistive-MHD and two-fluid model equations. In Fig. 4.13 the current sheet of the out-of-plane (helical) current J_h is shown for (a) resistive-MHD and (b) two-fluid. The times are chosen for where the two-fluid simulation is well into the accelerated nonlinear phase $t = 1460$, and where the resistive simulation has an island size comparable to that of the two-fluid case at $t = 5625$. The dominant feature in this figure is that the resistive current sheet is elongated compared to the two-fluid current sheet. By measuring where J_h falls to

[2]While we discuss the case of the reconnection site only on the inboard side, a simple extension is applicable to other toroidal angles.

[3]Data is sampled locally by interpolating between the simulation data computed at each node of the finite element mesh, where the order of interpolation is consistent with the spatial representation of the finite elements.

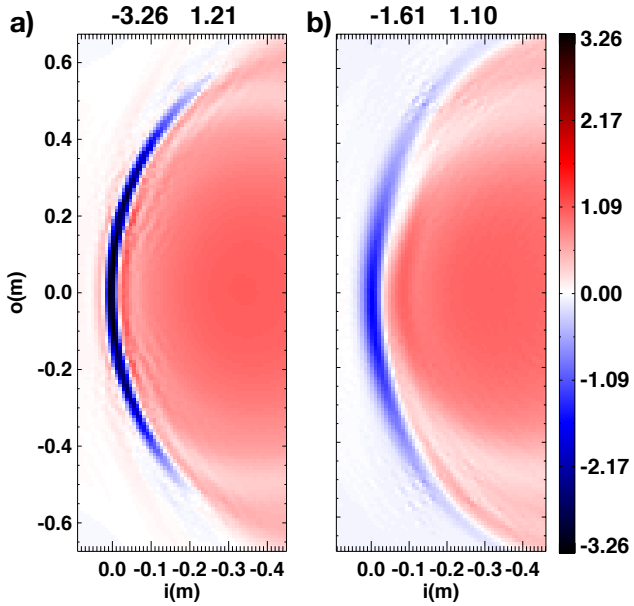

Figure 4.13: Helical current J_h as viewed in the reconnection plane for the (a) resistive-MHD and (b) two-fluid simulations. By finding where the current falls to half its maximum, δ/L can be calculated for both sheets; $\delta/L \sim 0.07$ for the resistive case and ~ 0.17 for the two-fluid simulation, which is consistent with the elongated current sheet of Sweet-Parker reconnection, and the localized current sheet of collisionless reconnection.

half its maximum value in the inflow and outflow directions, we find the thickness δ and the length L of the current sheet. The resistive sheet is elongated with $\delta/L = 0.07$ compared to the two-fluid current sheet, where $\delta/L = 0.17$. The two-fluid result is in reasonable agreement with values seen in 2D slab geometry simulations, while resistive reconnection with smaller δ/L forms a nozzle which slows reconnection. Interestingly, due to our choice of $\eta = 1.5 \times 10^{-6}$ and $d_b = 0.10$, the resistive current sheet is thinner than the two-fluid current sheet, which may seem counter-intuitive. However this is a nice consistency check that two-fluid physics are dominant in the simulation shown in Fig. 4.13(b). It justifies our choice for η; if the width of the current sheet for the resistive simulation was larger than for the two-fluid simulation, the two-fluid effects would be washed away for the simulation with $d_b = 0.10$.

To further quantify the difference between the reconnection process in the resistive-MHD

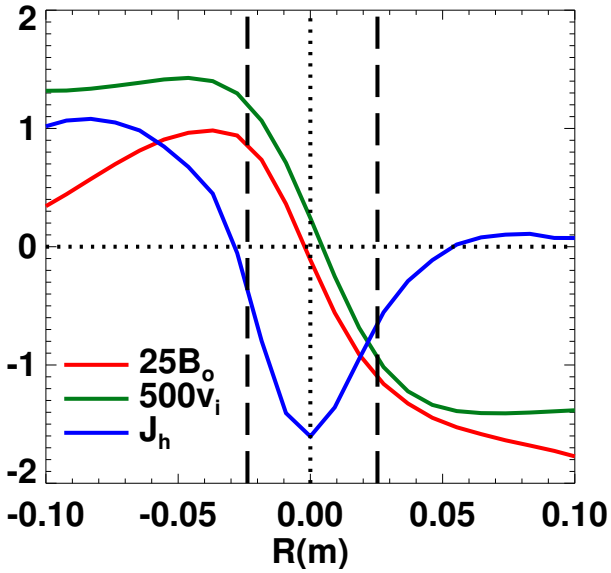

Figure 4.14: Profiles of the reconnecting field B_o, the inflow velocity v_i, and the helical current J_h. Where J_h drops to half its maximum value, denoted by the vertical, dashed black lines, upstream quantities are evaluated and used in scaling expressions. The inflow velocity profile has been shifted into the moving frame of the reconnection site outward from the core at $v_{i,xl} = 2.3 \times 10^{-3}$, and the reconnecting field exhibits a weak asymmetry.

and two-fluid simulations, we must boost into the reference frame of the reconnection site, which drifts in the positive $\hat{i}$ direction, towards the tokamak edge, as discussed earlier. This drift $v_{i,rec}$ is quantified by assuming that the out-of-plane electric field E_h is uniform in the reference frame of the reconnection site, and since this field is primarily comprised of the convective electric field upstream in the inflow direction, from *Mozer et al.* (2002):

$$v_{i,rec} = \frac{E_1 - E_2}{B_{1,o} + B_{2,o}}, \tag{4.13}$$

where $E_\alpha = v_{\alpha,i} B_{\alpha,o}$ is the convective electric field in either inflow region, $v_{\alpha,i}$ is the inflow velocity, and $B_{\alpha,o}$ is the reconnection magnetic field for $\alpha = 1, 2$ referring to the inflow region for positive i and negative i, respectively.

Values for $B_{\alpha,o}$ and $v_{\alpha,i}$ on either side are determined by taking a cut of J_h in the inflow $(\hat{i})$ direction. Fig. 4.14 shows J_h as a function of position for the two-fluid simulation as the

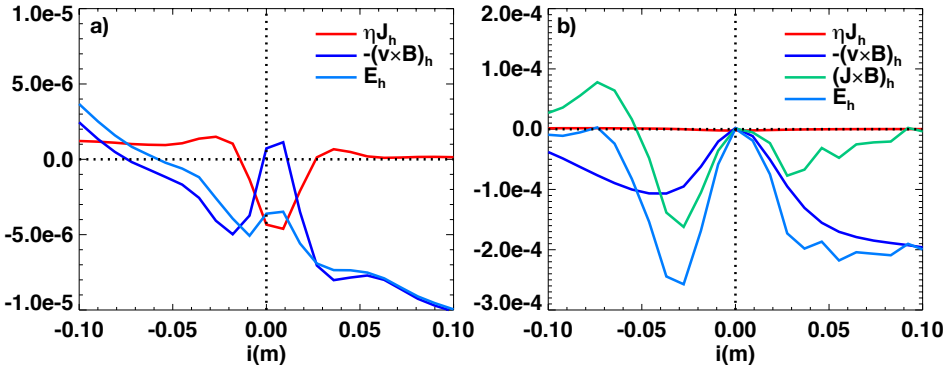

Figure 4.15: Profiles of terms in the out-of-plane component of the generalized Ohm's law taken through the reconnection site of data sampled in the reconnection plane. In (a), the resistive-MHD results are shown, with contributions from resistive diffusion balancing convection. In (b) are the two-fluid simulation results. The contribution due to diffusion is very minor while the contributions due to convection and the Hall term are appreciable.

blue trace. Vertical dashed lines denote where J_h falls to half of its absolute maximum. This defines the thickness of the reconnection site in the inflow direction, and is where values for $B_{\alpha,o}$ and $v_{\alpha,i}$ are taken. With these values, the calculated drift speed of the reconnection site from Eq. 4.13 toward the edge are 1.2×10^{-4} and 2.6×10^{-3} for the resistive and two-fluid cases. This value of $v_{i,rec}$ is used to boost into the reference frame of the reconnection site. The inflow speed v_i in this frame of reference is given by the green trace in Fig. 4.14. Additionally, the reconnecting field B_o is shown by the red trace, exhibiting a weak asymmetry ($B_{1,o}$ is slightly different than $B_{2,o}$).

After boosting into the reference frame of the moving X-line, we look at profiles of contributions to the out-of-plane electric field E_h in the generalized Ohm's law taken through the reconnection site in the inflow direction at $o = 0$. These profiles are shown in Fig. 4.15 for the (a) resistive and (b) two-fluid simulations. For the resistive simulation, the only terms that contribute are convection $-(\mathbf{v}\times\mathbf{B})_h$ and diffusion due to resistivity ηJ_h, shown by the dark blue and red lines respectively. They essentially balance, as one expects for steady-state 2D reconnection. For the two-fluid simulation, the dominant terms are convection and the

Hall term $(\mathbf{J} \times \mathbf{B})_h$ shown as the mint green line. The resistivity has a negligible contribution to E_h. The sums of all the terms are also shown in both figures as the light blue line.

In the moving frame of the reconnection site, the profiles are recognizable as similar to 2D reconnection in a slab geometry. However, here the toroidal geometry gives the convective electric field a profile that decreases towards the edge, rather than being flat throughout the domain. Still, we find that the measured reconnection electric field for the two-fluid simulation is $\sim 2 \times 10^{-4}$, which is 40 times larger than that of the resistive simulation at $\sim 5 \times 10^{-6}$, in line with collisionless reconnection being much faster than resistive reconnection. In Fig. 4.15(b) the plotted terms in Ohm's law are seen to be around zero at the origin. This is because in two-fluid reconnection, the physics that breaks the magnetic field is not due to resistive diffusion, but rather electron inertia or off-diagonal elements of the electron pressure tensor. In this simulation without these effects, the mechanism breaking the frozen-in condition is undoubtedly numerical. Fortunately, the large scale effects of collisionless reconnection are relatively insensitive to this physics (*Birn et al.*, 2001). Testing how the present results are affected when the dissipation mechanism is explicit should be the subject of future work. In summary, we find that the local measure of the reconnection rate shows that two-fluid is much faster than collisional reconnection, consistent with the global measures discussed earlier.

4.3.2.2 Comparing Asymmetric Reconnection Rates

In this section and the remainder of the chapter, we turn our discussion exclusively to the two-fluid simulation. Here, we calculate the rate of reconnection by employing analytical predictions and then compare it to the measured value for the inboard reconnection site at $t = 1460$ discussed in the last section. The in-plane magnetic field structure is displayed in

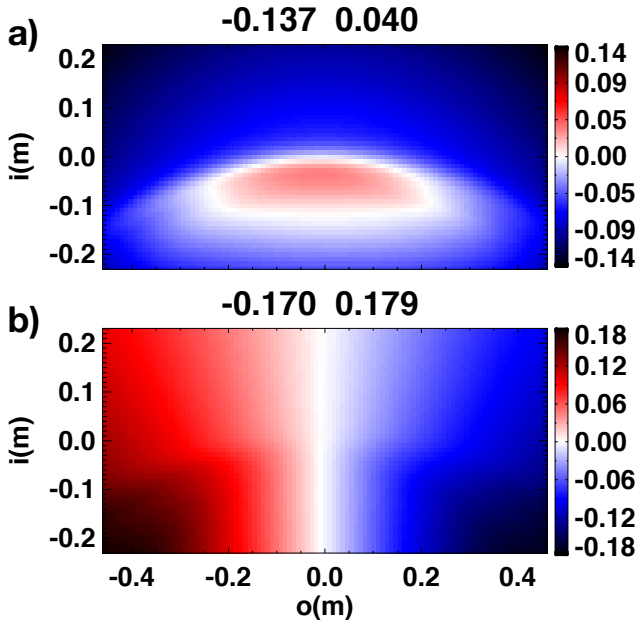

Figure 4.16: Magnetic fields in the (a) $\hat{o}$ direction and (b) $\hat{i}$ direction sampled in the reconnection plane. The reconnection site is at $(i, o) = (0, 0)$ and the field structure there is consistent with both components changing directions.

Fig. 4.16, showing the magnetic fields in the (a) $\hat{o}$ and (b) $\hat{i}$ directions. The color table used here and throughout the remainder of the chapter is set with white being 0, red positive, and blue negative. The polarity of these fields at the origin is consistent with an X-type null. Furthermore, the magnetic field in the $\hat{o}$ direction is the reconnecting field, and it exhibits a weak asymmetry as was also seen in Fig. 4.14. An asymmetry in the reconnecting field is consistent with the drift of the reconnection site in the inflow direction (*Ugai*, 2000; *Cassak and Shay*, 2007, 2008; *Hoshino and Nishida*, 1983; *Scholer*, 1989b; *Rijnbeek et al.*, 1991).

Using the values for the reconnecting field B_o and the inflow velocity v_i evaluated at the upstream locations shown by the vertical black dashed lines in Fig. 4.14 as discussed in the last section, we can calculate the reconnection electric field (reconnection rate) from *Mozer et al.* (2002):

$$E_{rec,1} = \frac{E_1 B_2 + E_2 B_1}{B_1 + B_2}, \tag{4.14}$$

where E_α and $B_{\alpha,o}$ are defined as before. The calculated value $E_{rec,1} = 8.2 \times 10^{-5}$ is within a factor of 2.5 of the measured value of $E_h = 2 \times 10^{-4}$ from Fig. 4.15(b). We can also evaluate the reconnection electric field from *Cassak and Shay* (2007) as

$$E_{rec,2} \sim \left(\frac{B_1 B_2}{B_1 + B_2} \right) v_{out} \frac{2\delta}{L}, \tag{4.15}$$

where v_{out} is the flow velocity downstream from the reconnection site. Using the measured value of v_{out}, we get $E_{rec,2} \sim 6.8 \times 10^{-5}$, which is within a factor of 4 of $E_{rec,1}$ and E_h. The disparity between calculated and measured values may be due to uncertainties in the measured data and also numerous effects not included in the scaling arguments, such as guide-field effects and curved magnetic geometry.

4.3.3 Two-Fluid Reconnection Signatures

4.3.3.1 Separation of Two-Fluid Scales

Due to the disparity between the ion and electron masses, where m_e is set to zero for the two-fluid simulation used here and M_i is scaled by setting d_b, there should be a separation of the scales over which the ion and electron dynamics decouple. Shown in Fig. 4.17 are the (a) ion and (b) electron velocities, where $\mathbf{v_e} = \mathbf{v_i} - (d_b/ne)\mathbf{J}$ in the reconnection plane. The maximum electron outflow velocity is larger than that of the ions by over a factor of 2, which is consistent with two-fluid and PIC slab reconnection studies, where the electron flow eclipses the ion flow in the reconnection exhausts [e.g. *Shay et al.* (1998)]. Furthermore, the electron outflows are noticeably thinner than those of the ion outflows, consistent with the two-scale structure due to the inclusion of the Hall term in the generalized Ohm's law. While hard to determine from the figure, the maximum electron velocity is peaked closer to

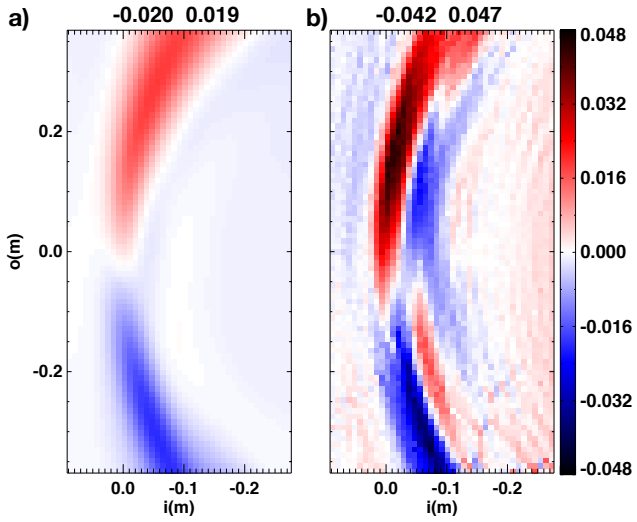

Figure 4.17: (a) Ion and (b) electron flows in the $\hat{o}$ direction in the reconnection plane located on the inboard side of the tokamak. The maximum electron flows are a factor of two larger than the ion flows and are peaked closer to the reconnection site. Additionally, the dominant electron flow is in the electron diamagnetic direction, and the flow is also in this direction at the reconnection site.

the reconnection site than the maximum ion velocity, also consistent with known properties of collisionless reconnection (*Shay et al.*, 1998). These results suggest that two-fluid physics is playing a role in these simulations as is expected, but has not previously been diagnosed in 3D toroidal simulations.

A particularly interesting observation is that both the ion and electron flows are in the direction of v_{*e} at the reconnection site, which is consistent with the 2D slab simulations shown in the previous chapter. This suggests that electron diamagnetic effects are playing a role in the local flow dynamics at the reconnection site.

4.3.3.2 Helical Magnetic Field Quadrupole

As discussed in Sec. 2.3, an important signature in collisionless reconnection is the existence of a quadrupole in the out-of-plane magnetic field. Due to the Hall effect, where the ion and electron physics decouple, the magnetic field is convected with the electron flow that

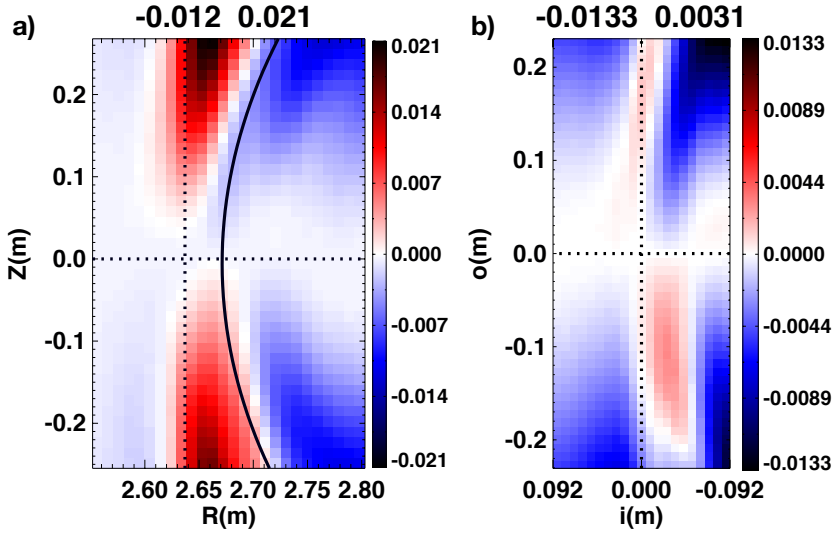

Figure 4.18: (a) Toroidal magnetic field perturbation $\tilde{B}_\phi$ in the poloidal plane with the profile at the midplane subtracted out of every horizontal slice, which leaves a dipolar structure. (b) Helical magnetic field perturbation $\tilde{B}_h$ in the reconnection plane with the profile through $o = 0$ subtracted out, which leaves a quadrupolar structure that has polarity consistent with collisionless reconnection due to the Hall term.

has a strong out-of-plane component due to its contribution to the reconnection current sheet. Recalling Fig. 2.4, as this electron flow convects the X-type magnetic configuration, it drags the field out-of-the plane, forming a quadrupolar structure in the out-of-plane field. As was discussed in Ch. 2, this has been observed experimentally in dedicated reconnection experiments, but the 3D field structure and small reconnection scales in a tokamak makes viewing this structure prohibitively difficult. Furthermore, to the best of our knowledge, it has not been identified in fully 3D toroidal simulations either.

In Fig. 4.18(a), we first show the toroidal magnetic field $\tilde{B}_\phi$ in the poloidal plane at the inboard side of the torus, the typical plane where reconnection has been studied, where we have subtracted the profile of B_ϕ at the midplane form every slice of B_ϕ to get the difference from the background profile. The dotted lines mark axes through the location of the reconnection site as determined from a Poincaré plot, and the solid line shows the calculated $q = 1$ surface from averaging over the magnetic field in the toroidal and poloidal

directions, revealing the latter technique's lack of accuracy as discussed in Sec. 4.3.1. From this figure, it is evident that there is no quadrupolar field signature in $\tilde{B}_\phi$ when viewed from the poloidal plane.

However, by sampling the data in the reconnection plane, we find a quadrupolar magnetic field signature in the helical magnetic field B_h as shown in Fig. 4.18(b). Similar to how the data is processed in (a), the profile of B_h through the reconnection site at $o = 0$ is subtracted out from each horizontal slice of B_h, leaving only the perturbed helical field $\tilde{B}_h$. With the polarity of the in-plane magnetic fields shown in Fig. 4.16, the polarity of the quadrupole out-of-plane field is consistent with that of the expected Hall magnetic field.

Because the helical (guide) field is strong compared to the relatively weak reconnecting field, with a ratio of $B_o/B_h \sim .039/1.23 = 3.2\%$, it is expected that the helical quadrupole field would be accompanied by a quadrupole gas pressure profile, as discussed in Sec. 2.4.1 in order to maintain total pressure balance. However, we find no gas pressure quadrupole in the reconnection plane for this two-fluid simulation. Additionally, the scaling of the ratio of the quadrupolar field to the reconnecting field departs from predictions by *Rogers and Denton* (2003), where $\tilde{B}_h \sim B_o$. We hypothesize that the curved geometry of the toroidal system and extremely large B_h/B_o dictates that additional physics due to magnetic field bending be kept in the scaling relations, but we leave this analysis for a future study. In summary, we have shown evidence local to the reconnection site demonstrating that Hall reconnection takes place.

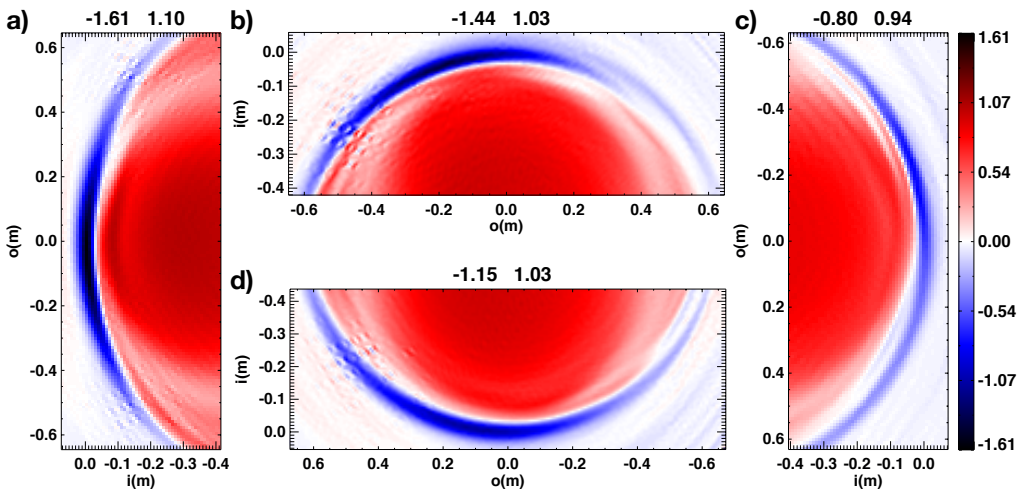

Figure 4.19: Views of the helical reconnection current density J_h in the reconnection plane at different toroidal angles corresponding to where the reconnection site is at the (a) inboard, (b) top, (c) outboard, and (d) bottom of the torus. The maximum magnitude of the reconnection current is on the inboard side, where the toroidal field is the strongest. Note also that δ/L is greater towards the inboard side, and lower towards the outboard side.

4.4 Toroidal Dependence

Thus far, the discussion has been limited to the reconnection site located on the inboard side of the torus. In this section we explore how reconnection changes for different toroidal angles, where the reconnection site is located at different poloidal locations. Because the threshold condition for incomplete reconnection is concerned with parameters local to the reconnection site, it is important to understand how reconnection behaves throughout the tokamak.

4.4.1 Toroidal Variation of Collisionless Reconnection

We begin our discussion in this section by looking at the reconnection current sheet of J_h at different toroidal angles. In Fig. 4.19, J_h is shown where the reconnection site is on the (a) inboard, (b) top, (c) outboard, and (d) bottom of the torus as determined from Poincaré

plots. The principal feature of Fig. 4.19 is that the maximum J_h in the current sheets at different toroidal angles is greater on the inboard side, and is smaller on the outboard side. Since the out-of-plane current is a reflection of the in-plane magnetic field shear and the width of the current sheet is set by the reconnection physics, on the inboard where the toroidal magnetic field is larger, we would expect the current to be larger, consistent with our simulations.

We have listed measured parameters associated with reconnection in Table 4.2. Using the methodology in Sec. 4.3.2.1 for finding upstream values, we find the reconnecting magnetic fields in the inflows of the core $B_{o,core}$ and the edge $B_{o,edge}$.Since the toroidal field varies as $B_\phi \sim 1/R$, the reconnecting fields are larger on the inboard side, consistent with the larger current on the inboard side. We also measure the density n at the X-line, and the average of the maximum downstream ion $v_{out,ave}$ and electron $v_{e,ave}$ flows in the reconnection exhausts. Consistent with the reconnection outflows scaling with the Alfvén speed, which scales as $\sim n^{-1/2}$, the average ion and electron flows are the smallest on the inboard side where the density is largest. The length of the reconnection current sheet $2L$ is found by locating where J_h falls to half its maximum along both outflow directions. We attribute the toroidal variation in the length of the current sheet to toroidal curvature. By looking at Fig. 4.1, for a helical field line with a circular cross-section, the path length from the top to the bottom on the inboard side is shorter than the path length connecting the top and bottom on the outboard side because B is stronger on the inboard side. The width of the reconnection current sheet $2\delta = \delta_1 + \delta_2$ is also listed, where the thicknesses are found by measuring from the X-line to the location where the upstream magnetic fields are found.

While the width of the current sheet varies slightly with toroidal (poloidal) location, the length of the current sheet increases towards the outboard side due to the toroidal curvature,

Table 4.2: Measured characteristic values of two-fluid reconnection, where the reconnection site is located at different toroidal (and poloidal) angles. Tabulated values are the reconnecting magnetic field in the inflows toward the core and edge $B_{o,core}$ and $B_{o,edge}$, the density n at the X-line, the average ion outflow velocity $v_{out,ave}$, the average electron outflow velocity $v_{e,ave}$, the total length of the current sheet $2L$, and the total thickness of the current sheet $2\delta = \delta_1 + \delta_2$.

Location	$B_{o,core}$	$B_{o,edge}$	n	$v_{out,ave}$	$v_{e,ave}$	$2L$	$\delta_1 + \delta_2$
Outboard	0.02	0.014	0.83	0.028	0.063	0.45	0.051
Top	0.044	0.01	0.91	0.025	0.059	0.28	0.048
Inboard	0.034	0.044	1.1	0.021	0.047	0.29	0.049
Bottom	0.024	0.038	0.95	0.024	0.051	0.35	0.057

Table 4.3: Aspect ratio of the reconnection site δ/L, measured E_h and calculated $E_{rec,1}$ and $E_{rec,2}$ values of the reconnection rate, where the reconnection site is located at different toroidal (and poloidal) angles. $E_{rec,1}$ is calculated using Eq. 4.14 and $E_{rec,2}$ is calculated using Eq. 4.15.

Location	δ/L	E_h	$E_{rec,1}$	$E_{rec,2}$
Outboard	0.11	7.3×10^{-5}	2.6×10^{-5}	2.6×10^{-5}
Top	0.17	1.0×10^{-4}	2.3×10^{-5}	3.4×10^{-5}
Inboard	0.17	2.0×10^{-4}	8.2×10^{-5}	6.8×10^{-5}
Bottom	0.16	1.4×10^{-4}	6.5×10^{-5}	5.7×10^{-5}

decreasing δ/L as shown in Table 4.3. Recalling Eq. 2.1, this aspect ratio is indicative of the rate of reconnection, implying that reconnection proceeds more slowly towards the outboard side of the tokamak. The decrease in the rate of reconnection toward the outboard side is also visible in the measured E_h helical electric field and the reconnection electric fields $E_{rec,1}$ and $E_{rec,2}$ calculated from Eq. 4.14 and Eq. 4.15, respectively, where the measured electric fields are generally larger on the inboard and smaller on the outboard.

We notice in Fig. 4.19, that while the inboard and outboard current sheets are mostly centered around the midplane, the top and bottom current sheets are shifted towards the inboard side of the torus. A similar asymmetry is also seen in Fig. 4.20 of the ion outflows on the (a) top and (b) bottom reconnection sites, where the stronger outflow jets are toward the outboard side for both sites. This asymmetry in the outflows can be explained by how the toroidal magnetic field varies in the major radial direction, decreasing as $\sim 1/R$. At

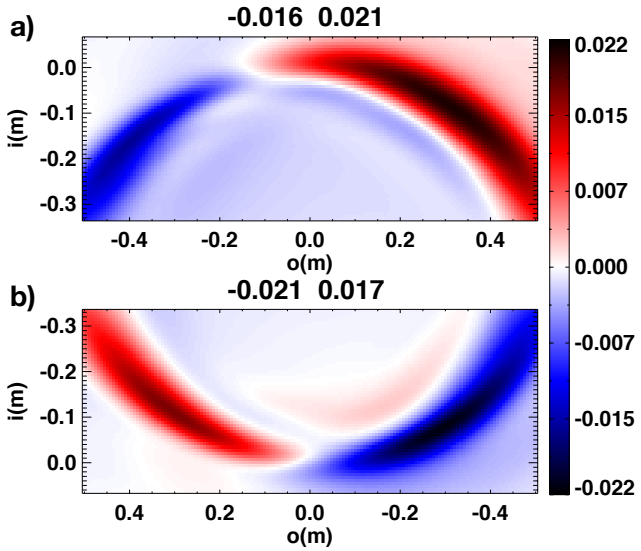

Figure 4.20: Ion flows in the $\hat{o}$ direction where the reconnection site is at the (a) top and (b) bottom of the torus. The outflows are asymmetric due to the magnetic pressure gradient in the major radial direction due to the varying toroidal magnetic field, consistent with *Murphy et al.* (2010) that shows the outflow with a lower pressure has a faster flow.

the inboard and outboard reconnection sites, the toroidal magnetic field changes through the inflow direction, contributing to the helical current, but at the top and bottom sites the toroidal magnetic field changes through the outflow direction. *Murphy et al.* (2010) showed that if there is a gas pressure gradient in the outflow direction, there is an outflow asymmetry with the faster outflow where the gas pressure is less. Similarly here, there is a magnetic field pressure gradient towards the outboard side of the torus, and for the top and bottom sites this gradient is in the outflow direction, consistent with the polarity of the asymmetric outflows.

Interestingly enough, there is also an asymmetry of the electron temperature for the top and bottom reconnection sites, as seen in Fig. 4.21. The temperature in the outflow toward the outboard side is greater than that in the outflow toward the inboard side, giving the appearance that the high temperature core is offset toward the outboard side. This observation is consistent with the experimental result of *Yamaguchi et al.* (2004) shown in

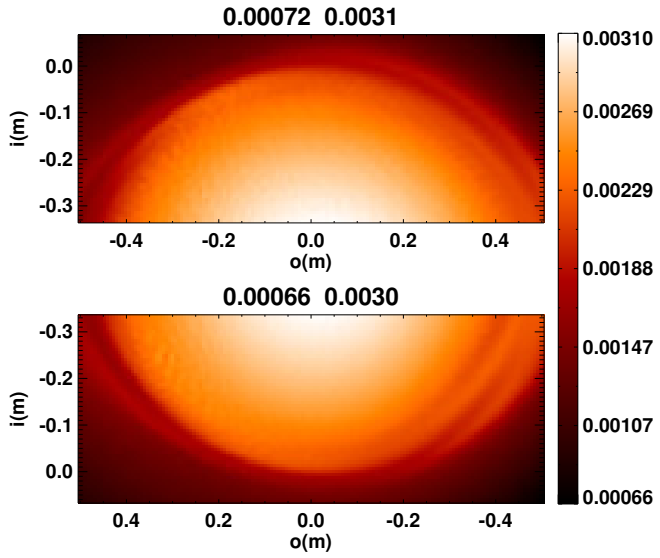

Figure 4.21: Electron temperature sampled in the reconnection plane where the reconnection site is at the (a) top and (b) bottom of the torus. Consistent with the results of *Yamaguchi et al.* (2004), the hot core bulges toward the outboard side of the torus.

Fig. 1.11, where the hot core was shifted toward the outboard side when the sawtooth mode was on the top and bottom sides of the tokamak.

The last feature we discuss in this section is the separation of the ion and electron flows in the $\hat{o}$ direction, shown in Fig. 4.22 for the outboard side of the device. Comparing this to Fig. 4.17, which shows the same data at the inboard side, there are many similarities. The electron flow is significantly larger in magnitude than the ion flow, the ion outflow jets are thicker than the electron jets, and the ion and electron flows are in the direction of v_{*e} at the reconnection site. However, there are differences as well. The magnitudes of both the ion and electron flows increase towards the outboard side, as recorded in Table 4.2, and the locations of the maximum flow are located further downstream on the outboard side, consistent with the elongation of the reconnection current sheet.

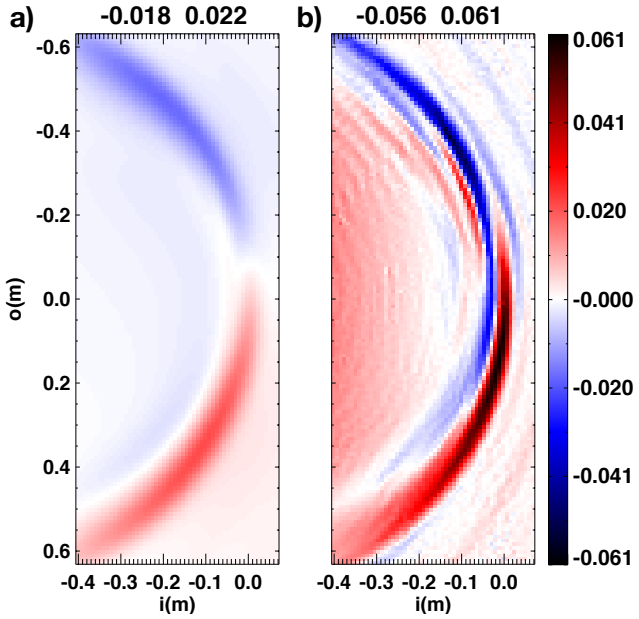

Figure 4.22: (a) Ion and (b) electron flows in the $\hat{o}$ direction of the reconnection plane for the two-fluid simulation, where the reconnection site is located on the outboard side of the helical mode, as compared to the inboard side in Fig. 4.17. Note that the maximum electron flows are greater in magnitude, and both the ion and electron flow maxima are located further downstream from the reconnection site on the outboard side.

Table 4.4: Parameters determining the electron diamagnetic effects evaluated at the reconnection site for different toroidal (and poloidal) locations. Tabulated values are the helical magnetic field B_h, the electron pressure gradient ∇p_e, the density n, and the electron diamagnetic drift speed v_{*e}.

Location	B_h	∇p_e	n	v_{*e}
Outboard	0.86	-0.027	0.83	0.0040
Top	0.99	-.022	0.91	0.0026
Inboard	1.23	-0.033	1.1	0.0027
Bottom	0.99	-0.025	0.95	0.0028

4.4.2 Diamagnetic Effects

We end the chapter by commenting on how the electron diamagnetic effects vary at the reconnection sites at different toroidal angles in order to understand how the incomplete reconnection condition varies around a tokamak. Table 4.4 lists values of parameters measured locally at the reconnection sites at the outboard, top, inboard, and bottom of the torus. As expected, the helical magnetic field is stronger on the inboard than the outboard side, and as we commented on in the last section, so is the density. The electron pressure gradient at the reconnection site is largest on the inboard and outboard sides, and slightly less on the top and bottom. Combining the measured values, v_{*e} is basically constant over the top, inboard, and bottom sides, while it is increased on the outboard.

While the electron diamagnetic flows are larger on the outboard side of the torus due to the decreased toroidal field and density, the electron flows due to reconnection are also faster there as well, consistent with the observation of complete reconnection. Compared to Eq. 3.5 for the suppression of reconnection, even at the outboard where v_{*e} is greatest, the electron outflows from the reconnection site are still over a factor of 20 larger for this simulation. In future simulations aimed to observe incomplete reconnection, we will need to explore a parameter space that allows the electron diamagnetic effects to increase more as reconnection evolves. This may be accomplished by changing the geometry of the equilibrium, lowering the density as was commented upon in Sec. 4.2.2, or lowering d_b to narrow the two-fluid current sheet and substantially increase ∇p_e during the reconnection phase.

4.5 Conclusions

Because of the breadth of topics covered in this chapter, it is prudent to summarize the results of the toroidal simulations. By utilizing the extended-MHD code M3D-C^1, we have undertaken a comparison of the tearing/reconnection of the $(m, m) = (1, 1)$ helical mode between resistive-MHD and two-fluid simulations. Compared to the resistive-MHD model, we find that the growth of the kinetic energy in different toroidal modes for the two-fluid reconnection process is substantially greater and exhibits a nonlinear acceleration, which is more closely in line with experimental results. Additionally, for the two-fluid model, we showed the first observation of early nonlinear stabilization of tearing by electron diamagnetic effects in a toroidal geometry. When the equilibrium electron pressure gradient was then lowered, tearing and eventually reconnection proceeded completely.

By sampling simulation data in the poloidal plane, the typical plane in which sawteeth are studied, we confirmed the known result that reconnection processes the hot core differently in the resistive and two-fluid models, being faster in the latter. The toroidal rotation due to the externally-applied neutral beam causes poloidal rotation of the helical mode during the longer timescale of the resistive simulation consistent with experimental results (*Yamaguchi et al.*, 2004). During the tearing phase in the two-fluid simulations, the tearing site drifted in the direction of v_{*e}, which shows that the magnetic field configuration drifts with the electron diamagnetic flow rather than with the ion flow. Furthermore, this poloidal drift is consistent with the initial findings of *von Goeler et al.* (1974), which reported that the sawtooth mode propagates in the v_{*e} direction. It was also shown that the reconnection current was directed opposite to the plasma current I_p for the chosen equilibrium, flowing in the negative helical direction, which causes the $q = 1$ surface to expand radially outward

and has the potential to trigger disruptive behavior. Also in the poloidal plane, we saw how reconnection causes the electron pressure gradient to increase, which is consistent with the results of *Chapman et al.* (2010) and a central part of our incomplete reconnection model in Ch. 3.

By sampling the two-fluid simulation data in the plane perpendicular to the local magnetic field at the reconnection site, we have shown the first observation of the quadrupole out-of-plane magnetic field appearing during sawtooth reconnection with the Hall term. This is an important result because it shows that the inclusion of the Hall term leads to fast reconnection in sawteeth, leading to crash times that are more in line with experimental results as compared to simulations without Hall physics. We compared the relative rates of resistive and two-fluid reconnection, where the reconnection electric field was a factor of 40 larger in the latter. It was seen that the reconnecting fields and inflows were asymmetric leading to a drift of the reconnection site towards the edge of the torus.

We also explored how reconnection as viewed in the proper plane varies toroidally, where reconnection was stronger on the inboard even though the outflow speeds of the ions and electrons were faster on the outboard side. We posit that toroidal curvature affected the aspect ratio of the reconnection geometry, elongating the reconnection site on the outboard side, while the varying toroidal magnetic field causes an outflow asymmetry on the top and bottom of the torus. Because these asymmetries and current sheet variations alter the rate of reconnection, this is important for understanding how the reconnection mode evolves locally throughout the tokamak. Due to the decrease of the helical field and density with major radius, the electron diamagnetic effects were stronger on the outboard side. However, the reconnection flows were also stronger there, leading to dominance of the reconnection physics over diamagnetic effects throughout the tokamak and complete reconnection. To test our

incomplete reconnection model from Ch. 3, additional simulations will need to be performed where the reconnection physics and diamagnetic physics are comparable during the sawtooth crash phase.

Chapter 5

Conclusions and Future Work

5.1 Summary of Results

In summary, the sawtooth crash is an internal disruption in tokamaks where the magnetic field of the $(m, n) = (1, 1)$ helical mode reconnects at the $q = 1$ rational surface. This disruption allows for increased transport of the hot, core plasma to the edge of the tokamak. While many experimental results and numerical simulations have provided data to explain sawteeth, many questions still exist. Foremost is the appearance of incomplete reconnection, where the sawtooth crash phase ends before all available core magnetic field is reconnected. Multiple models exist to explain these observations, but none have been unequivocally proven using simulations or data available from experiments.

In this dissertation, we suggest that reconnection self-consistently increases diamagnetic effects that can cause the suppression of reconnection, a model that would explain incomplete reconnection in sawteeth. We tested this model with 2D slab geometry, two-fluid simulations, and utilized 3D toroidal geometry, two-fluid simulations to diagnose reconnection and diamagnetic physics during the sawtooth crash phase and confirm some key aspects of the

model.

5.1.1 A New Model for Incomplete Reconnection

Building on the previous work of the stabilizing effect of diamagnetic physics on magnetic reconnection, we have proposed a new model for incomplete reconnection in sawteeth. Since reconnection at the $q = 1$ surface convects in hot plasma from the core and cold plasma from the edge, the pressure gradient across the $q = 1$ surface will increase self-consistently as reconnection proceeds. If the pressure gradient is increased to a sufficient level, the associated diamagnetic effects suppress reconnection. We tested the basic physics of this proposed model with 2D slab, two-fluid numerical simulations. A simulation including an external pressure gradient showed that reconnection was indeed suppressed as the system evolved, while a simulation without an external pressure gradient proceeded until all magnetic flux was processed. We also showed that the model was consistent with experimental data from MAST. The model is quantified by the threshold condition given in Eq. 3.5, which states that if the electron diamagnetic flow at the reconnection site ever eclipses either electron reconnection outflow, reconnection ceases.

5.1.2 3D Toroidal Simulations of Sawteeth

We then extended our analysis of incomplete reconnection in sawteeth by utilizing the extended-MHD code M3D-C^1 which has a 3D toroidal computational domain. We began by comparing tearing/reconnection of the $(m, n) = (1, 1)$ helical mode between resistive-MHD and two-fluid simulations. We found that compared to simulations using the resistive-MHD model, in two-fluid simulations the growth of the kinetic energy was more in line with experimental observations. To our knowledge, this is the first time this has been done in

3D toroidal simulations. We also saw that for a two-fluid simulation with a relatively high central pressure, that the tearing/reconnection mode was suppressed during the early non-linear phase. However, when we lowered the central pressure, which lowered the pressure gradient at the $q = 1$ surface, reconnection proceeded, and completely processed the core plasma. Thus, for the simulation parameters tested, we observed either complete suppression or complete reconnection, again the first time this has been observed in simulations.

5.1.2.1 Reconnection and Diamagnetic Physics in the Poloidal Plane

To make contact with previous studies of sawteeth in a 3D toroidal geometry, we analyzed data sampled in the poloidal plane defined by a constant toroidal angle. By looking at the evolution of the electron temperature, we confirmed the known result that reconnection processes the core more rapidly in the two-fluid case than the resistive case. During the longer timescales of the resistive simulation, toroidal rotation due to the applied torque of the neutral beam caused poloidal rotation of the helical mode, which is consistent with experimental results. Also in line with experimental results, the tearing/reconnection site was observed to drift poloidally with the electron diamagnetic flow v_{*e} in the two-fluid simulation. By looking at profiles of the electron pressure taken through the midplane for toroidal angles where the reconnection site was located on the inboard side, we observed the increase in the electron pressure gradient at the $q = 1$ surface, consistent with a prediction of our new model for incomplete reconnection and experimental results.

5.1.2.2 Local Signatures in Reconnection Plane

After looking at data sampled in the poloidal plane, we outlined a new method for obtaining the plane of reconnection in 3D toroidal simulations, where the plane is perpendicular to

the local magnetic field at the reconnection site as opposed to a poloidal plane. Looking at data sampled in the appropriate plane for reconnection, we compared the reconnection sites on the inboard side of the torus between resistive-MHD and two-fluid simulations. We found that the current sheet has a larger δ/L in the latter, consistent with collisionless reconnection, while the current sheet in the former was elongated, consistent with Sweet-Parker reconnection. We quantified the contributions to the reconnection electric field, showing that resistivity balanced it at the X-line in resistive-MHD, but not in the two-fluid case. The two-fluid simulation had a reconnection electric field a factor of 40 times greater than the resistive simulation. Additionally, both reconnection sites were asymmetric in the inflow direction, which was compatible with the observation that the $q = 1$ surface expanded toward the edge of the tokamak in both simulations. When comparing the measured value of the reconnection rate for the two-fluid case to analytical predictions based on fields and velocities in the inflows, we found they scaled reasonably well, but there were discrepancies. We also observed that the ion and electron flows exhibited a two scale structure, which were consistent with the observation of an out-of-plane quadrupolar field due to the inclusion of the Hall physics. This was the first observation of this signature in 3D toroidal simulations, and shows that the inclusion of the Hall term in the generalized Ohm's law leads to fast crash times that are more in line with experimental results than resistive-MHD simulations.

5.1.2.3 Toroidal Variation of Reconnection and Diamagnetic Physics

Next, we explored how two-fluid reconnection as viewed in the proper plane varies toroidally. We found that the reconnection rate was larger on the inboard side, while the ion and electron outflows were larger on the outboard side. We proposed that due to the toroidal magnetic field scaling like $B_\phi \sim 1/R$, the reconnection fields are weaker on the outboard side, which

lowered the local reconnection rate. Because the threshold condition proposed to explain incomplete reconnection depends on local reconnection parameters, understanding how reconnection varies through the toroidal direction is significant. We observed that since the toroidal magnetic field decreases with increasing major radius, there is an asymmetry in the reconnection outflow speeds at the top and bottom sides of the tokamak. Furthermore, the decrease in toroidal magnetic field leads to a decrease in the helical magnetic field with major radius, and when coupled with the observation of a decrease in the density at the reconnection site with major radius, leads to an increase in the electron diamagnetic drift speed on the outboard side of the torus. However, since the reconnection flows were also larger there, the incomplete reconnection threshold condition was not satisfied, and reconnection was complete for these simulation parameters.

5.2 Future Work

Throughout the presented work, we commented on additional lines of study that would further test our predictions and develop important concepts involved in the incomplete reconnection process. We conclude this dissertation by gathering them here.

5.2.1 Analytical Predictions

Analytical expressions in *Rogers and Denton* (2003) give predictions for the magnitudes of characteristic values associated with the Hall magnetic fields when there is a magnetic guide field. However, our results did not agree with these predictions. In the 3D toroidal geometry simulations, we did not observe a quadrupole perturbation to the electron pressure. Future work to address these observations should include a detailed analytical treatment including

curved geometry, extreme guide-field, and drift effects. Also in 3D toroidal simulations, we showed how the rates of reconnection consistent with the out-of-plane electric field E_h scaled reasonably well with analytical predictions conceived for 2D slab configurations. However, there were differences, so a better predictive model for the reconnection rate in sawteeth would require a more thorough analysis of the local reconnection site, including curved geometry, magnetic guide field, and a drifting reference frame.

5.2.2 2D Slab Geometry Simulations

For the 2D slab geometry simulations where reconnection was suppressed due to the increase in local diamagnetic effects, further simulation work should be carried out that includes additional extended-MHD effects such as ion diamagnetic effects and higher thermal conductivity $\chi_{||}$. In the simulations presented, we observed a secondary instability, which suggested a Kelvin-Helmholtz or drift instability arose in the reconnection outflows due to the interaction of the external pressure gradient. While gyro-kinetic simulations have been performed over a parameter space where pressure gradients were located across the reconnection site, a study employing an equilibrium with an upstream pressure gradient would be useful for investigating the role these secondary instabilities play.

For the two-fluid simulations in both the 2D slab and 3D toroidal geometries, we observed that the X-line drifted with a speed that was approximately 1/5 of the electron diamagnetic drift speed v_{*e}, while PIC simulations showed a $1:1$ correspondence. Because the PIC simulations started from an equilibrium with a pressure gradient initially across the reconnection site, a steady-state was not reached before the influence of the diamagnetic effects. By running PIC simulations with the pressure gradient initially upstream, it would be possible investigate the additional physics controlling the drift speed of the reconnection site.

5.2.3 3D Toroidal Geometry Simulations

There are also several places where the work done in our 3D toroidal simulations should be extended. Since the amount of resources needed to perform two-fluid nonlinear simulations is substantial, our ability to undertake a convergence study of the spatial resolution was limited, so doing more to test the numerics, including increasing the number of toroidal planes would be important. The model equations should be augmented to included multiple ion species to better connect to experiments. The two-fluid simulation for the higher central pressure, where the tearing mode was suppressed in the early nonlinear phase, should also be extended in time to ensure the suppression is robust over longer times.

While 2D simulations in a slab geometry have shown that collisionless reconnection has a reconnection rate that is insensitive to the dissipative mechanism breaking magnetic fields at the X-line, testing how the present results in 3D toroidal, two-fluid simulations are affected when the dissipation mechanism is altered is necessary. By using an explicit, high-order, numerical diffusion in the evolution equations, this study could be undertaken with a controlled approach.

Since all the simulations covered in this dissertation were proof-of-principle, it is essential that the model is assessed with parameters of specific devices. Also, we expect that for equilibria where the value of the central safety factor q_0 is closer to unity, which are more indicative of experimental devices, the reconnection current would interact differently with the confining plasma current than in the present simulations. By choosing equilibria with lower values of density, we can explore conditions where diamagnetic effects play a larger relative role during the reconnection phase in order to evaluate our new model for incomplete reconnection.

5.2.4 Application to Experiments

The crash time of sawteeth, including the effects of incomplete reconnection, is important for fast-ion transport by sawteeth. The magnitude of the transport depends crucially on the relative magnitude of the sawtooth crash time and the characteristic times for energetic-ion orbits (*Muscatello et al.*, 2012). Accurate crash times are needed to provide reasonable predictions of the effect of large sawteeth on alpha-particle confinement in the ITER baseline scenarios.

The dynamics of sawteeth are also important for the seeding of disruptions through seeding NTMs. NTMs require an initial perturbation to being growing, and sawteeth can couple their energy through the $n = 1$ or $n = 2$ toroidal mode to create seed islands for $(m, n) = (2, 1)$ and $(3, 2)$ NTMs. Understanding the rate at which the magnetic island due to reconnection grows, and how large it grows compared to the location of the $q = 1$ surface relative to higher-order rational surfaces determines the strength of this coupling. By understanding how diamagnetic effects change the reconnection rate during the crash phase and how the reconnection current relative to the core plasma current convects the $q = 1$ surface, our work has the potential to describe how sawteeth seed NTMs.

The new model for incomplete reconnection may be useful for low-dimensional transport modeling codes that are used to predict the extent of plasma transport in tokamak discharges. They currently use an ad hoc description of incomplete reconnection, so the results give an avenue for a first-principles approach. Since the model only depends on the local electron diamagnetic effects and reconnection physics, it is machine independent, and should apply both to existing tokamaks and future ones such as ITER.

Bibliography

Appel, L. C., T. Fülöp, M. J. Hole, H. M. Smith, S. D. Pinches, R. G. L. Vann, and the MAST team (2008), Compressional alfvén eigenmodes on MAST, *Plasma Phys. Control. Fusion*, *50*, 115011.

Axford, W. I. (1984), Magnetic field reconnection, in *Magnetic Reconnection in Space and Laboratory Plasmas*, edited by J. Edward W. Hones, Geophysical Monograph 30, pp. 1–8, American Geophysical Union.

Aydemir, A. Y. (1992), Nonlinear studies of $m = 1$ modes in high-temperature plasmas, *Phys. Fluids B*, *4*(11), 3469–3472.

Barabaschi, P. (2015), Understanding fusion: What is fusion?, http://fusionforenergy.europa.eu.

Basu, B., and B. Coppi (1981), Theory of $m = 1$ modes in collisionless plasmas, *Phys. Fluids*, *24*, 465.

Bateman, G. (1978), *MHD Instabilities*, The MIT Press.

Bateman, G., C. N. Nguyen, A. H. Kritz, and F. Porcelli (2006), Testing a model for triggering sawtooth oscillations in tokamaks, *Phys. Plasmas*, *13*, 072505.

Birn, J., J. F. Drake, M. A. Shay, B. N. Rogers, R. E. Denton, M. Hesse, M. Kuznetsova, Z. W. Ma, A. Bhattacharjee, A. Otto, and P. L. Pritchett (2001), GEM magnetic reconnection challenge, *J. Geophys. Res.*, *106*, 3715.

Biskamp, D. (1981), Nonlinear theory of the $m = 1$ mode in hot tokamak plasmas, *Phys. Rev. Lett.*, *46*, 1522.

Biskamp, D. (1986), Magnetic reconnection via current sheets, *Phys. Fluids*, *29*, 1520.

Biskamp, D. (2000), *Magnetic Reconnection in Plasmas*, Cambridge University Press, Cambridge, UK.

Biskamp, D., and T. Sato (1997), Partial reconnection in the nonlinear internal kink mode, *Phys. Plasmas*, *4*, 1326.

Biskamp, D., E. Schwarz, and J. F. Drake (1997), Two-fluid theory of collisionless magnetic reconnection, *Phys. Plasmas*, *4*, 1002.

Borgogno, D., D. Grasso, F. Porcelli, F. Califano, F. Pegoraro, and D. Farina (2005), Aspects of three-dimensional magnetic reconnection, *Phys. Plasmas*, *12*, 032309.

Braginskii, S. I. (1965), Transport processes in a plasma, *Reviews of Plasma Physics*, *1*, 205.

Breslau, J., N. Ferraro, and S. Jardin (2009), Some properties of the M3D-C1 form of the three-dimensional magnetohydrodynamics equations, *Physics of Plasmas*, *16*, 092503.

Breslau, J. A., S. C. Jardin, and W. Park (2007), Three-dimensional modeling of the sawtooth instability in a small tokamak, *Phys. Plasmas*, *14*, 056105.

Bussac, M. N., R. Pellat, D. Edery, and J. L. Soule (1975), Internal kink modes in toroidal plasmas with circular cross sections, *Phys. Rev. Lett.*, *35*, 1638–1641.

Caldas, I. L., R. L. Viana, M. S. T. Araujo, A. Vannucci, E. C. d. Silva, K. Ullmann, and M. V. A. P. Heller (2002), Control of chaotic magnetic fields in tokamaks, *Brazilian Journal of Physics*, *32*, 980 – 1004.

Campbell, D. J., P. A. Duperrex, A. W. Edwards, R. D. Gill, C. W. Gowers, R. Granetz, M. Hugon, P. J. Lomas, N. Lopes-Cardozo, M. Malacarne, M. F. Nave, D. C. Robinson, F. C. Schüller, P. Smeulders, J. A. Snipes, P. E. Stott, G. Tonetti, B. J. Tubbing, A. Weller, and J. A. Wesson (1986), Sawteeth and disruptions in JET, in *Plasma Physics and Controlled Nuclear Fusion Research*, vol. 1, edited by K. International Conference, pp. 433–445, IAEA, Wienna, 1987.

Campbell, D. J., D. F. H. Start, J. A. Wesson, D. V. Bartlett, V. P. Bhatnagar, M. Bures, J. G. Cordey, G. A. Cottrell, P. A. Dupperex, A. W. Edwards, C. D. Challis, C. Gormezano, C. W. Gowers, R. S. Granetz, J. H. Hammen, T. Hellsten, J. Jacquinot, E. Lazzaro, P. J. Lomas, N. L. Cardozo, P. Mantica, J. A. Snipes, D. Stork, P. E. Stott, P. R. Thomas, E. Thompson, K. Thomsen, and G. Tonetti (1988), Stabilization of sawteeth with additional heating in the JET tokamak, *Phys. Rev. Lett.*, *60*, 2148.

Cassak, P. A. (2006), Catastrophe model for the onset of fast magnetic reconnection, Ph.D. thesis, University of Maryland, www.physics.udel.edu/˜pcassak/cassakthesis.pdf.

Cassak, P. A. (2011), Theory and simulations of the scaling of magnetic reconnection with symmetric shear flow, *Phys. Plasmas*, *18*, 072106.

Cassak, P. A., and M. A. Shay (2007), Scaling of asymmetric magnetic reconnection: General theory and collisional simulations, *Phys. Plasmas*, *14*, 102114.

Cassak, P. A., and M. A. Shay (2008), Scaling of asymmetric Hall reconnection, *Geophys. Res. Lett.*, *35*, L19102.

Cassak, P. A., R. N. Baylor, R. L. Fermo, M. T. Beidler, M. A. Shay, M. Swisdak, J. F. Drake, and H. Karimabadi (2015), Fast magnetic reconnection due to anisotropic electron pressure, *Physics of Plasmas*, *22*(2), 020705.

Chang, Z., J. D. Callen, E. D. Frederickson, R. B. Budny, C. C. Hegna, K. M. Mcguire, M. C. Zarnstorff, and the TFTR group (1995), Observation of nonlinear neoclassical pressure-gradient-driven tearing modes in TFTR, *Phys. Rev. Lett.*, *74*, 1995.

Chapman, I. T. (2011a), Controlling sawtooth oscillations in tokamak plasmas, *Plasma Physics and Controlled Fusion*, *53*(1), 013001.

Chapman, I. T. (2011b), Private communication, Private Communication.

Chapman, I. T., R. Scannell, W. A. Cooper, J. P. Graves, R. J. Hastie, G. Naylor, and A. Zocco (2010), Magnetic reconnection triggering magnetohydrodynamic instabilities during a sawtooth crash in a tokamak plasma, *Phys. Rev. Lett.*, *105*, 255002.

Chapman, I. T., R. J. L. Haye, R. J. Buttery, W. W. Heidbrink, G. L. Jackson, C. M. Muscatello, C. C. Petty, R. I. Pinsker, B. J. Tobias, and F. Turco (2012), Sawtooth control using electron cyclotron current drive in ITER demonstration plasmas in DIII-D, *Nuclear Fusion*, *52*(6), 063006.

Chapman, I. T., V. Igochine, M. Maraschek, P. J. McCarthy, G. Tardini, the ASDEX Upgrade ECRH Group, and the ASDEX Upgrade Team (2013), Sawtooth control using electron cyclotron current drive in the presence of energetic particles in high performance ASDEX upgrade plasmas upgrade plasmas, *Plasma Phys. and Conrol. Fusion*, *55*, 065009.

Chen, F. F. (1974), *Introduction to Plasma Physics*, Plenum Press.

Chen, F. F. (2011), *An Indispensable Truth: How Fusion Power Can Save the Planet*, Springer.

Choudhuri, A. R. (1998), *The Physics of Fluids and Plasmas*, Cambridge University Press.

Coppi, B. (1965), Current-driven instabilities in configurations with sheared magnetic fields, *Phys. Fluids*, *8*, 2273.

Coppi, B., R. J. Hastie, S. Migliuolo, F. Pegoraro, and F. Porcelli (1988), Suppression of internal plasma oscillations by trapped high energy nuclei, *Phys. Lett. A*, *132*, 267.

Cowley, S. C., J. P. Jr., J. D. Callen, F. R. Chang-Díaz, T. Ditmire, W. Dorland, W. Gekelman, S. L. Girshick, D. Hammer, E. P. Ippen, M. J. Kushner, K. A. Lynch, J. E. Menard, L. Merminga, E. Quataert, T. J. Sommerer, C. M. Surko, and M. Tabak (2007), *Plasma Science: Advancing Knowledge in the National Interest*, The National Academies Press.

Denton, R., J. F. Drake, R. G. Kleva, and D. Boyd (1986), Skin currents and compound sawteeth in tokamaks, *Phys. Rev. Lett.*, *56*, 2477.

Drake, J. F., and M. A. Shay (2007), The fundamentals of collisionless reconnection, in *Reconnection of Magnetic Fields: Magnetohydrodynamics and Collisionless Theory and Observations*, edited by J. Birn and E. Priest, Cambridge University Press.

Drake, J. F., M. Swisdak, M. A. Shay, B. N. Rogers, A. Zeiler, and C. Cattell (2003), Formation of electron holes and particle energization during magnetic reconnection, *Science*, *299*, 873.

Drake, J. F., M. A. Shay, W. Thongthai, and M. Swisdak (2005), Production of energetic electrons during magnetic reconnection, *Phys. Rev. Lett.*, *94*, 095001.

Dubois, M. A., A. L. Pecquet, and C. Reverdin (1983), Internal disruptions in the TFR tokamak - a phenomenological analysis, *Nucl. Fusion*, *23*, 147.

Dungey, J. W. (1953), Conditions for the occurrence of electrical discharges in astrophysical systems, *Phil. Mag.*, *44*, 725.

Edwards, A. W., D. J. Campbell, W. W. Engelhardt, H. U. Farhbach, R. D. Gill, R. S. Granetz, S. Tsuji, B. J. D. Tubbing, A. Weller, J. Wesson, and D. Zasche (1986), Rapid collapse of a plasma sawtooth oscillation in the JET tokamak, *Phys. Rev. Lett.*, *57*, 210–213.

Egedal, J., W. Fox, N. Katz, M. Porkolab, K. Reim, and E. Zhang (2007), Laboratory observations of spontaneous magnetic reconnection, *Phys. Rev. Lett.*, *98*, 015,003.

Ferraro, N. M., and S. C. Jardin (2009), Calculations of two-fluid magnetohydrodynamic axisymmetric steady-states, *Journal of Computational Physics*, *228*(20), 7742–7770.

Forbes, T. G. (2007), *Classical Theory of Two-Dimensional Reconnection*, chap. 2, pp. 16–25, Cambridge University Press.

Freidberg, J. P. (1987), *Ideal Magnetohydrodynamics*, Springer.

Furth, H. P., J. Killeen, and M. N. Rosenbluth (1963), Finite-resistivity instabilities of a sheet pinch, *Phys. Fluids*, *6*(4), 459.

Galeev, A. A., and R. Z. Sagdeev (1984), *Handbook of Plasma Physics*, vol. 2, chap. 6.1, p. 271, North Holland Physics Publishing.

Gibbs, K. (2012), Binding energy per nucleon, http://www.schoolphysics.co.uk.

Grad, H., and H. Rubin (1958), Hydrodynamic equilibris and force-free fields, in *Proceedings of the 2nd UN Conference on the Peaceful Uses of Atomic Energy*, vol. 31, p. 190, IAEA.

Hender, T. C., J. C. Wesley, J. Bialek, A. Bondeson, A. H. Boozer, R. J. Buttery, A. Garofalo, T. P. Goodman, R. S. Granetz, Y. Gribov, O. Gruber, M. Gryaznevich, G. Giruzzi, S. G"unter, N. Hayashi, P. Helander, C. C. Hegna, D. F. Howell, D. A. Humphreys, G. T. A. Huysmans, A. W. Hyatt, A. Isayama, S. C. Jardin, Y. Kawano, A. Kellman, C. Kessel, H. R. Koslowski, R. J. L. Haye, E. Lazzaro, Y. Q. Liu, V. Lukash, J. Manickam, S. Medvedev, V. Mertens, S. V. Mirnov, Y. Nakamura, G. Navratil, M. Okabayashi, T. Ozeki, R. Paccagnella, G. Pautasso, F. Porcelli, V. D. Pustovitov, V. Riccardo, M. Sato, O. Sauter, M. J. Schaffer, M. Shimada, P. Sonato, E. J. Strait, M. Sugihara, M. Takechi, A. D. Turnbull, E. Westerhof, D. G. Whyte, R. Yoshino, H. Zohm, D. the ITPA MHD, and M. C. T. Group (2007), Chapter 3: MHD stability, operational limits and disruptions, *Nucl. Fusion*, *47*, S128.

Hesse, M., K. Schindler, J. Birn, and M. Kuznetsova (1999), The diffusion region in collisionless magnetic reconnection, *Phys. Plasmas*, *6*(5), 1781.

Hesse, M., M. Kuznetsova, and M. Hoshino (2002), The structure of the dissipation region for component reconnection: Particle simulations, *Geophys. Res. Lett.*, *29*, 1563.

Hesse, M., M. Kuznetsova, and J. Birn (2004), The role of electron heat flux in guide-field magnetic reconnection, *Phys. Plasmas*, *11*(12), 5387–5397.

Hesse, M., S. Zenitani, and A. Klimas (2008), The structure of the electron outflow jet in collisionless magnetic reconnection, *Physics of Plasmas*, *15*(11), 112102.

Holmes, J. A., B. A. Carreras, and L. A. Charlton (1989), Magnetohydrodynamic stability and nonlinear evolution of the $m = 1$ mode in toroidal geometry for safety factor profiles with an inflection point, *Phys. Fluids B*, *1*, 788.

Horiuchi, R., and T. Sato (1997), Particle simulation study of collisionless driven reconnection in a sheared magnetic field, *Phys. Plasmas*, *4*(2), 277–289.

Hoshino, M., and A. Nishida (1983), Numerical simulation of the dayside magnetopause, *J. Geophys. Res.*, *88*, 6926.

Huba, J. D. (2005), Hall magnetic reconnection: Guide field dependence, *Phys. Plasmas*, *12*, 012322.

Igochine, V., O. Dumbrajs, H. Zohm, A. Flaws, and A. U. Team (2007), Stochastic sawtooth reconnection in ASDEX upgrade, *Nucl. Fusion*, *47*, 23.

Jardin, S. C. (2004), A triangular finite element with first-derivative continuity applied to fusion MHD applications, *Journal of Computational Physics*, *200*, 133–152.

Jardin, S. C. (2012), Review of implicit methods for the magnetohydrodynamic description of magnetically confined plasmas, *Journal of Computational Physics*, *231*, 822–838.

Jemella, B. D., M. A. Shay, J. F. Drake, and B. N. Rogers (2003), Impact of frustrated singularities on magnetic island evolution, *Phys. Rev. Lett.*, *91*(12), 125002.

Jemella, B. D., J. F. Drake, and M. A. Shay (2004), Singular structure of magnetic islands resulting from reconnection, *Phys. Plasmas*, *11*(12), 5668–5672.

Kadomtsev, B. B. (1975), Disruptive instability in tokamaks, *Fiz. Plazmy*, *1*, 710.

Kleva, R., J. Drake, and F. Waelbroeck (1995), Fast reconnection in high temperature plasma, *Phys. Plasma*, *2*, 23.

Kleva, R. G. (1992), Stabilization of sawteeth in tokamaks by sheared poloidal flows, *Phys. Fluids B*, *4*, 218.

Kleva, R. G., and P. N. Guzdar (2002), Stabilization of sawteeth in tokamaks with toroidal flows, *Phys. Plasmas*, *9*, 3013.

Kobayashi, S., B. N. Rogers, and R. Numata (2014), Gyrokinetic simulations of collisionless reconnection in turbulent non-uniform plasmas, *Phys of Plasmas*, *21*, 040704.

La Haye, R., L. Lao, E. Strait, and T. Taylor (1997), High beta tokamak operation in DIII-D limited at low density/collisionality by resistive tearing modes, *Nuclear Fusion*, *37*(3), 397.

Lawson, J. D. (1957), Some criteria for a power producing thermonuclear reactor, *Proceedings of the Physical Society. Section B*, *70*(1), 6.

Lazarus, E. A., F. L. Waelbroeck, T. C. Luce, M. E. Austin, K. H. Burrell, J. R. Ferron, A. W. Hyatt, T. H. Osborne, M. S. Chu, D. P. Brennan, P. Gohil, R. J. Groebner, C. L. Hsieh, R. J. Jayakumar, L. L. Lao, J. Lohr, M. A. Makowski, C. C. Petty, P. A. Politzer, R. Prater, T. L. Rhodes, J. T. Scoville, E. J. Strait, A. D. Turnbull, M. R. Wade, G. Wang, H. Reimerdes, and C. Zhang (2006), A comparison of sawtooth oscillations in bean and oval shaped plasmas, *Plasma Phys. Control. Fusion*, *48*, L65–L72.

Levinton, F. M., R. J. Fonck, G. M. Gammel, R. Kaita, H. W. Kugel, E. T. Powell, and D. W. Roberts (1989), Magnetic field pitch-angle measurments in the PBX-M tokamak using the motional Stark effect, *Phys. Rev. Lett.*, *63*, 2060.

Levinton, F. M., L. Zakharov, S. H. Batha, J. Manickam, and M. C. Zarnstorff (1994), Stabilization and onset of sawteeth in TFTR, *Phys. Rev. Lett.*, *72*, 2895.

Lichtenberg, A. J., K. Itoh, S. I. Itoh, and A. Fukuyama (1992), The role of stochasticity in sawtooth oscillations, *Nucl. Fusion*, *32*, 495.

Loureiro, N. F., S. C. Cowley, W. D. Dorland, M. G. Haines, and A. A. Schekochihin (2005), X-point collapse and saturation in the nonlinear tearing mode reconnection, *Phys. Rev. Lett.*, *95*, 235003.

Mandt, M. E., R. E. Denton, and J. F. Drake (1994), Transition to whistler mediated magnetic reconnection, *Geophys. Res. Lett.*, *21*, 73.

McGuire, K., and D. C. Robinson (1979), Sawtooth oscillations in a small tokamak, *Nucl. Fusion*, *19*, 505.

Mozer, F., S. D. Bale, and T. D. Phan (2002), Evidence of diffusion regions in a subsolar magnetopause crossing, *Phys. Rev. Lett.*, *89*, 015002.

Murphy, N. A., C. R. Sovinec, and P. A. Cassak (2010), Magnetic reconnection with asymmetry in the outflow direction, *J. Geophys. Res.*, *115*, A09206.

Muscatello, C. M., W. W. Heidbrink, Y. I. Kolesnichenko, V. V. Lutsenko, M. A. V. Zeeland, and Y. V. Yakovenko (2012), Velocity-space studies of fast-ion transport at a sawtooth crash in neutral-beam heated plasmas, *Plasma Phys. Control. Fusion*, *54*, 025006.

Nave, M., J. Rapp, T. Bolzonella, R. Dux, M. Mantsinen, R. Budny, P. Dumortier, M. von Hellermann, S. Jachmich, H. Koslowski, G. Maddison, A. Messiaen, P. Monier-Garbet, J. Ongena, M. Puiatti, J. Strachan, G. Telesca, B. Unterberg, M. Valisa, P. de Vries, and

contributors to the JET-EFDA Workprogramme (2003), Role of sawtooth in avoiding impurity accumulation and maintaining good confinement in jet radiative mantle discharges, *Nuclear Fusion*, *43*(10), 1204.

Osborne, T. H., R. N. Decker, and S. C. Prager (1982), Discharges with safety factor, q, < 1 in a noncircular tokamak, *Phys. Rev. Lett.*, *49*, 734.

Papadopoulos, K. (1977), A review of anomalous resistivity for the ionosphere, *Rev. Geophys. Space Phys.*, *15*, 113.

Park, W., D. A. Monticello, and T. K. Chu (1987), Sawtooth stabilization through island pressure enhancement, *Phys. Fluids*, *30*, 285.

Park, W., E. V. Belova, G. Y. Fu, X. Z. Tang, H. R. Strauss, and L. E. Sugiyama (1999), Plasma simulation studies using multilevel physics models, *Phys. Plasmas*, *6*, 1796.

Parker, E. N. (1957), Sweet's mechanism for merging magnetic fields in conducting fluids, *J. Geophys. Res.*, *62*, 509.

Pegoraro, F., F. Porcelli, and T. J. Schep (1989), Internal kink modes in the ion-kinetic regime, *Phys. Fluids B*, *1*, 364.

Petschek, H. E. (1964), Magnetic field annihilation, in *AAS/NASA Symposium on the Physics of Solar Flares*, edited by W. N. Ness, p. 425, NASA, Washington, DC.

Phan, T. D., J. T. Gosling, G. Paschmann, C. Pasma, J. F. Drake, M. Øieroset, D. Larson, R. P. Lin, and M. S. Davis (2010), The dependence of magnetic reconnection on plasma beta and magnetic shear: Evidence from solar wind observations, *Ap. J. Lett.*, *719*, L199.

Porcelli, F. (1991), Fast particle stabilization, *Plasma Phys. Control. Fusion*, *33*, 1601.

Porcelli, F., D. Boucher, and M. N. Rosenbluth (1996), Model for the sawtooth period and amplitude, *Plasma Phys. Control. Fusion*, *38*, 2163.

Prater, R. (2004), Heating and current drive by electron cyclotron waves, *Phys of Plasmas*, *11*(5), 2349–2376.

Pritchett, P. L. (2001), Geospace environmental modeling magnetic reconnection challenge: simulations with a full particle electromagnetic code, *J. Geophys. Res.*, *106*, 3783.

Pritchett, P. L. (2008), Collisionless magnetic reconnection in an asymmetric current sheet, *J. Geophys. Res.*, *113*, A06210.

Pritchett, P. L., and F. V. Coroniti (2004), Three-dimensional collisionless magnetic reconnection in the presence of a guide field, *J. Geophys. Res.*, *109*, 1220.

Rice, B. W. (1992), Fifteen chord FIR polarimetry system on MTX, *Rev. Sci. Instrum.*, *63*, 5002.

Rijnbeek, R. P., V. S. Semenov, A. A. Shmalts, H. K. Biernat, M. F. Heyn, and B. P. Besser (1991), Time-dependent reconnection in a current sheet with velocity shear, *Planet. Space Sci.*, *39*, 1377.

Rogers, B., and L. Zakharov (1995), Nonlinear ω_* stabilization of the $m = 1$ mode in tokamaks, *Phys. of Plasmas*, *2*, 3420.

Rogers, B. N., and R. E. Denton (2003), Signatures of collisionless magnetic reconnection, *J. Geophys. Res.*, *108*(A3), 1111.

Rogers, B. N., R. E. Denton, J. F. Drake, and M. A. Shay (2001), Role of dispersive waves in collisionless magnetic reconnection, *Phys. Rev. Lett.*, *87*(19), 195004.

Sarff, J., A. Almagri, J. Anderson, D. Brower, D. Craig, B. Deng, D. D. Hartog, W. Ding, G. Fiksel, C. Forest, V. Mirnov, S. Prager, and V. Svidsinski (2005), Magnetic reconnection and self-organization in reversed field pinch laboratory plasmas, in *The Magnetized Plasma in Galaxy Evolution*, edited by K. Chyzy, K. Otmianowska-Mazur, M. Soida, and R.-J. Dettmar, pp. 48–55.

Sauter, O., E. Westerhof, M. L. Mayoral, B. Alper, P. A. Belo, R. J. Buttery, A. Gondhalekar, T. Hellsten, T. C. Hender, D. F. Howell, T. Johnson, P. Lamalle, M. J. Mantsinen, F. Milani, M. F. F. Nave, F. Nguyen, A. L. Pecquet, S. D. Pinches, S. Podda, and J. Rapp (2002), Control of neoclassical tearing modes by sawtooth control, *Phys. Rev. Lett.*, *88*, 105001.

Scholer, M. (1989a), Undriven magnetic reconnection in an isolated current sheet, *J. Geophys. Res.*, *94*(A7), 8805–8812.

Scholer, M. (1989b), Asymmetric time-dependent and stationary magnetic reconnection at the dayside magnetopause, *J. Geophys. Res.*, *94*, 15099.

Scott, B. D., and A. B. Hassam (1987), Analytical theory of nonlinear drift-tearing mode stability, *Physics of Fluids*, *30*(1), 90–101.

Shafranov, V. D. (1966), Plasma equilibrium in a magnetic field, *Reviews of Plasma Physics*, *2*, 103.

Shay, M. A., J. F. Drake, R. E. Denton, and D. Biskamp (1998), Structure of the dissipation region during collisionless magnetic reconnection, *J. Geophys. Res.*, *25*, 9165.

Shay, M. A., J. F. Drake, B. N. Rogers, and R. E. Denton (1999), The scaling of collisionless, magnetic reconnection for large systems, *Geophys. Res. Lett.*, *26*, 2163.

Shay, M. A., J. F. Drake, M. Swisdak, and B. N. Rogers (2004), The scaling of embedded collisionless reconnection, *Phys. Plasmas*, *11*(5), 2199.

Soltwisch, H. (1988), Measurement of current density changes during sawtooth activity in a tokamak by far-infrared polarimetry, *Rev. Sci. Instrum.*, *59*, 1599.

Soltwisch, H. (1992), Current density measurements in tokamak devices, *Plasma Phys. Control. Fusion*, *34*, 1669.

Spitzer, L., and R. Härm (1953), Transport phenomena in a completely ionized gas, *Phys. Rev.*, *89*, 977.

Sweet, P. A. (1958), The neutral point theory of solar flares, in *Electromagnetic Phenomena in Cosmical Physics*, edited by B. Lehnert, p. 123, Cambridge University Press, New York.

Swisdak, M., J. F. Drake, M. A. Shay, and B. N. Rogers (2003), Diamagnetic suppression of component magnetic reconnection at the magnetopause, *J. Geophys. Res.*, *108*(A5), 1218.

Swisdak, M., M. Opher, J. F. Drake, and F. A. Bibi (2010), The vector direction of the interstellar magnetic field outside the helioshere, *Ap. J.*, *710*, 1769.

Sykes, A., and J. A. Wesson (1976), Relaxation instability in tokamaks, *Phys. Rev. Lett.*, *37*, 140.

Tanaka, M. (1996), Asymmetry and thermal effects due to parallel motion of electrons in collisionless magnetic reconnection, *Phys. Plasmas*, *3*, 4010.

Terasawa, T. (1983), Hall current effect on tearing mode instability, *Geophys. Res. Lett.*, *10*, 475.

Tournianski, M. R., R. J. Akers, P. G. Carolan, and D. L. Keeling (2005), Anisotropic fast nerutral particle spectra in the MAST spherical tokamak, *Plasma Phys. Control. Fusion*, *47*(5), 671.

Ugai, M. (2000), Computer simulations of asymmetric spontaneous fast reconnection, *Phys. Plasma*, *7*, 867.

Uzdensky, D. A., and R. M. Kulsrud (2000), Two-dimensional numerical simulation of the resistive reconnection layer, *Phys. Plasmas*, *7*(10), 4018.

Vasyliunas, V. M. (1975), Theoretical models of magnetic field line merging, 1, *Rev. Geophys.*, *13*(1), 303.

von Goeler, S., W. Stodiek, and N. R. Sautoff (1974), Studies of internal disruptions and $m = 1$ oscillations in tokamak discharges with soft-X-ray tecniques, *Phys. Rev. Lett.*, *33*, 1201.

Wang, X., and A. Bhattacharjee (1995), Nonlinear dynamics of the $m = 1$ kink-tearing instability in a modified magnetohydrodynamic model, *Phys. Plasmas*, *2*, 171.

Webster, A. J. (2003), Fusion: Power for the future, *Physics Education*, *38*(2), 135.

Wesson, J. (1987), *Tokamaks*, Clarendon Press, Oxford.

Wesson, J. A., A. W. Edwards, and R. S. Granetz (1991), Spontaneous $m = 1$ instability in the JET sawtooth collapse, *Nucl. Fusion*, *31*, 111.

Wesson, J. A., B. Alper, A. W. Edwards, and R. D. Gill (1997), Transport in the sawtooth collapse, *Phys. Rev. Lett.*, *79*, 5018.

West, W. P., D. M. Thomas, J. S. deGrassie, and S. B. Zhang (1987), Measurement of the rotational transform at the axis of a tokamak, *Phys. Rev. Lett.*, *58*, 2758.

White, R. B., M. N. Bussac, and F. Romanelli (1989), High-β, sawtooth-free tokamak operation using energetic trapped particles, *Phys. Rev. Lett.*, *62*, 539.

White, R. B., F. Romanelli, and M. N. Bussac (1990), Influence of an energetic ion population on tokamak plasma stability, *Phys. Fluids B*, *2*, 745.

Wroblewski, D., and L. L. Lao (1991), Determination of the safety factor in sawtoothing discharges in DIII-D, *Phys. Fluids B*, *3*, 2877.

Yamada, M., F. M. Levinton, N. Pomphrey, R. Budny, J. Manickam, and Y. Nagayama (1994), Investigation of magnetic reconnection during a sawtooth crash in a high-temperature tokamak plasma, *Phys. Plasmas*, *1*, 3269–3276.

Yamada, M., Y. Ren, H. Ji, J. Breslau, S. Gerhardt, R. Kulsrud, and A. Kuritsyn (2006), Experimental study of two-fluid effects on magnetic reconnection in a laboratory plasma with variable collisionality, *Phys. Plasmas*, *13*, 052119.

Yamaguchi, S., H. Igami, H. Tanaka, and T. Maekawa (2004), Observations of sawtooth crashes by a multi-toroidally positioned soft x-ray computer tomography system in the WT-3 tokamak, *Plasma Phys. and Conrol. Fusion*, *46*, 1163–1180.

Zakharov, L., and B. Rogers (1992), Two-fluid magnetohydrodynamic description of the internal kink mode in tokamaks, *Phys. Fluids B*, *4*, 3285.

Zakharov, L., B. Rogers, and S. Migliuolo (1993), The theory of the early nonlinear stage of $m = 1$ reconnection in tokamaks, *Phys. Fluids B*, *5*, 2498.

Zakharov, L. E., F. M. Levinton, S. H. Batha, R. V. Budny, M. C. Zarnstorff, S. Migliuolo, and B. Rogers (1994), Onset and stabilization of sawtooth oscillations in tokamaks, in *Plasma Physics and Controlled Nuclear Fusion Research*, vol. Proceedings of the 15th International Conference, Seville, pp. 407–415, IAEA.

Zaslavskiĭ, G. M., and B. V. Chirikov (1972), Reviews of topical problems: Stochastic instability of non-linear oscillations, *Sov. Phys. Usp.*, *14*, 549.

Zeiler, A., D. Biskamp, J. F. Drake, B. N. Rogers, M. A. Shay, and M. Scholer (2002), Three-dimensional particle simulations of collisionless magnetic reconnection, *J. Geophys. Res.*, *107*, 1230.